Title	Development of Rigid Body Coupled Spring discrete model for simulation of cementitious composites and structural elements
Author(s)	Saeid Mehrpay Moghaddam
Citation	北海道大学. 博士(工学) 甲第13999号
Issue Date	2020-03-25
DOI	10.14943/doctoral.k13999
Doc URL	http://hdl.handle.net/2115/78359
Type	theses (doctoral)
File Information	Saeid_Mehrpay_Moghaddam.pdf

Development of Rigid Body Coupled Spring discrete model for simulation of cementitious composites and structural elements

セメント系複合材料および構造要素のシミュレーションのための
剛体-バネ連成離散モデルの開発

By
Saeid Mehrpay M.

A thesis submitted in partial fulfilment of the requirements for the degree of
Doctor of Philosophy

Supervisors
A. Professor Koji Matsumoto
Professor Tamon Ueda

Department of Civil Engineering
Division of Engineering and Policy for Sustainable Environment (EPSE)
Laboratory of Engineering for Maintenance System
Graduate School of Engineering - e3 Program
Hokkaido University
Sapporo, Japan
January 2020

Acknowledgements

I would like to take this chance to give my sincere gratitude to professor Tamon Ueda for providing support and guidance during my research period. It was a great honour for me to have this chance to study under his supervision.

I would like to extend my gratitude to our associate professor Dr. Koji Matsumoto for his vital comments and discussions.

My gratitude also extends to the examination committee, professor Takeshi Matsumoto and professor Motohiro Sato, thanks to whose kind comments the contents of this thesis was improved.

I would like to thank my colleague, Zhao Wang for his collaborations. His inputs on the research were nourishing and made major improvements.

I would like to give my sincere thanks to our assistant professor Dr. Hitoshi Furuuchi at the lab of engineering for maintenance system and to my lab-mates and colleagues, Zhu Miaochang, Linh Van Hong Bui, Rajkamal Kumar, Irish Sultan Tambis, Shono Marin, Mahmudul Hasan Mizan, Haruna Minakawa, Liangliang Wei and the secretary of the laboratory Ms. Naoko Masaki for their helps and support and all the good memories. I wish you all the best.

Finally, I would like to express appreciation to my family and friends for their emotional and financial support from the other side of the world which encouraged me to step forward with a strong heart.

Table of Contents

Abstract

A new element based on the concept of Rigid Body Spring Model (RBSM) that inherently incorporates Poisson effect is developed and utilized to simulate nonlinear behaviour of concrete.

Nonlinear material models are implemented based on the meso-scale modelling technique and do not have the complexity of macroscopic models based on volumetric and deviatoric stress and strain tensors separation. Beside the capability of representing the Poisson's ratio of the material, with the new material models implemented, the new element can represent the compressive, tensile and shear behaviour of concrete as well as provide the principal stresses in the model.

With further development of the element the capability of simulating fibrous concrete was added to the developed discrete model.

The uniaxial compressive and tensile test beside splitting tensile test on plain concrete specimen were simulated successfully and similar cracking patterns to the experiments were observed in the simulations.

Investigation on the SFRC models performed as uniaxial compression, direct tension, flexural beams tests and direct shear through push-off were conducted to verify the capability of the model.

The new discrete element was also employed into simulation of a prefabricated concrete wall keyed shear connection to show the capabilities of the model beyond material scale.

It was observed that the model could predict the strength of the connection and its failure modes properly for two shear key size.

The new ability to visualize stresses and displacement distribution in the model helped clarifying the behaviour of the model.

Development of Rigid Body Coupled Spring discrete model for simulation of cementitious composites and structural elements

By
Saeid Mehrpay M.

A thesis submitted in partial fulfilment of the requirements for the degree of
Doctor of Philosophy

Examination Committee
Associate Professor Koji Matsumoto (Supervisor)
Professor Tamon Ueda (Supervisor)
Professor Takashi Matsumoto
Professor Motohiro Sato

Department of Civil Engineering
Division of Engineering and Policy for Sustainable Environment (EPSE)

Laboratory of Engineering for Maintenance System
Graduate School of Engineering - e3 Program
Hokkaido University
Sapporo, Japan
January 2020

Chapter 1

Introduction

1.1. Background

Concrete is a fundamental material and the backbone of almost all modern engineering structures. The economically optimized designing of structures capable of withstanding harsh conditions requires a good understanding of the behaviour of concrete under different circumstances. This requirement has opened up vast areas in the field of concrete research and the scope of these studies is still widening. When it comes to numerical analysis of solid mechanics problem, it is generally accepted that Finite Element Analysis (FEA) is the most widely developed method that can be employed; however, when it comes to the simulation of continuums comprised of granular particle with a quasi-brittle behaviour like concrete, FEA has some shortcomings for simulation of the behaviour of the cracked material. Many constitutive models have been developed for concrete like materials and employed in FEA, but the complicated nonlinear behaviour of concrete has made it difficult to provide a general constitutive model of concrete for all engineering purposes. Accordingly, different approaches and modelling techniques are used under different conditions in response to the specific requirements and challenges faced of the design in question. As an alternative to FEA, techniques based on discrete elements has been widely employed in the field of solid mechanics for simulation of granular materials or materials subject to cracking and discontinuities. This approach has also aided researchers to create less complicated models for concrete like materials that can better represent their real-world prototypes for specific cases (e.g. [1–3]). Advances achieved in this field can improve the ability to simulate and predict the behaviour of engineering structures and estimate their durability in harsh environments and contribute to attaining a better understanding of the complicated behaviour of materials. Kawai tried to address the issues of FEA by developing a discrete model base on the idea of using rigid blocks to represent such volumes made of connected particles forming a solid [4]. Kawai represented the new method in a trinary of elements that could be used to simulate solids, beams and plates. This modelling technique is known as Rigid Body Spring Model (RBSM) and has found its way into geotechnical studies and solid mechanics.

In 1997, Meguro and Tagel-Din used a new DEM method, which was later referred to as Applied Element Method (AEM), to investigate crack initiation and propagation in reinforced concrete walls under monotonic and cyclic loadings. They used discrete blocks connected with normal and shear springs at the distributed contact points around the perimeter of the blocks. The crack initiation was detected by calculating the principal tensile stress at the location of contact points and comparing it with the maximum allowed value; this approach would reduce the dependency of crack propagation path to the blocks shape and size. This method also has the advantage of modelling behaviour of the structures to the point of complete loss of resistance (global failure) [1]. In 1998, Meguro and Tagel-Din improved this method to solve the problems dealing with large deformation and rigid body motion [5]. They also introduce a method to represent Poisson effect which was later introduced into AEM [6].

K. Sonoda and A. Kambayashi in 1992 [7] and A. Kambayashi et al. in 1999 [8], developed RBSM to make it applicable to impact and wave propagation in elastic bodies problems.

In 2004, K. Nagai et al. [2] used RBSM to develop a two-dimensional mesoscopic concrete model and investigated its failure behaviour under specific situations. In 2005, they expanded their investigations to produce a 3-dimensional RBSM and further investigated the behaviour of their mesoscopic model [9]. In these studies, formulations for recalibration of Poisson’s ratio and Elastic modulus was proposed to obtain lateral deformations for concrete which would resemble Poisson effect by increasing shear deformations in meso-scale. Further on In 2009, this technique was extended by T. Ueda et al. to create mesoscopic models for investigating effect of frost damage on concrete [10]. Their model could predict the effect of different levels of frost damage on properties of concrete. In 2011 and 2014 Y. Yamamoto et al. also investigated compressive and cyclic fracture of concrete by further development to the same RBSM technique [11,12].

In this paper a new discrete element, based on RBSM method, is introduced that incorporates Poisson effect which in is usually ignored or calculated indirectly in most discrete models. In the first part of this paper, application of new element in elastic linear analysis is discussed and after that the new element is utilized for nonlinear simulation of cement concrete. In this manuscript the new element is referred to as Rigid Body and Coupled Springs (RBCS) element, is introduced and described in details and investigated in more simulation cases. Theory and application of this element is also available in [13–15]. The analysis software is developed using Intel Fortran[16] compiler installed on integrated development environment of Visual Studio. The Intel Fortran compiler comes with Math Kernel Library[17] which is also employed for efficient matrixial calculations and utilising full capacity of multi-core CPU machines using multi-threading which will dramatically reduce the calculation time.

The employed concept for material model is similar to the one utilized by Nagai et al. in 2004 [18] where nonlinear behaviour is considered for springs separately; however some dramatical changes were implemented to adapt with new element and improve its behaviour.

1.2. Motivation of the research

As already mentioned in the introduction, implementation of the discrete models into simulation of concrete-like materials, which are subject to cracking and discontinuities, comes with advantages such as simpler constitutive models, reduced calculation expenses and ability to capture discontinuities. While alternative methods such as the Finite Element Method (FEM) is not capable of simulating discontinuities and crack closure unless special methods, such as the one developed in [19,20], are employed. The Extended Finite Element Method (XFEM) approach, which was developed to overcome the limitation of FEM in simulation of fracture, can consider crack propagation and discontinuities in the model, however this method has limitation such as the location of the initiation of the crack and its direction has to be defined by the user (i.e. such location has to be known in the simulated problem) and yet there are additional limitations on the number crack initiation points [21].

On the other hand, many researches have used RBSM method to study the fracture process of concrete in various circumstances. Yet the RBSM also has limitation such as the inaccuracy of evaluating the deformations due to Poisson effect which can be very important in capturing the confinement stresses in the concrete. Also, some RBSM methods can lead to calculation of inaccurate stresses [22] while modification of mechanical properties of internal springs to incorporate Poisson effect as proposed by Nagai et al. [18] can lead to more inaccuracies of calculating internal stresses.

Another limitation of the RBSM method is inability to evaluate principal stresses in the model as well as inability to evaluate stresses in a globally specified direction (e.g. global X or Y axis). This issue which can be a significant shortcoming in comparison to FEM, will be discussed and demonstrated in the coming sections.

The main objective of this research is to develop a new discrete model that resolve mentioned issues with the RBSM technique and provide a more advanced tool for the simulation of the nonlinear behaviour of the concrete.

Secondary goals of the research are improving the constitutive models and the outcome of the numerical simulations and extending the method into simulation of fibrous concrete materials that are drawing more attention in recently. This topic will be opened further in the corresponding chapter.

Finally, to demonstrate the capability of the new element beyond material level, a case of simulating in structural level will be chosen. In this final investigation, the fractural pattern of a structural element will be simulated with the new element.

1.3. Overview of the original solid RBSM

As already mentioned, discrete techniques are suitable for simulation of granular materials. The RBSM uses a discrete concept in which three types of elements comprise a rigid part and contact springs. The trinary elements of RBSM include *beam bending element*, *axial strain element* and *plate bending element*. The focus of this paper is on the axial strain element, which is also referred to as the *plane strain element* or *solid element.*

In RBSM rigid blocks are obtained by discretizing the model. No specific shape is mandatory for these blocks therefore a Voronoi diagram or another tessellation method can be used. For the case of 2-dimensional axial strain element, tessellated blocks have one rotational and two displacement degree of freedom at the centroid and it is assumed that they are connected on any mutual ridge using zero-length normal, shear and rotational springs.

The stiffness of normal springs for axial strain element is derived assuming zero strains for both in plane and out of plane orthogonal directions. In other words, a condition of axial strain is assumed[1] which will lead to a simplified hook law in which Poisson effect is ignored. The stiffness of axial, shear and rotational contact springs derived using this simplifying assumption is given in Equation 1 to 3.

$$K_n = \frac{E(1-\nu)L_r}{(1+\nu)(1-2\nu)(h_1+h_2)}$$ *Equation 1*

$$K_s = \frac{EL_r}{(1+\nu)(h_1+h_2)}$$ *Equation 2*

$$K_r = \frac{K_n L_r^2}{12}$$ *Equation 3*

In which K_n, K_s, K_r are the stiffness of the normal springs, shear springs and rotational springs respectively, E is the elastic modulus of the material, ν is the Poisson's ratio, L_r is the ridge's length, h_1 and h_2 are the normal distance from the rigid block centroid to the ridge of the first and the second element.

While from Equation 1 it is evident that the normal stiffness is derived by taking advantage of the stress-strain relationship in special case of axial strain[1], the shear stiffness is simply using the "shear stress – shear strain" relationship with this exception that the spring deformation represent only half of the shear deformation ($\varepsilon_s = \frac{\gamma}{2}$) and therefore instead of shear modulus of G, $\breve{G} = 2G$ is used (Figure 1).

$$G = \frac{E}{2(1+\nu)} \qquad \text{Equation 4}$$

$$\breve{G} = \frac{E}{1+\nu} \qquad \text{Equation 5}$$

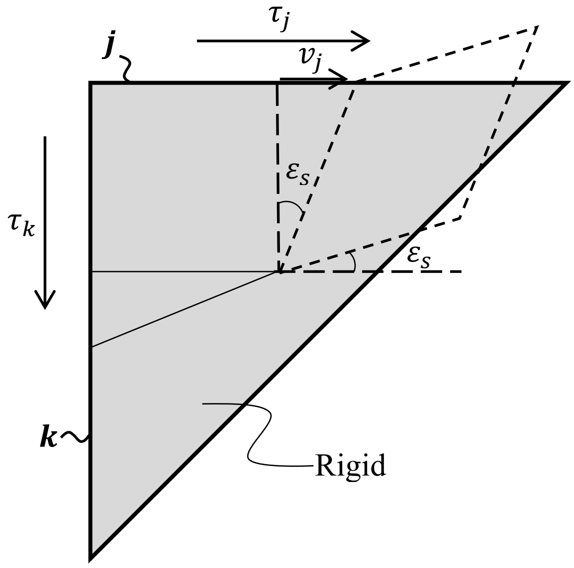

Figure 1. shear strain and deformation in shear spring

Finally, a rotational stiffness is added for rotational degree of freedom of rigid body. If the free body diagram of rigid body is considered, the rotational resistance of this part will be due to resisting shear at the circumference and the variation of normal stresses at the edges of rigid body. Since single normal springs at each face go through the centroid of the rigid body and cannot account for stress variation, they do not contribute to the rotational stiffness and the rotational resistance would be underestimated. The rotational stiffness will resolve this issue as an additional aid to shear springs. The stiffness of the rotational spring is calculated by calculating the resisting moment due to stress variation along the edge, assuming a linear relationship between stress and strain.

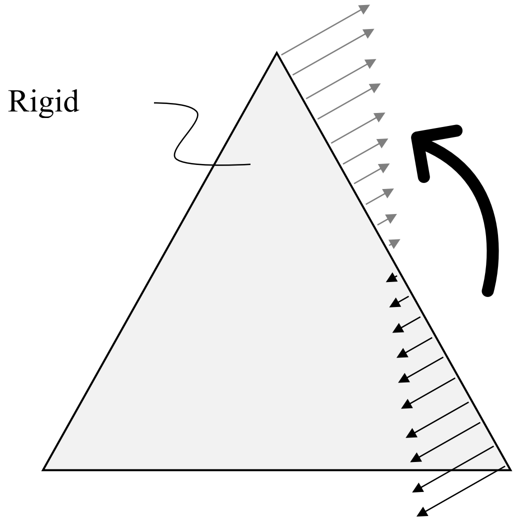

Figure 2. Stress variation can create additional resisting moment

1.4. Modified Plane Stress RBSM Element

As discussed above the RBSM element is meant for fully confined cases in which, to derive the stiffness of normal springs, strain is assumed to be zero in two orthogonal directions. Nagai et al. used a modified version of this assumption for simulation of concrete specimens [18]. The modified concept uses stress-strain relationship that can be obtained by combining plane strain and plane stress[2] to derive the stiffness of normal springs (Equation 6).

$$K_n = \frac{EL_r}{(1-\nu^2)} \qquad \text{Equation 6}$$

Another alteration to original RBSM is modification of mesoscopic properties to make up for the Poisson effect. As stated, the RBSM is actually a Discrete element in which the contact between rigid blocks are provided by use of springs. One-dimensional normal springs are not capable of providing lateral expansion, when deformation is induced in an orthogonal direction. This issue can be more easily observed in a simplified case of square rigid blocks discretization where vertical deformation will not induce any force and deformation to horizontal springs (Figure 3). Therefore, the Poisson effect is not originally incorporated in RBSM method. Using axial strain condition makes the RBSM element suitable for special applications (i.e. simulation of infinite or semi-infinite volumes), however, Poisson effect cannot be simply ignored in many problems especially in case of hydrostatic pressure sensitive materials, like cement concrete for simulation of which RBSM has been utilized by many researchers. In addition, if the problem does not satisfy the condition based on which the stress-strain relationship is derived (e.g. axial strain) beside lack of the Poisson effect, the accuracy of the modelling will also be affected.

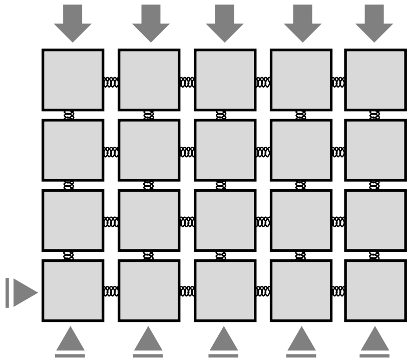

Figure 3. Inability of RBSM to capture Poisson deformation

That being the case, Nagai et al. [2] proposed using different meso-scale mechanical properties to recreate a macro-scale behaviour corresponding to material's Poisson's ratio and stiffness (Throughout this paper, we refer to this method as calibrating RBSM since a calibration for mesoscopic Poisson's ratio and Elastic modulus is required). In this method a different value of Poisson's ratio is considered as the mesoscopic Poisson's ratio for the springs which is several times bigger than original (macro-scale) Poisson's ratio of the material (mesoscopic Poisson's ratio can be assumed larger than 0.5). Larger Poisson's ratio will cause the stiffness of shear spring be reduced (Equation 5) which will lead to increased shear deformation and therefore increased deformation in surfaces inclined to the direction of load causing increment to the lateral deformations which will resemble the Poisson effect phenomenon. Increasing Poisson's ratio will cause the stiffness of normal springs be increased (Equation 6), this issue was also addressed by assuming a reduced mesoscopic elastic modulus. Nagai et al. proposed equations for calculating the mesoscopic Poisson's ratio and elastic modulus as a function of the original Poisson's ratio and elastic modulus of the material. However, there are a few considerations about this approach, for instance this approach Poisson effect relies on shear deformations and therefore the lateral deformation will be affected by the shape of the elements. On the other hand, since the stiffness of shear springs was modified, it may affect the shear stresses in the model.

A different approach proposed by Fang et al. is using force redistribution to incorporate Poisson effect in RBSM [22]. In this method, after obtaining initial deformations, a residual force will be calculated to recreate the Poisson effect, which will lead to secondary deformations and secondary residual forces should be calculated to represent secondary Poisson effects and this loop will continue until the desired accuracy for Poisson deformations are attained. A similar method was also employed by Asahina et al. to simulate Poisson effect in elastic lattice models [23].

In the next section the new element (RBCS) is introduced that can represent Poisson effect by relating the behaviour of springs on each rigid body.

1.5. Review of Nagai et al. material models for 2D RBSM

The model used by Nagai et al. employs RBSM elements that are derived from combined Planes stress and Plane strain[2] condition [18]. The normal and shear springs connect rigid bodies and the rotational spring is omitted but a small constant rotational stiffness is added to stiffness matrix to prevent instability of the model.

The elastic modulus and Poisson's ratio used to derive the stiffness of the springs is different from the real material. The reason of this difference is to obtain lateral deformations that are close to the lateral deformation of original material due to the Poisson effect in uniaxial compression test. For this purpose, empirical functions provided to evaluate the elastic modulus and Poisson's ratio for springs.

1.5.1. Nonlinear behaviour of normal springs

Normal springs behave elastically in compression but will undergo softening and failure in tension (Figure 5). Therefore, the most important property that defines the failure point of normal springs is the maximum tensile stress of normal springs, σ_t^c which is assumed to be equal to the tensile strength of concrete, f_t.

Beside the tensile behaviour, maximum tensile strength also determines the behaviour of shear springs (as it is pointed out in the next section) and therefore determines the compressive behaviour of model. In other words, the most important parameter for the model is the tensile strength. To make a meaningful connection between the given tensile strength (f_t) and the expected compressive strength (f_c'), Nagai et al. implemented the relationship proposed by Kosaka et al. as cited in [18] (Equation 7). It is worth mentioning that authors in this paper have used the relationships suggested by fib model codes [24,25] for conversion of tensile strength of concrete. A comparison of Kosaka et al. model and some other commonly used relationships is depicted in Figure 4 to clear out the difference.

$$f_t = 1.4 \times Ln(f_c') - 1.5 \qquad \textit{Equation 7}$$

The behaviour of normal springs is depicted in Figure 5 in which the dashed line shows the unloading path during tensile softening. The tensile strength of springs will become zero (total tensile failure) when an assumed maximum crack width is reached.

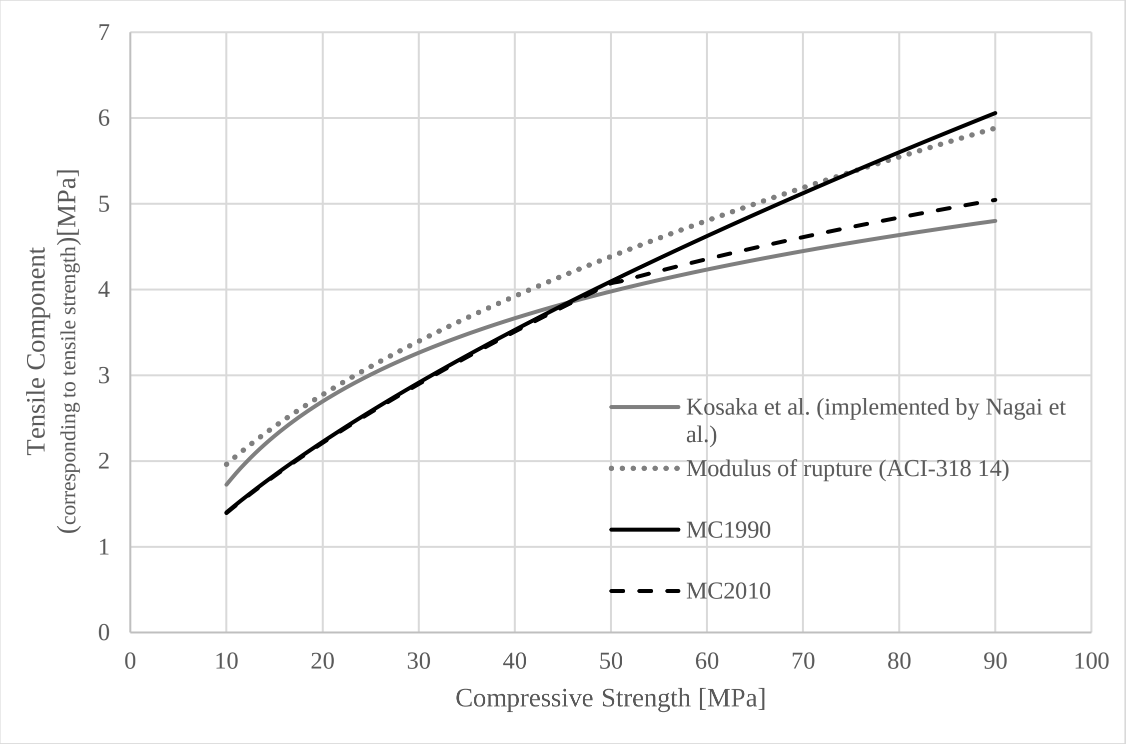

Figure 4. Comparison of relationships between compressive and tensile component (modulus of rupture or tensile strength)

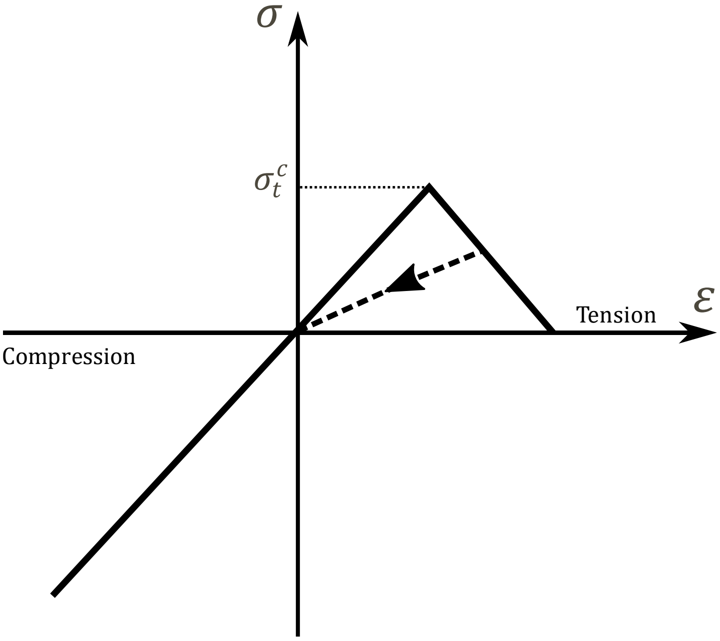

Figure 5. Material model for normal spring of Nagai et al.

To account for the non-homogenous nature of mortar, Nagai et al. used a probabilistic function to distribute different maximum tensile stress among normal springs. Using such function is also improve the curvature of ascending branch of stress-strain response of model in uniaxial compressive loading.

1.5.2. Nonlinear behaviour of shear springs

Shear springs have elastic - prefect plastic behaviour in which the yielding stress is a function of normal stress (Figure 6). The shear resistance capacity will be reduced as the common area of two adjacent element is reduced when they slide due to shear deformation. This is also another factor which will induce mesh size dependency since it will make the smaller elements to fail more rapidly under same shear deformation since the common area is smaller.

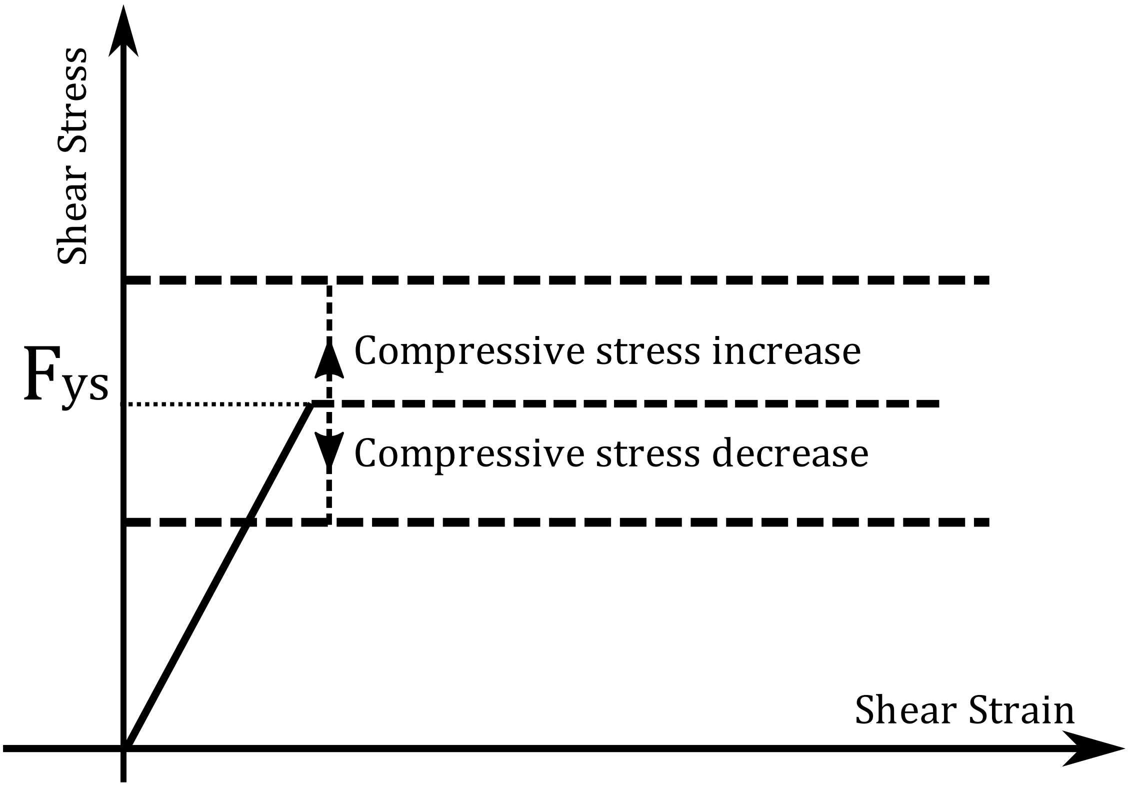

Figure 6. Shear spring model of Nagai et al.

1.5.3. Interfacial elements

In Meso-scale modelling technique of simulating behaviour of concrete like materials it is very common to assume that the model comprises mortar and aggregate phases. Nagai et al. beside homogenous models also employed non-homogenous models consisting of mortar phase and aggregate phase into simulation of concrete like materials. The aggregates are assumed to have elastic behaviour and for the springs in the aggregate-mortar interface, a mean value for stiffness is evaluated from mortar and aggregate elements.

To assess the new element in simulation of nonlinear behaviour of concrete, similar concepts as what briefly introduced in this section are implemented with some modifications to obtain an improved behaviour. In the next section the implemented material models into RBCS element are described in detail.

Chapter 2

Developing Rigid Body Coupled Springs Element

The RBCS element is based on a triangular rigid body and springs that have a dependent stress-strain relationship. The triangular shape is chosen for popularity and simplicity of triangular tessellation algorithms, simplification of new element's theory and the advantage of providing more paths for crack propagation compared to Voronoi blocks.

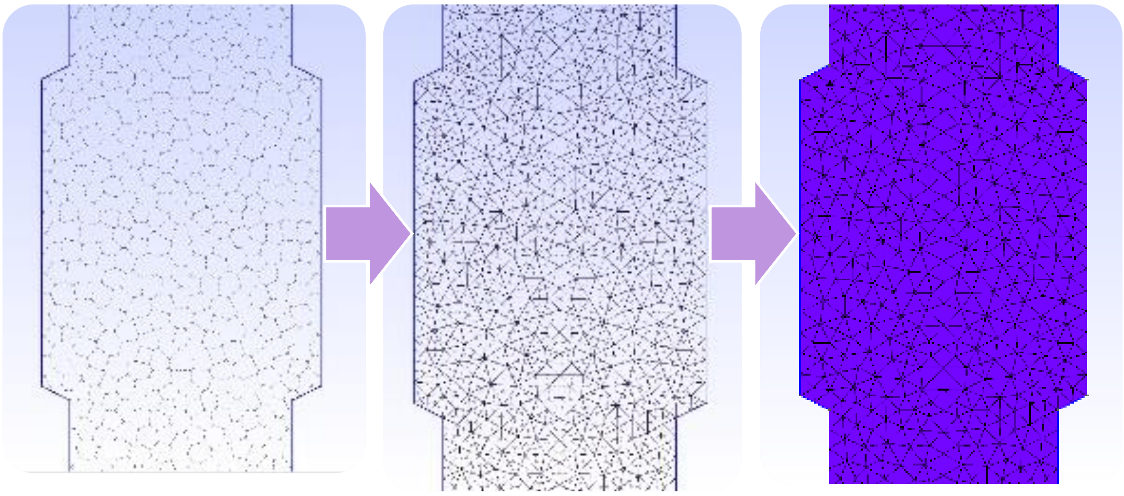

Figure 7. Triangular tessellation calculated from Voronoi diagram using open source software GMSH[26]: from left to right 1. Voronoi cells 2. Triangulation 3. Final mesh

The new element can be utilized for nonlinear applications and no extra iterations are required for obtaining Poisson effect in elastic applications. Another benefit of this element is the possibility of using two-dimensional plasticity models since a second normal force will be provided for each face of the element making it possible to calculate principal stresses and employing plasticity models in Haigh-Westergaard coordinates if such demand exists.

2.1. Assumptions

To derive the theory for the new triangular element with various forces acting on it, the displacement δ_p due to Poisson effect on arbitrary ridge, j, is calculated assuming that for only a normal stress acting on the bisector perpendicular fiber of ridge j, σ_j^{cut}, is required. In that case, as shown in Figure 8, δ_p can be calculated as

$$\delta_p = -\nu \frac{\sigma_j^{cut}}{E} = -\nu \frac{F_{cut}}{E L_j^{cut}} \qquad \text{Equation 8}$$

In which ν is the Poisson's ratio and E is the elastic modulus of the material, F_{cut} is the force acting on bisector fibre and L_j^{cut} is the length of the bisector fiber assuming the thickness of the element is unity.

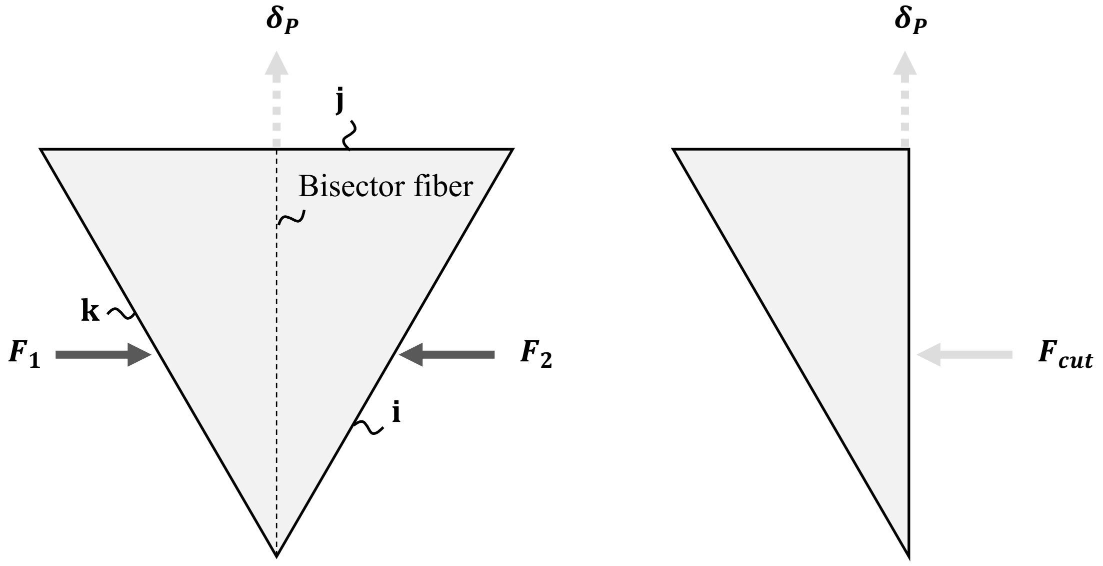

Figure 8. The basic theory of the new element for calculating deformations due to Poisson effect

Based on this concept it is possible to calculate strains due to Poisson effect on each ridge having the force on perpendicular bisector fibre for that ridge, F_{cut}, which will provide an orthogonal stress and make it possible to obtain Poisson deformation. To obtain a general stress-strain relationship, F_{cut} for a specific ridge j, is obtained by dividing the body using perpendicular bisector and writing the equilibrium for free body diagram (FBD) of one half (Figure 9). The forces in the FBD are assumed to be only due to stresses acting on the edges i, j and k; if there are forces acting on the centroid of the block (e.g. body forces), the F_{cut} will be different for each half, however in this research, no force is acting on the centroid of the elements and when prescribing boundary conditions are needed they are applied to the added DOFs (Degrees of Freedom) on the ridges of the rigid body.

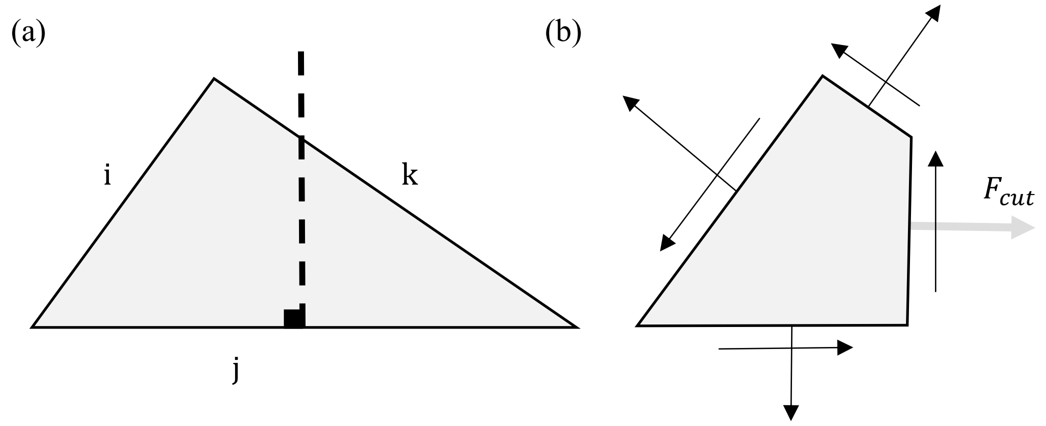

Figure 9. New element: a) bisector for ridge j b) obtaining the second normal stress from F_{cut} , for arbitrary ridge j to obtaine Poisson deformation

The relationship for the force on perpendicular bisector fibre of arbitrary ridge j, F_j^{cut} is given in Equation 9:

$$
\begin{aligned}
F_j^{cut} &= L_j^{cut}\sigma_j{}^{cut} \\
&= R_{jk}L_k\left(\sigma_k\cos\left(\pm\frac{\pi}{2}+\varphi_{jk}\right)+\tau_k\sin\left(\pm\frac{\pi}{2}+\varphi_{jk}\right)\right) \\
&+ R_{ji}L_i\left(\sigma_i\cos\left(\pm\frac{\pi}{2}+\varphi_{ji}\right)+\tau_i\sin\left(\pm\frac{\pi}{2}+\varphi_{ji}\right)\right) \\
&+ R_{jj}L_j\left(\sigma_j\cos\left(\mp\frac{\pi}{2}+\varphi_{jj}\right)+\tau_j\sin\left(\mp\frac{\pi}{2}+\varphi_{jj}\right)\right)
\end{aligned}
\qquad \textit{Equation 9}
$$

In which L_i, L_j and L_k are the lengths of ridges i, j and k respectively and with φ_{ij} to be equal to $\theta \times \xi_{ijk}$ in which θ is the angle between ridge i and j and ξ_{ijk} is the premutation symbol defined as if i, j and k where denoted by numbers 1 to 3 then

$$
\xi_{ijk} = \begin{cases} +1 & \text{if ijk is an even permutation of } 1,2,3 \\ -1 & \text{if ijk is an odd permutation of } 1,2,3 \\ 0 & \text{otherwise} \end{cases}
$$

Also σ_i, σ_j and σ_k are normal stresses and τ_i, τ_j and τ_k are the shear stresses on ridge i, j and k; the cosine and sine terms project σ_i, σ_j and σ_k and τ_i, τ_j and τ_k on the normal vector of the bisector fiber to calculate F_{cut} (Figure 9 (b)) and the sign of $\frac{\pi}{2}$ should be chosen accordingly depending on the direction bisector plane normal and the stresses.

In addition, R_{ij} is defined as

$$R_{ij} = \begin{cases} \dfrac{C_{ij}}{L_j cos\varphi_{ij}} & for\ C_{ij} > 0 \\ 1 & for\ C_{ij} < 0 \\ H(\varphi_{ij}) & for\ C_{ij} = 0 \end{cases} \qquad \text{Equation 10}$$

In which H is the Heaviside function and C_{ij} is defined as

$$C_{ij} = L_j \cos\varphi_{ij} - \frac{L_i}{2} \qquad \text{Equation 11}$$

Having calculated a secondary normal stress, σ_j^{cut}, using Equation 9, the stress due to Poisson effect on arbitrary ridge j can be simply obtained from

$$\begin{aligned} \varepsilon_{Poisson}^{j} &= -\frac{\nu}{E}\sigma_j^{cut} \\ &= -\frac{\nu}{E}\left(\Pi_{ji}\sigma_i + \Gamma_{ji}\tau_i + \Pi_{jj}\sigma_j + \Gamma_{jj}\tau_j + \Pi_{jk}\sigma_k + \Gamma_{jk}\tau_k\right) \end{aligned} \qquad \text{Equation 12}$$

in which Π_{ji} and Γ_{ji} are defined in [Equation]

$$\Pi_{ji} = \frac{R_{ji}L_i}{L_j^{cut}}\sigma_i \cos\left(\pm\frac{\pi}{2} + \varphi_{ji}\right) \qquad \text{Equation 13}$$

$$\Gamma_{ji} = \frac{R_{ji}L_i}{L_j^{cut}}\tau_i \sin\left(\pm\frac{\pi}{2} + \varphi_{ji}\right) \qquad \text{Equation 14}$$

Cosine and sine terms in above equations, again, calculate the projection of σ_i and τ_i on the normal vector of the bisector fiber to calculate F_{cut} and the sign of $\frac{\pi}{2}$ will depend on the arrangement of the stress vectors and direction of bisector normal.

Therefore, strain due to Poisson effect on one edge is a function of all stresses on all edges and the total normal strain on ridge j can be calculated from

$$\varepsilon_j = \frac{1}{E}\sigma_j - \frac{\nu}{E}\left(\Pi_{ji}\sigma_i + \Gamma_{ji}\tau_i + \Pi_{jj}\sigma_j + \Gamma_{jj}\tau_j + \Pi_{jk}\sigma_k + \Gamma_{jk}\tau_k\right) \qquad \text{Equation 15}$$

2.2. Evaluation of deformations from strains

In the concept of the new element, just like the concept used in RBSM, zero-length springs are connecting the rigid bodies. The stiffness of the zero-length normal spring, K_n^{spring}, is equal to EA/h, where E is the elastic modulus of the material, A is the area of the rigid block face ($A = L_{ridge} \times 1$, L_{ridge} being the length of the ridge and 1 being the thickness of the element, assumed to be unity), and h is the normal distance between the ridge and the centroid of the rigid block. The idea of the zero-length springs may cause confusion with evaluating deformations in the first place; however, it is important to notice that it is the stiffness of equivalent spring that connect the DOFs is being assembled on the stiffness matrix not the stiffness of zero length springs. Equivalent spring are made up of the zero-length spring and a rigid part representing the rigid block connected with series arrangement; this equivalent spring connects the DOF on the surface to the DOF on the centroid (Figure 10). The stiffness of equivalent normal spring can be obtained from:

$$\frac{1}{K_n} = \frac{1}{K_{rigid}} + \frac{1}{K_n^{spring}} = \frac{1}{\infty} + \frac{1}{EA/h} \Rightarrow K_n = \frac{EA}{h} = \frac{EL_{ridge}}{h} \qquad \textit{Equation 16}$$

In other words, the stiffness of equivalent normal spring is same as the stiffness of the zero-length normal spring, while its length being equal to normal distance between the corresponding ridge and the centroid of the rigid block.

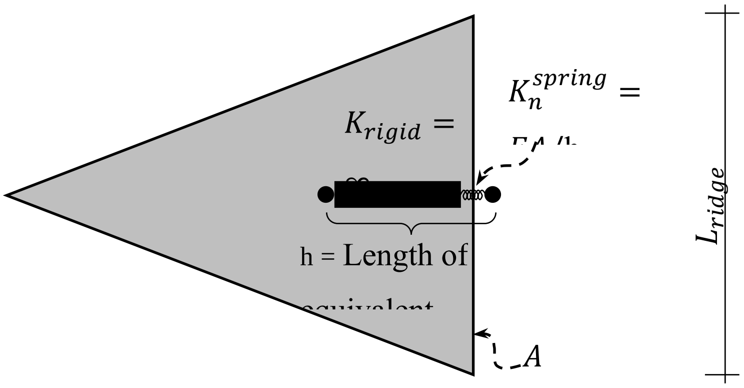

Figure 10. Equivalent normal spring

Having the strains, to calculate the deformation of springs, for the case of normal strains, the length that must be used to evaluate the normal deformation of an arbitrary ridge is the length of the equivalent normal spring (i.e. h). For example, in the case of arbitrary ridge j the normal deformation u_j is:

$$u_j = h_j \times \varepsilon_j \qquad \textit{Equation 17}$$

In all equations above, for arbitrary ridge j, h_j can be evaluated using:

$$h_j = \mid 1/3 \times L_i sin\varphi_{ji} \mid = \mid 1/3 \times L_k sin\varphi_{jk} \mid \qquad \textit{Equation 18}$$

On the other hand, for the case of shear springs (Figure 1), if an infinitesimal shear deformation is considered, having the shear strain of an arbitrary ridge j, ε_{sj}, it is possible to calculate the deformation of the shear spring, v_j, using:

$$v_j = h_j \times \varepsilon_{sj} \qquad \textit{Equation 19}$$

Therefore, h_j, can be considered as spring length for both normal and shear springs.

2.2.1. Stress and strain vectors and the stress-strain relationship matrix

The stress-strain relationship matrix, [D], will convert the strain vector $\{\varepsilon\}$ into stress vector $\{\sigma\}$. In other words, for each member of $\{\varepsilon\}$, there will be a corresponding member in $\{\sigma\}$ obtained from $\{\sigma\} = [D]\{\varepsilon\}$. To derive the [D], first the orthonormal vectors that define strain and stress vectors, $\{\varepsilon\}$ and $\{\sigma\}$, are defined for any arbitrary element (Figure 11). In the centroid of each ridge of the triangle one normal and one shear (tangential direction) strain is assumed and each ridge has its own local coordinates defined by unity vectors, $\vec{\imath}$ and $\vec{\jmath}$ (to prevent confusion with local vectors, $\vec{\imath}$ and $\vec{\jmath}$, ridge indexes i, j and k are relabeled with numbers 1, 2 and 3 respectively). $\vec{\imath}$ corresponds to the positive direction for normal stress while $\vec{\jmath}$ represents positive direction for shear stress of each ridge. Therefore the $\{\varepsilon\}$ contains six members representing three normal (ε_1, ε_2 and ε_3) and three shear strains (ε_{s1}, ε_{s2} and ε_{s3}) which correspond to normal and shear springs on each ridge (Figure 11). In a similar way, stress vector, $\{\sigma\}$, will also have 6 members for normal and shear stresses accordingly (Equation 20).

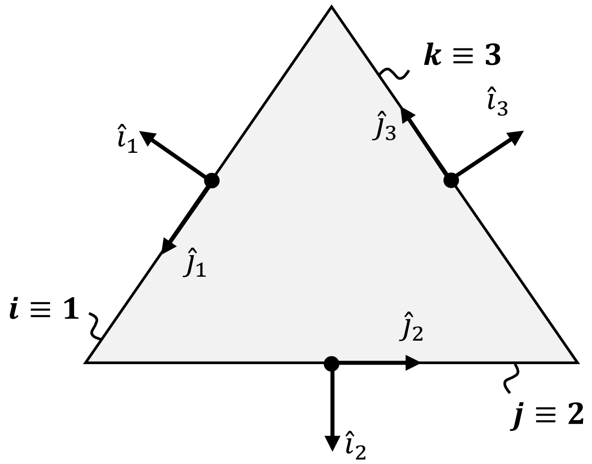

Figure 11. Local coordinates for normal and shear strains

From Equation 15 the inverse of stress strain relationship matrix, $[\boldsymbol{D}]^{-1}$, can be derived as given in Equation 21.

$$\{\varepsilon\} = [D]^{-1}\{\sigma\}, \qquad \{\varepsilon\} = \begin{Bmatrix} \varepsilon_1 \\ \varepsilon_2 \\ \varepsilon_3 \\ \varepsilon_{s1} \\ \varepsilon_{s2} \\ \varepsilon_{s3} \end{Bmatrix}, \qquad \{\sigma\} = \begin{Bmatrix} \sigma_1 \\ \sigma_2 \\ \sigma_3 \\ \tau_1 \\ \tau_2 \\ \tau_3 \end{Bmatrix} \qquad \textit{Equation 20}$$

- $[\boldsymbol{D}]^{-1} =$

$$\begin{bmatrix} \frac{1}{E} & -\frac{\nu}{E}\Pi_{12} & -\frac{\nu}{E}\Pi_{13} & -\frac{\nu}{E}\Gamma_{11} & -\frac{\nu}{E}\Gamma_{12} & -\frac{\nu}{E}\Gamma_{13} \\ -\frac{\nu}{E}\Pi_{21} & \frac{1}{E} & -\frac{\nu}{E}\Pi_{23} & -\frac{\nu}{E}\Gamma_{21} & -\frac{\nu}{E}\Gamma_{22} & -\frac{\nu}{E}\Gamma_{23} \\ -\frac{\nu}{E}\Pi_{31} & -\frac{\nu}{E}\Pi_{32} & \frac{1}{E} & -\frac{\nu}{E}\Gamma_{31} & -\frac{\nu}{E}\Gamma_{32} & -\frac{\nu}{E}\Gamma_{33} \\ 0 & 0 & 0 & \frac{1+\nu}{E} & 0 & 0 \\ 0 & 0 & 0 & 0 & \frac{1+\nu}{E} & 0 \\ 0 & 0 & 0 & 0 & 0 & \frac{1+\nu}{E} \end{bmatrix}$$

Equation 21

It is possible to derive $[\boldsymbol{D}]$ matrix formulation by an implicit inversion of $[\boldsymbol{D}]^{-1}$ from Equation 56, however in the current research, $[\boldsymbol{D}]$ is calculated by first evaluating $[\boldsymbol{D}]^{-1}$ from Equation 56 and then obtaining $[\boldsymbol{D}]$ by an explicit matrix inversion of $[\boldsymbol{D}]^{-1}$.

2.2.2. Deriving the stiffness matrix

Global displacements and deformations

For the current element, the global displacement matrix, $\{d\}$, is assumed to contain 9 members as depicted in Figure 12 and Equation 22; with u_o, v_o and ϕ_o being the displacement and rotation of the rigid body and u_1, v_1, …, u_3, v_3 the displacements of DOFs on the ridges (Figure 12).

$$\{d\} = \begin{Bmatrix} u_o \\ v_o \\ \phi_o \\ u_1 \\ v_1 \\ u_2 \\ v_2 \\ u_3 \\ v_3 \end{Bmatrix}$$

Equation 22

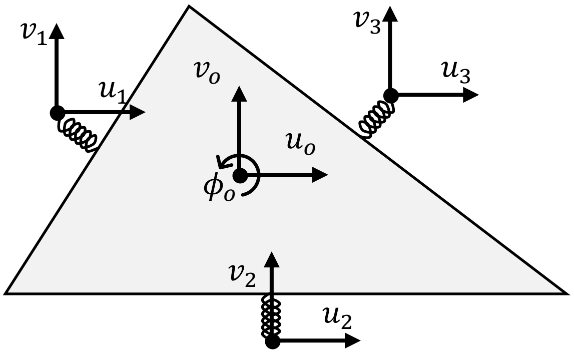

Figure 12. Global displacement vector definition

To evaluate the deformation of the element, deformation vector, $\{u\} = [N]\{d\}$, is defined (in which, as depicted in Figure 13 (a), the rotation of rigid body is converted to displacement on the ridges [27]):

$$\{u\} = \begin{Bmatrix} u_1^s \\ v_1^s \\ u_1 \\ v_1 \\ u_2^s \\ v_2^s \\ u_2 \\ v_2 \\ u_3^s \\ v_3^s \\ u_3 \\ v_3 \end{Bmatrix}, [N] = \begin{bmatrix} 1 & 0 & \Delta y_1 & 0 & 0 & 0 & 0 & 0 & 0 \\ 0 & 1 & -\Delta x_1 & 0 & 0 & 0 & 0 & 0 & 0 \\ 0 & 0 & 0 & 1 & 0 & 0 & 0 & 0 & 0 \\ 0 & 0 & 0 & 0 & 1 & 0 & 0 & 0 & 0 \\ 1 & 0 & \Delta y_2 & 0 & 0 & 0 & 0 & 0 & 0 \\ 0 & 1 & -\Delta x_2 & 0 & 0 & 0 & 0 & 0 & 0 \\ 0 & 0 & 0 & 0 & 0 & 1 & 0 & 0 & 0 \\ 0 & 0 & 0 & 0 & 0 & 0 & 1 & 0 & 0 \\ 1 & 0 & \Delta y_3 & 0 & 0 & 0 & 0 & 0 & 0 \\ 0 & 1 & -\Delta x_3 & 0 & 0 & 0 & 0 & 0 & 0 \\ 0 & 0 & 0 & 0 & 0 & 0 & 0 & 1 & 0 \\ 0 & 0 & 0 & 0 & 0 & 0 & 0 & 0 & 1 \end{bmatrix}$$

Equation 23

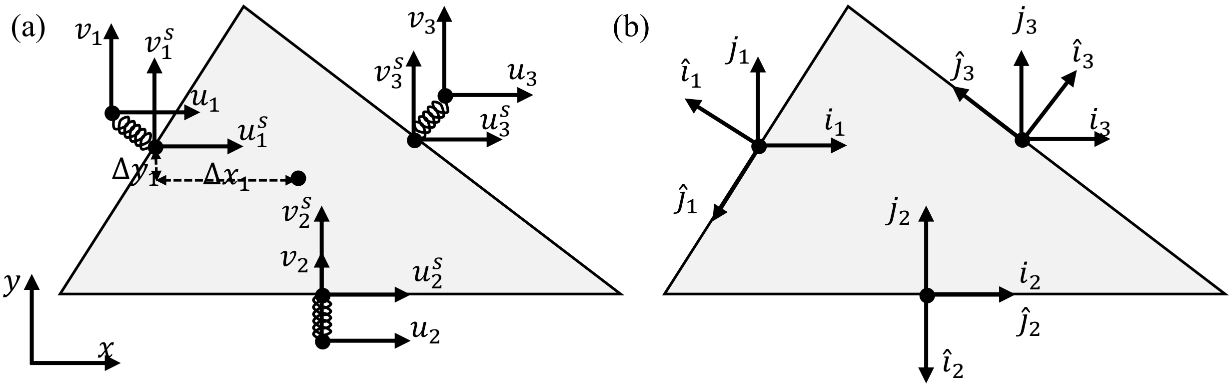

Figure 13. definition of deformations a) global deformation vector b) conversion of global deformations to deformations in local coordinates

Rotation matrix

Rotation matrix, denoted by $[T]$, is used to perform conversion from global deformations, $\{u\}$, to local deformations, denoted by $\{\hat{u}\}$.

$$[T] =$$

$$\begin{bmatrix} \hat{\imath}_1.i_1 & \hat{\imath}_1.j_1 & & & & & & & \\ \hat{\jmath}_1.i_1 & \hat{\jmath}_1.j_1 & & & & & & & \\ & & \hat{\imath}_1.i_1 & \hat{\imath}_1.j_1 & & & & & \\ & & \hat{\jmath}_1.i_1 & \hat{\jmath}_1.j_1 & & & & & \\ & & & & \hat{\imath}_2.i_2 & \hat{\imath}_2.j_2 & \cdots & & \\ & & & & \hat{\jmath}_2.i_2 & \hat{\jmath}_2.j_2 & & & \\ & & & & \vdots & & \ddots & \vdots & \\ & & & & & & \cdots & \hat{\imath}_3.i_3 & \hat{\imath}_3.j_3 \\ & & & & & & & \hat{\jmath}_3.i_3 & \hat{\jmath}_3.j_3 \end{bmatrix}_{12\times12} \qquad \textit{Equation 24}$$

In Equation 24, dot operator, denotes internal vector product, and i, j, $\hat{\imath}$ and $\hat{\jmath}$ are unity vectors representing the global and local coordinate systems on each ridge as depicted in Figure 13 (b).

2.2.3. Displacement to strain conversion matrix

The global displacement to strain matrix is denoted by $[B]$:

$$\{\boldsymbol{\varepsilon}\} = [\mathbf{B}]\{\mathbf{d}\} \qquad \textit{Equation 25}$$

To evaluate $[B]$ matrix, $[\hat{B}]$ and $[B^*]$ are defined as:

$$\{\boldsymbol{\varepsilon}\} = \left[\widehat{\mathbf{B}}\right]\{\widehat{\mathbf{u}}\} = \left[\widehat{\mathbf{B}}\right][\mathbf{T}]\{\mathbf{u}\} = [\mathbf{B}^*]\{\mathbf{u}\} = [\mathbf{B}^*][\mathbf{N}]\{\mathbf{d}\} \qquad \textit{Equation 26}$$

$$\left[\hat{B}\right] =$$

$$\begin{bmatrix} -1/h_1 & 0 & 1/h_1 & 0 & 0 & 0 & 0 & 0 & 0 & 0 & 0 \\ 0 & 0 & 0 & 0 & -1/h_2 & 0 & 1/h_2 & 0 & 0 & 0 & 0 \\ 0 & 0 & 0 & 0 & 0 & 0 & 0 & -1/h_3 & 0 & 1/h_3 & 0 \\ 0 & -1/h_1 & 0 & 1/h_1 & 0 & 0 & 0 & 0 & 0 & 0 & 0 \\ 0 & 0 & 0 & 0 & 0 & -1/h_2 & 0 & 1/h_2 & 0 & 0 & 0 \\ 0 & 0 & 0 & 0 & 0 & 0 & 0 & 0 & -1/h_3 & 0 & -/h_3 \end{bmatrix} \qquad \textit{Equation 27}$$

$$[B^*] = [\hat{B}][T] \qquad \textit{Equation 28}$$

Using Equation 25 to Equation 28 it is evident that

$$[B] = [B^*][N] = [\hat{B}][T][N] \qquad \textit{Equation 29}$$

Local stiffness matrix

But employing a conventional method to derive the stiffness matrix (e.g. minimum potential energy), the Equation 30 will be obtained for deriving the local stiffness matrix, $[\hat{k}]$.

$$[\hat{k}] = [B]^T[V][D][B] \qquad \textit{Equation 30}$$

Where $[M]^T$ indicates the transpose of the matrix $[M]$ and $[V]$ is volume matrix of the springs which for a triangular rigid body with three normal and three shear springs is a six by six diagonal matrix obtained from Equation 31; in which again, the thickness of element is assumed to be unity.

$$[v] = \begin{bmatrix} h_1 * L_1 & & & & & \\ & h_2 * L_2 & & & & \\ & & h_3 * L_3 & & & \\ & & & h_1 * L_1 & & \\ & & & & h_2 * L_2 & \\ & & & & & h_3 * L_3 \end{bmatrix} \qquad \textit{Equation 31}$$

Having local stiffness evaluated for every element, the global stiffness will be obtained by assembling the local stiffness matrices along with additional rotational stiffness to account for resisting moment due to variation of normal stress on each ridge (Figure 2). Since shear springs provide rotational stiffness of rigid blocks this extra rotational resistance is often ignored (e.g. [9,18]) but even in this case a minimum extra rotational stiffness is necessary to ensure stability of the model, however in the new triangular element an extra rotational stiffness evaluated from Equation 32 is assembled on the global stiffness matrix.

$$M = \sum_{1}^{3} \frac{L_i^3 E}{12 h_i} \qquad \textit{Equation 32}$$

2.3. Validation of Proposed Element

To verify the behaviour of the proposed element, a square shaped prism is analysed. The model is assumed to be a 100mm by 100mm specimen. The specimen is triangulated with element size of approximately 10mm. To create the model and visualize the outcome an opensource software named GMSH [26] which has integrated pre/post-processing facilities is employed.

The boundary condition is prescribed displacement, δ, in negative direction of y axis on top surface (assigned to the top ridge of the rigid elements), zero vertical displacement at the bottom of specimen (assigned to the lower ridge of rigid element), and finally zero horizontal displacement on the left side (assigned to the left ridge of rigid elements). The right side of the model is left free to allow deformations due to Poisson effect. The model and boundary conditions are depicted in Figure 14.

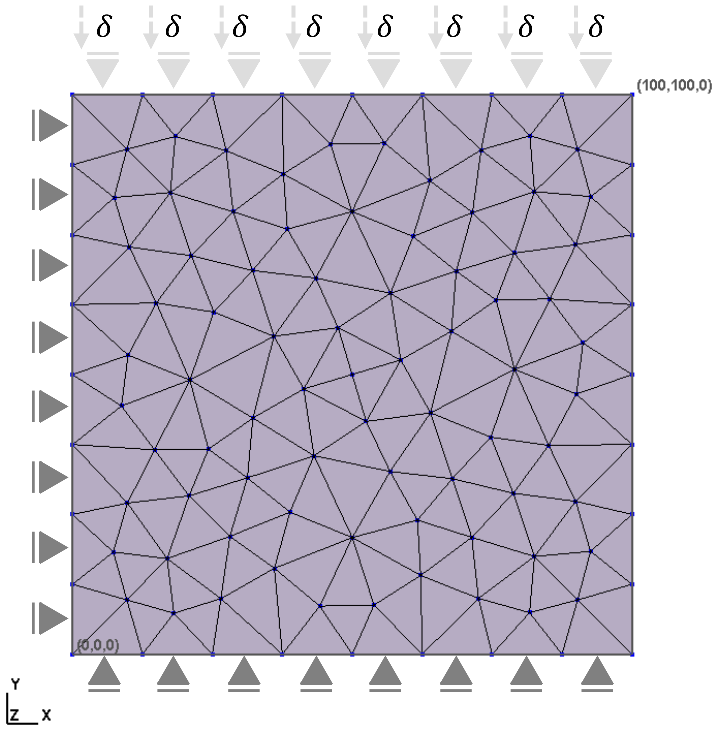

Figure 14. Meshing and the boundary condition of the model

The material is assumed to have mechanical properties close to concrete at elastic stage. Therefore, the assumed properties are elastic modulus of $E = 20{,}000$ MPa and Poisson's ration of $\nu = 0.2$.

The analysis results show that the deformation of the model meets the expected value with respect to the assigned Poisson's ratio, i.e. the horizontal deformation of the modelled specimen for the vertical deformation of 10mm is 2mm (which is same as $\nu \times \delta = 0.2 \times 10mm = 2mm$). The deformation of the model is depicted in Figure 15a. The elements in this figure are shrunk for better vision while the network of the springs is depicted over the rigid bodies. For the sake of comparison, the Poisson's ratio along the height of a similar model analysed by RBSM is presented in Figure 15b. It should be noted that the fluctuation in the height of the RBSM model is due to the fact that the lateral deformations of due to Poisson effect are recreated in the RBSM by shear deformations and therefore are dependent on the mesh configurations and therefore less accurate in comparison to RBCS.

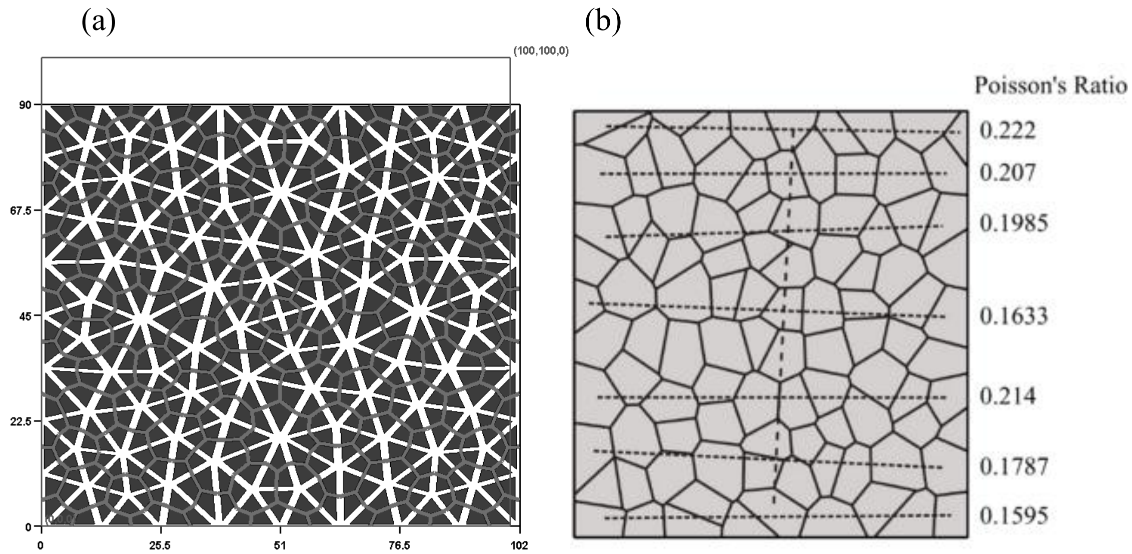

Figure 15. Representing the Poisson effect, a) RBCS model (dimensions are in mm) b) RBSM model

The proposed element in this chapter is used for simulation of nonlinear behaviour of concrete in Chapter 3.

2.4. Simulation of incompressible materials

RBCS supports simulation of incompressible materials. In the study field related to construction industries, this ability can be useful in the study of materials comprise incompressible ingredients like rubber. Use of waste rubber in concrete to produce rubberized concrete is known as one of the solutions for the problem of huge number of tyres thrown away as waste each year. Numerical simulations like XFEM (extended finite element method) has been used as a tool to simulate rubberized concrete but they come with limitations of capturing the fracture since they usually have limited number of cracks they can simulate and also the location of the cracks should be given to the solver. This weak point in the continuum-based techniques is the strong point when it comes to discrete models. However it is obvious that an accurate simulation of Poisson’s ratio is crucial in the case of simulating incompressible materials. There is no limitation in RBCS for simulating incompressible materials. Figure 16 depicts simulation of an elastic material with Poisson’s ratio of 0.5. The induced deformation 4mm to a 100mm by 100mm square is simulated in a linear elastic analysis. It can be observed that the simulation is performed accurately with no problem. It should be noted that it is not stated here that the RBCS or other discrete models are more suitable for simulation of rubber or other form of materials such as steel compared to the continuum mechanics numerical techniques such as FEM, but rather the possibility of simulation using RBCS is pointed out.

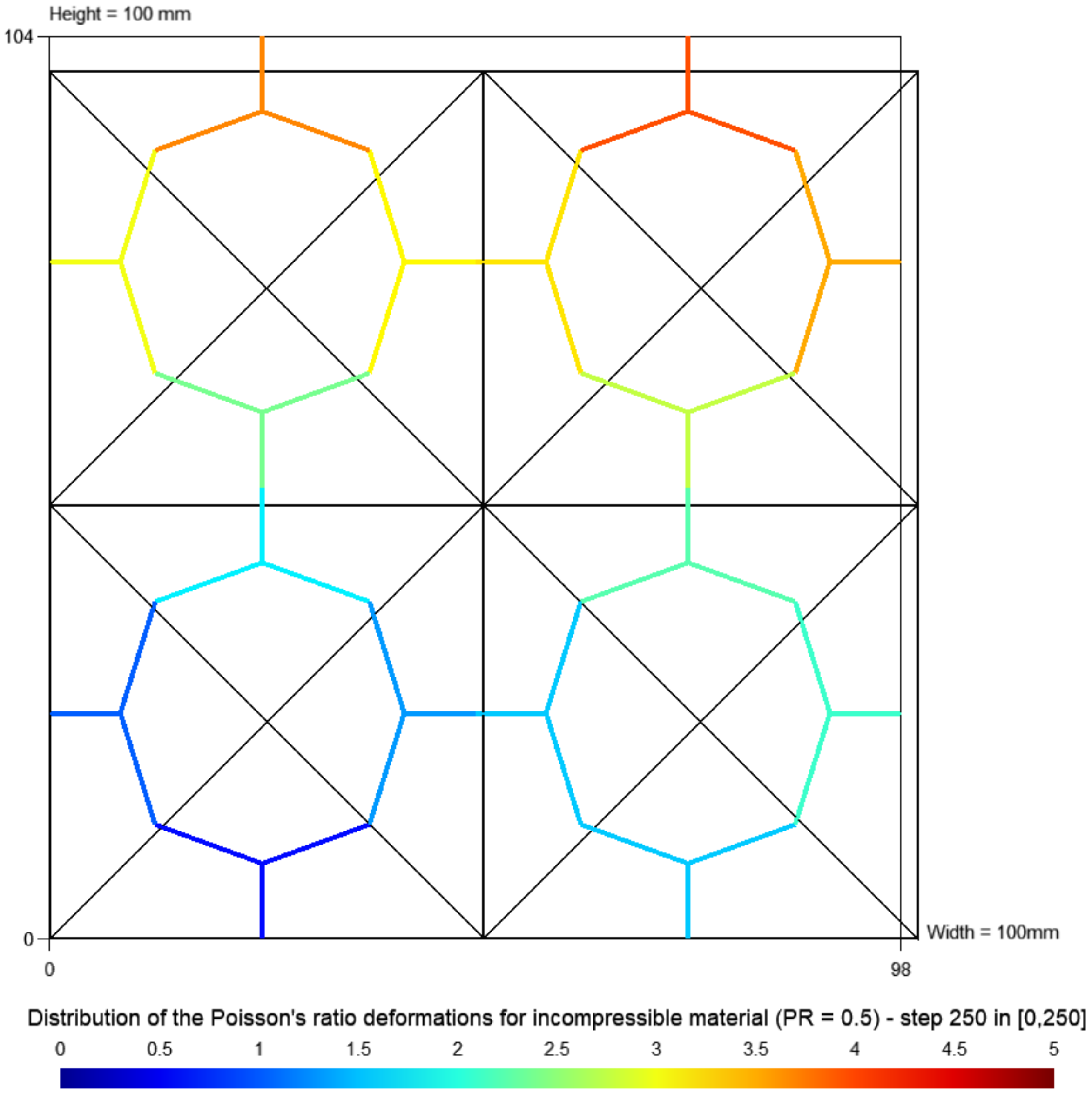

Figure 16. Simulation of incompressible material using RBCS

It should be noted that the for the RBSM method proposed by Nagai et al., the Poisson's ratio of the material is limited to maximum value of 0.3. However this is not a limitation related to the method itself but it is rather the accurate range of the empirical equations proposed by Nagai et al. [18,28,29].

2.5. Visualization of stress field

Depiction of stress field on the simulated volume can be crucial for the purpose of studying and making conclusions about the behaviour material and the simulated case. One of the main disadvantages with the RBSM is that the stresses cannot be properly depicted in the model. For example, the stresses for a uniform and uniaxial compressive case is obtained from RBSM model is depicted in figure#. As it can be observed instead of an uniform compressive stress distribution a severe variation of stress is depicted as the stress of the specimen in RBSM. The issue is that the RBSM cannot obtain the stress in a global direction and tries to give stress results simply using the stress in normal springs which have a random orientation and this stress is presented as the stress in the vicinity of that spring. This method of evaluating stresses is not reliable and has to be addressed.

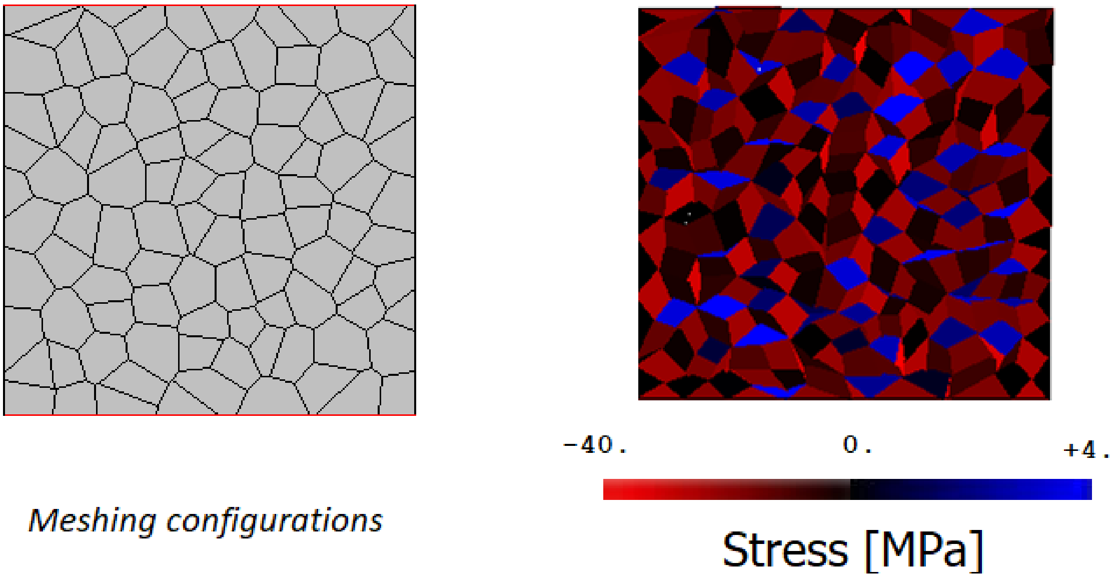

Figure 17. Stress calculation issue in RBSM

As an alternative to the stresses in the elements, the forces or stresses in the springs are usually used as a representative of the stress in the model. The issue with this approach is that all the spring have random alignments and cannot be a reliable representative of the stress since to make useful information all the stresses should be in the same direction or should be principal stresses.

One of the benefits of RBCS as an alternative to the original RBSM is the ability to depict stress contours on the model and in any desired direction as well as the ability to calculate and depict principal stresses. In this section this procedure is explained.

The main difference between RBCS and RBSM is that RBCS takes orthogonal stresses into account while RBSM simply ignores them. As explained before this ability is implemented into inverse stress-strain relationships matrix (i.e. $[\mathbf{D}]^{-1}$) between ridges. It is possible to decompose the first three rows of $[\mathbf{D}]^{-1}$ (denoted as $[\mathbf{D}]^{-1}_{(1:3,:)}$) into two parts:

$$[\mathbf{D}]^{-1}_{(1:3,:)} = [\mathbf{D}]^{-1}_{diag(1:3,:)} - \frac{\nu}{E}[\mathbf{C}]$$ *Equation 33*

In which $[\mathbf{C}]$ is a 3×6 rectangular matrix calculating the orthogonal stresses and $[\mathbf{D}]_{diag}^{-1}$ is a rectangular matrix with same diagonal members as $[\mathbf{D}]_{diag(1:3,:)}^{-1}$. The matrix $[\mathbf{C}]$ is depicted in Equation 34Equation 21.

- $$[\mathbf{C}] = \begin{bmatrix} 0 & \Pi_{12} & \Pi_{13} & \Gamma_{11} & \Gamma_{12} & \Gamma_{13} \\ \Pi_{21} & 0 & \Pi_{23} & \Gamma_{21} & \Gamma_{22} & \Gamma_{23} \\ \Pi_{31} & \Pi_{32} & 0 & \Gamma_{31} & \Gamma_{32} & \Gamma_{33} \end{bmatrix}$$ *Equation 34*

The orthogonal stresses of element can be calculated from Equation 35:

- $$\{\boldsymbol{\sigma}\}_{\mathbf{ortho}} = [\mathbf{C}]\{\boldsymbol{\sigma}\}$$ *Equation 35*

in which $\{\boldsymbol{\sigma}\}_{\mathbf{ortho}}$ is a vector with dimension 3 containing orthogonal stresses of each ridge in the element.

Having the orthogonal stresses on each ridge it is possible to calculate the stresses in desired direction. For instance, the stresses toward global X axis direction depicted by $\vec{\imath}$ unity vector (σ_X) can be evaluated from

- $$\sigma_X = \sigma_n l^2 + \sigma_{orth} m^2 + 2\,\tau\,l\,m$$ *Equation 36*

and stresses toward global X and Y axis (σ_X and σ_Y) can be evaluated from

- $$\sigma_X = \sigma_n m^2 + \sigma_{orth} l^2 + 2\,\tau\,l\,m$$ *Equation 37*

- $$\sigma_Y = \sigma_n m^2 + \sigma_{orth} l^2 - 2\,\tau\,l\,m$$ *Equation 38*

in which l and m respectively are cosine and sine of the angle between normal vector of the ridge and direction which stress is being to be calculated.

In a similar manner the principal stresses can be evaluated as:

- $$\sigma_{max} = \frac{\sigma_n + \sigma_{orth}}{2} + \sqrt{\frac{(\sigma_n - \sigma_{orth})^2}{4} + \tau^2}$$ *Equation 39*

- $$\sigma_{min} = \frac{\sigma_n + \sigma_{orth}}{2} - \sqrt{\frac{(\sigma_n - \sigma_{orth})^2}{4} + \tau^2}$$ *Equation 40*

The desired stress for the element can be evaluated using a shape function or simply averaging the stresses of the ridges.

The Figure 18 depicts the stress in Y direction (the direction of the applied displacement) of a simple model which is evaluated from Equation 38 for each ridge and averaged to represent the stress value for each element as described above.

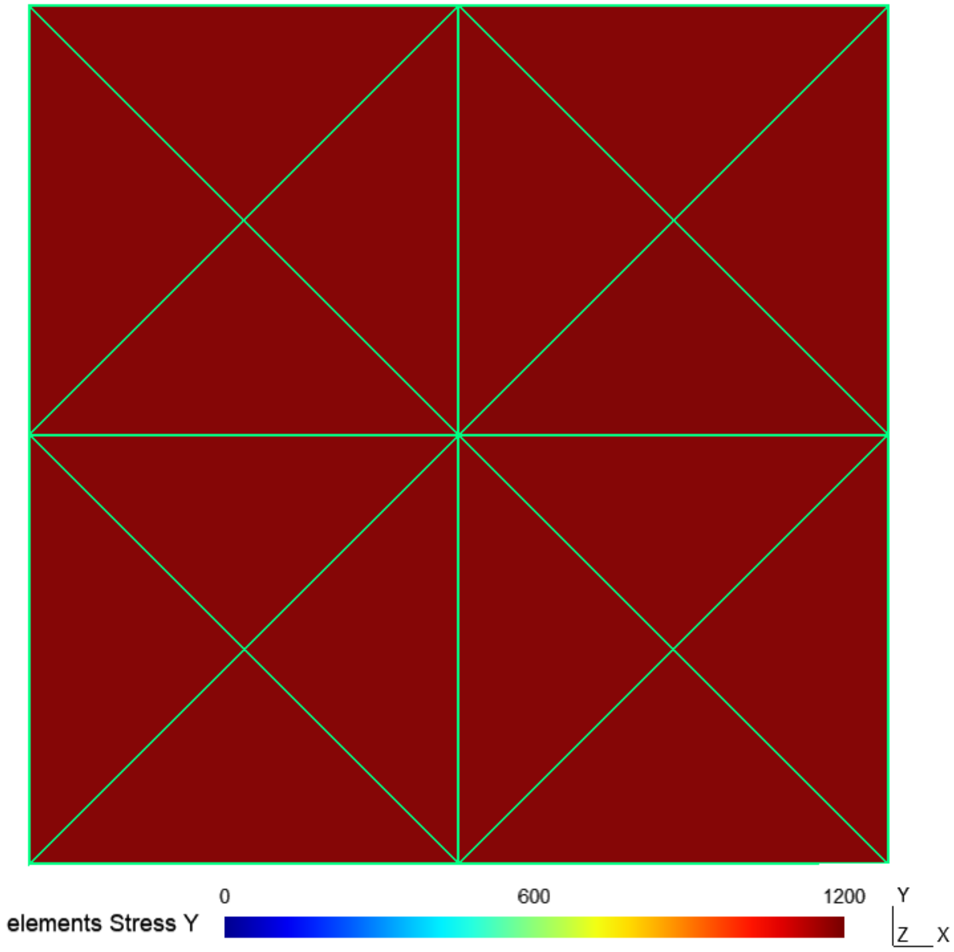

Figure 18. Stress contour depiction of a simple model (expected stress for all elements is 1200MPa)

2.6. Bottom line

Developing a new discrete element base on RBSM method which can incorporate the Poisson effect accurately without modification of input mechanical properties or extra iterations (which could make the procedure of nonlinear calculations cumbersome) was one of the mains goals of this study which is achieved in this chapter.

The lateral deformation in the model created using the new element, referred to as RBCS element, were properly distributed within the height of the model with a much more accuracy compared to the RBSM model. Furthermore, the ability to simulate the non-compressive material such as rubber with Poisson's ratio of 0.5 is another merit of the proposed element.

Other outstanding goals that are achieved in this chapter are the ability to calculate and visualize the principal stresses as well as the stresses in a specific direction such as X or Y direction. This will generate more reliable result compared to the existing RBSM method which cannot calculate the principal stresses and uses the stresses at the normal springs to visualize the stress values.

It is worth mentioning that the integration with a standard and opensource pre/post-processing software has made the definition of the model and post-processing of the results much easier and it is possible to visualize the distribution of the displacements in the model which should make it possible to highlight cracking or produce informative figures from the analysis results.

Chapter 3

Applying RBCS into Simulation of Concrete

In this chapter, the proposed element in Chapter 2 is implemented into nonlinear simulation of plain concrete. To assess the new RBCS element in simulation of nonlinear behaviour of concrete, nonlinear material models are developed similar to what briefly discussed in section 1.5 of Chapter 1. In the next section the implemented material models into RBCS element are described in detail following that the case studies and analysis results are presented.

3.1. Material model of concrete for RBCS element

In the mesoscopic modelling technique, the nonlinearity of the models is assumed to come from the formation of the cracks in the material. At the location of the cracks there are normal and shear deformation. These deformations are reflected in the behaviour of normal and shear springs. Micro-cracks that are smaller to be covered in the macro-scale can cause nonlinearity before the cracking in meso-scale appear should also be reflected by nonlinear behaviour of springs. To have the model resemble the behaviour of concrete like material specific material models are applied to the spring. The behaviour implemented in springs is referred to as mesoscopic behaviour while the assembly of all elements together will create a macroscopic behaviour. The goal is that the model as a whole show a similar behaviour to the real material under similar conditions. In other words, the criteria of selecting the mesoscopic material models is the overall (macroscopic) behaviour of the model (behaviour in macro-scale). In this section implemented mesoscopic material models are described. In the further sections the behaviour of the model is put into test to investigate the macroscopic behaviour of the model and compare it with the behaviour of concrete like materials.

3.1.1. Material model for normal springs

The concept of normal spring behaving elastically in compression is implemented in the new material model as well. When subject to tensile deformations however, the element may go through softening. To allow the model to have remaining plastic deformations in tension, the concept of focal point is employed into the normal springs. The mentioned concept was previously employed by Ueda et al. [30].

Beside the normal springs, depending on the arrangement of elements, the shear springs will also contribute to the tensile failure (Figure 19) therefore, the macroscopic behaviour in tension is not necessarily same as the mesoscopic material model given to tensile springs. The maximum stress for the tensile springs (σ_t^c) is evaluated in a way to create the correct tensile strength in macro-scale (Equation 41). The complete tensile failure strain (at which the stress of normal springs becomes zero) is denoted by ε_t^u, and is assumed to be ten times of the strain associated with peak tensile stress (ε_t^c) as given in Equation 42. Material model of tensile springs is depicted in Figure 20.

$$\sigma_t^c = 1.75\left(\frac{f_c'}{10}\right)^{2/3} \qquad f_c' \text{ is in MPa}$$ *Equation 41*

$$\varepsilon_t^u = 10 \times \varepsilon_t^c$$ *Equation 42*

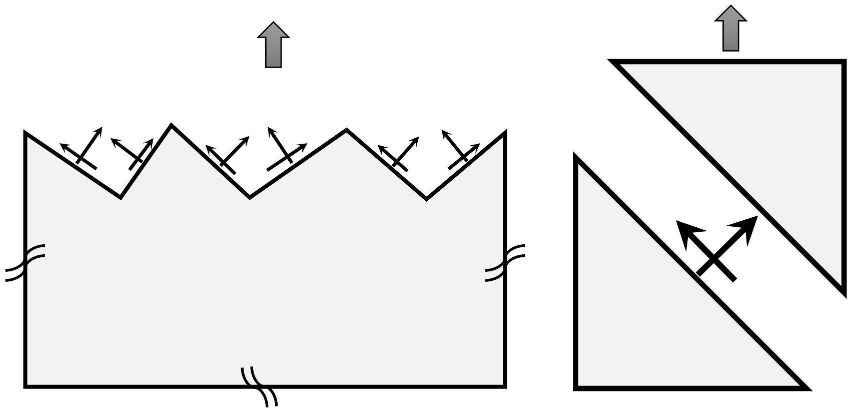

Figure 19. Interaction of normal and shear springs in case of tension force

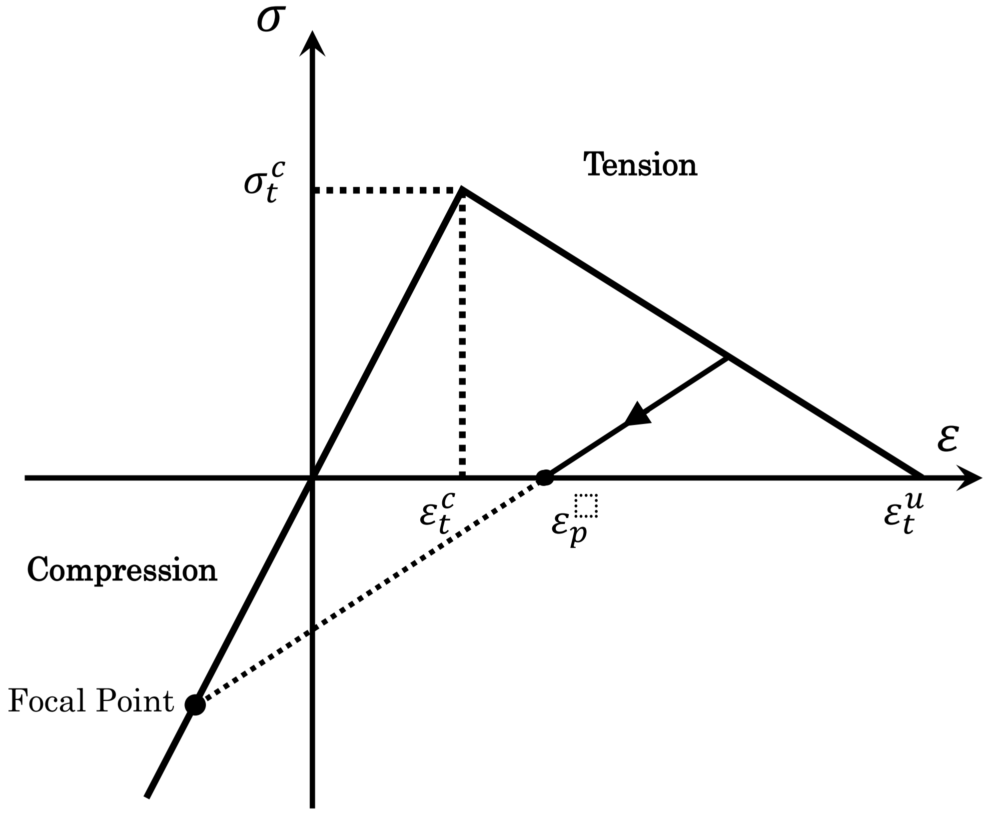

Figure 20. Material model for tensile springs

3.1.2. Material model for shear springs

Since in the concept of normal springs there is no possibility of failure, the failure of the model in compression is made possible by failure in shear and tensile springs. The mesoscopoic nonlinear behaviour of for shear springs is derived based on the macroscopic behaviour of concrete in uniaxial compression test. For this purpose authors have chosen the first part of the compressive stress-strain model suggested in CEB-FIP model code 1990 [24] which represent the behaviour of the concrete before and peak and early stages after peak up to a so called limit compressive strain. This model suggests a rather brittle post-peak behaviour compared to some other models used for this purpose. To obtain a similar macroscopic behaviour, considering that the normal springs are behaving linearly in compression, initially a similar nonlinear behaviour is considered for shear springs and a relation for tangent shear modulus is derived based. The initial form of the behaviour is recalibrated and validated until the appropriate macroscopic behaviour is attained.

Similar to the RBSM, the deformation in shear springs represent half of the shear deformation [4] the stiffness of the shear springs is derived using doubled shear modulus (two times shear modulus). In this manuscript to simplify annotation, the doubled shear modulus is depicted with $\breve{G}$ (i.e. $\breve{G} = 2G = E/(1+\nu)$) and simply referred to as shear modulus.

At early stages of loading, shear springs behave elastically with a shear modulus equal to G_0 obtained from elastic modulus of the material until the ratio of shear stress to maximum shear strength of springs reaches the designated linear behaviour limit of $r_1 = 0.3$. As the compressive deformations increase the hardening and softening stages of the concrete is simulated by using a reduced tangent shear modulus, $\breve{G}_t$ (Equation 43).

$$\breve{G}_t = -c_m \frac{(r_\mathrm{E}-2)\left(\frac{\varepsilon_s}{\varepsilon_{sc}}\right)^2 + 2\left(\frac{\varepsilon_s}{\varepsilon_{sc}}\right) - r_\mathrm{E}}{\varepsilon_{sc}\left((r_\mathrm{E}-2)\left(\frac{\varepsilon_s}{\varepsilon_{sc}}\right)+1\right)^2} \beta\alpha v_c \, \varepsilon_s < \varepsilon_{s\,lim}$$

$$\breve{G}_t = -c_m \frac{(r_\mathrm{E}-2)(r_{lim})^2 + 2(r_{lim}) - r_\mathrm{E}}{\varepsilon_{sc}\left((r_\mathrm{E}-2)(r_{lim})+1\right)^2} \beta\alpha v_c \qquad \varepsilon_s \geq \varepsilon_{s\,lim}$$

Equation 43

In the Equation 43, ε_s is the strain in the shear spring (not smaller than remaining plastic strain in shear springs). As mentioned earlier the first part of compressive stress-strain model used to derive the main part of Equation 43 is meant up the early stages after peak. Therefore, $\varepsilon_{s\,lim}$ is used to limit the separate the behaviour of the shear spring in later stages of loading. For $\varepsilon_s \geq \varepsilon_{s\,lim}$ the $\breve{G}_t$ is assumed to be constant and evaluated from second part of Equation 43. In Equation 43, $\varepsilon_{s\,lim}$ *and* ε_{sc} are defined as

$$\varepsilon_{s\,lim} = \varepsilon_{sc} \times r_{lim}$$

Equation 44

With r_{lim} defined as

$$r_{lim} = \frac{\frac{(\frac{1}{2}r_E + 1)}{2}}{\sqrt{\left(\frac{\frac{1}{2}r_E + 1}{2}\right)^2 - 0.5}}$$

Equation 45

$$\varepsilon_{sc} = \left(\sqrt{2}\varepsilon'_{c0} - \frac{f'_c}{2E_0}\right) \times r_3$$

Equation 46

ε_{sc} determines the peak location of the shear springs with r_3 being a calibration parameter assumed equal to 1.2, E_0 is the elastic modulus and f'_c is the macroscopic compressive strength of the concrete in MPa, ε'_{c0} is the compressive strain of concrete pertaining to maximum macroscopic compressive strength, as suggested by Carreira and Chu [31] is evaluated from

$$\varepsilon'_{c0} = \frac{0.71 f'_c + 168}{10^5} \times r_2$$

Equation 47

In which r_2 is another parameter assumed equal to unity added to the original equation for the purpose of calibration.

also r_E is evaluated as

$$r_E = E_0\varepsilon_{sc}/f_c' \qquad \textit{Equation 48}$$

The function β, defined by Equation 49, adds additional calibration parameters to modify the behaviour of shear springs.

$$\beta = \frac{a_1 - a_2}{1 + e^{\frac{c(|\varepsilon_s| - \varepsilon_{sl})}{\varepsilon_{sl}}}} + a_2 \qquad \textit{Equation 49}$$

In equation above, ε_{sl} is defined as

$$\varepsilon_{sl} = c_c\varepsilon_{sc} + c_l\varepsilon_{s\,lim} \qquad \textit{Equation 50}$$

Where a_1, a_2, c, c_c and c_l are calibration parameters introduced by β and are given in the Table 1.

In Equation 43 α is a parabola function of normal stress (σ) of degree n for $\sigma < 0$ and a linear for $\sigma \geq 0$ as given in Equation 51, adding the effect of normal springs to the behaviour of shear springs. in Equation 51, v_c is the mesoscopic shear strength for $\sigma = 0$ and in this study, it is assumed to be evaluated from Equation 52. Rest of the parameters in Equation 51 can be evaluated from Equation 41 and Equation 53 - 55. The degree of the α, n, is assumed to be five ($n = 5$). Figure 21 depicts αv_c as a function of normal stress.

$$\begin{aligned} \alpha &= \sqrt[n]{a_p\sigma + 1)} && \sigma < 0 \\ \alpha &= (1 - \sigma/\sigma_t^c) && \sigma \geq 0 \end{aligned} \qquad \textit{Equation 51}$$

$$v_c = 0.83\sqrt{f_c'} \qquad \textit{Equation 52}$$

$$a_p = \frac{\left(1 - \frac{\sigma_{fail}}{a_f}\right)^n - 1}{\sigma_{fail}} \qquad \textit{Equation 53}$$

$$a_f = \frac{v_c f_c' \cos^2 60}{f_c' \sin 60 \cos 60 - v_c} \qquad \textit{Equation 54}$$

$$\sigma_{fail} = \frac{1}{2}f_c'(\cos(60) - 1) = -\frac{1}{2}f_c'(1 + \cos(2 \times 60)) \qquad \textit{Equation 55}$$

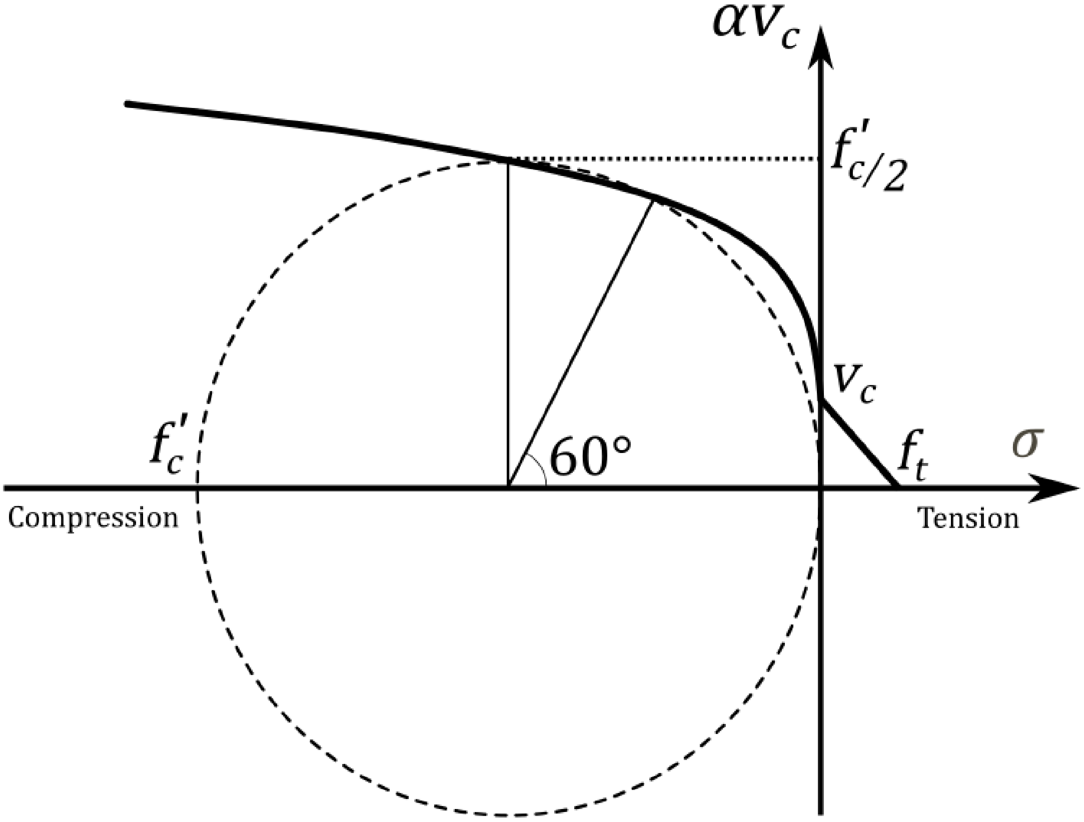

Figure 21. maximum shear stress as a function of normal stress

Once $\breve{G}_t$, reaches zero, with further increment of strain in shear springs, the negative value of tangent shear will create a softening effect in the model. With negative values of $\breve{G}_t$, elastic energy in normal springs starts to release. In this stage with further loading, some normal springs fall in tension and start to fail. To maintain a gradual softening a mitigation coefficient (c_m) is used for negative values of $\breve{G}_t$ (Table 1).

Table 1. Calibration parameter values

No.	Parameter	Condition	Value
1	r_1	-	0.3
2	r_2	-	1.0
3	r_3	-	1.2
4	c_m	$\breve{G}_t \geq 0$	1.0
		$\breve{G}_t < 0$	0.025
5	a_1	-	1.1
6	a_2	-	0.4
7	c	$\varepsilon_s < \varepsilon_{s\,lim}$	4.0
		$\varepsilon_s \geq \varepsilon_{s\,lim}$	1.0
8	c_c	$\varepsilon_s < \varepsilon_{s\,lim}$	0.4
		$\varepsilon_s \geq \varepsilon_{s\,lim}$	0.8
9	c_l	-	0.0
10	n	-	5

3.1.3. Deriving elasto-plastic stiffness matrix

The RBCS element features the Poisson effect by coupling the behaviour of the springs on one triangular rigid block. This is done by defining the stress strain relation matrix, [D], in a way that strain of one spring creates strains on other springs on other ridges of the rigid body which will lead to lateral expansion that represents Poisson effect. To obtain such a stress-strain relationship matrix, [D], it is easier to define the inversed stress-strain relationship matrix, $[\mathbf{D}]^{-1}$. $[\mathbf{D}]^{-1}$ is derived using this idea that by having the stresses on each ridge it is easy to obtain forces acting on the rigid body and use equilibrium of forces to evaluate a normal force for each ridge which gives a normal stress from which the Poisson strain for that ridge is calculated. More detailed explanation is provided in the literature introducing the RBCS element. For the nonlinear usage aimed in this research, inversed stress-strain relationship matrix is defined as:

$$[\boldsymbol{D_t}]^{-1} = \begin{bmatrix} \frac{1}{E_1^u} & \frac{-\nu}{E_0}\Pi_{12} & \frac{-\nu}{E_0}\Pi_{13} & \frac{-\nu}{E_0}\Gamma_{11} & \frac{-\nu}{E_0}\Gamma_{12} & \frac{-\nu}{E_0}\Gamma_{13} \\ \frac{-\nu}{E_0}\Pi_{21} & \frac{1}{E_2^u} & \frac{-\nu}{E_0}\Pi_{23} & \frac{-\nu}{E_0}\Gamma_{21} & \frac{-\nu}{E_0}\Gamma_{22} & \frac{-\nu}{E_0}\Gamma_{23} \\ \frac{-\nu}{E_0}\Pi_{31} & \frac{-\nu}{E_0}\Pi_{32} & \frac{1}{E_3^u} & \frac{-\nu}{E_0}\Gamma_{31} & \frac{-\nu}{E_0}\Gamma_{32} & \frac{-\nu}{E_0}\Gamma_{33} \\ 0 & 0 & 0 & \frac{1}{G_1^t} & 0 & 0 \\ 0 & 0 & 0 & 0 & \frac{1}{G_2^t} & 0 \\ 0 & 0 & 0 & 0 & 0 & \frac{1}{G_3^t} \end{bmatrix}$$

Equation 56

Where E_0 and E_i^u are the initial elastic modulus and degraded elastic modulus of normal spring on ridge i, and G_i^t is the tangent shear modulus of shear spring on ridge i; Π_{ij} and Γ_{ij} are parameters dependent to the geometry of element as introduced in definition of RBCS element. By inversing the $[\boldsymbol{D_t}]^{-1}$, the stress-strain relationship matrix, $[\boldsymbol{D_t}]$, will be evaluated. Elasto-plastic stiffness matrix is derived the same way as the elastic stiffness matrix is derived for RBCS element; except that the elasto-plastic stress strain relationship matrix ($[\boldsymbol{D_t}]$) is used instead of elastic stress strain relationship matrix ($[\boldsymbol{D}]$).

3.1.4. The convergence criteria

The convergence of a calculation step is evaluated from Equation 57:

$$convergence = \frac{\sum(f_{int}^2)}{1 + \sum(f_{ext}^2)}$$

Equation 57

in which f_{int} is the internal and f_{ext} is the external forces vector. The convergence criterion is set as 0.001.

3.1.5. Crack closure and stress transfer along the cracks

In the concrete the stress transfer along the discrete cracks can take place due to interlocking of crack faces. This behaviour is dependent to the crack surface configuration. Since throughout the process of stress transfer, the surface of crack goes though plastic deformations this behaviour is known to be ultimately complicated. The goal of this study is not focused on this phenomenon, but a simple algorithm is implemented in the code to simulate the crack closure and basic stress transfer to avoid problems like elements overlapping in the cracks. This algorithm takes advantage of a simple assumption implemented in related studies (e.g. [32,33]) according to which, the angle of resultant reaction on the contacting point will remain perpendicular to the initial surface of the crack before deformation. This assumption is implemented in the model by the algorithm to generate a force in the direction of normal springs when two rigid bodies on two sides of a failed surface overlap.

The generated resistance to overlapping in the cracks, will cause an effect like the phenomenon of shear dilation in concrete. However, since this effect is related to the crack roughness, the behaviour of model on crack surface it will be affected by the dimensions of the rigid bodies. If the model is discretized using a smaller discretization dimension, which results in smaller rigid bodies, the crack surface is expected to be affected. Also, as it is common in mesoscopic modelling, if the aggregates are modelled as a separate phase (e.g. [18,29]), they will also affect the crack form and consequently affect the stress transfer and shear dilation (Figure 22).

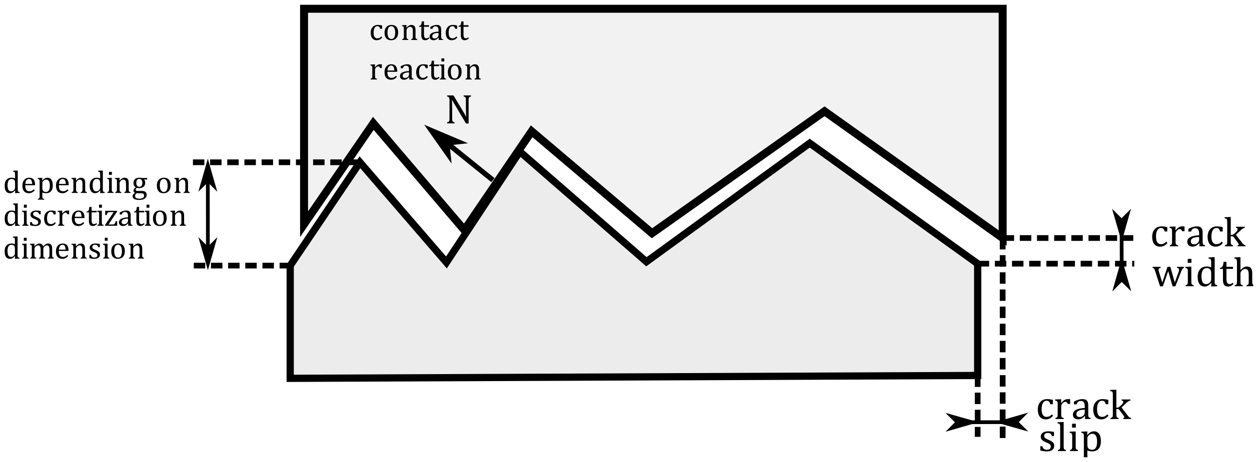

Figure 22. Effect of crack configuration on the stress transfer and shear dilation

Using multi-phase mesoscopic modelling limits the maximum discretization size to allow rigid bodies to be fine enough to model smaller aggregates which will demand excessive calculation costs. Instead of using multi-phase modelling, Eddy et al. used the rigid bodies as representative of coarse aggregates and assigned the dimension of 10mm to 20mm to rigid bodies, so they have correct crack configuration [34].

Bujadham and Maekawa estimated maximum crack roughness for normal strength concrete to be half of the maximum aggregate size and this value will decrease in higher strength concretes (possibly due to aggregate crashing) [33].

In this study it has been tried to maintain the dimension of approximately 5mm for the rigid bodies at the location of crack formation.

3.2. Analysis results

To investigate the behaviour of the model, several common tests performed on concrete-like materials are simulated. It is known that behaviour of RBSM is dependent on discretization dimension [18]. In the case of RBCS elements the material models were made in a way to avoid causing mesh-size dependency as much as possible. However, the crack development is directly affected by the discretization dimension (size of rigid bodies). Generally, with smaller mesh size, cracking has more path to propagate through and this will lead to a less ductile behaviour, in other words in smaller mesh the crack can propagate through weaker direction with less distortion. Another reason for weakness of small mesh could be that for smaller spring, same amount of strain means smaller deformation i.e. peak strain correspond to a smaller deformation and therefore more brittle behaviour. This is especially the case where local crack occurs in tension. Defining a tensile behaviour in which failure of springs is based on the crack mouth opening can be an alternative way to confront this issue. The current paper will not cover this topic any further, but this will be investigated in the future works. Simulations in this section were performed with discretization dimension of approximately 5mm. To reduce the calculation costs of some models, in the parts of the that are not of main interest (e.g. no failure is expected) gradual increment in discretization dimension is allowed.

The modelling, discretization and post processing is performed using pre/post-processing software, GMSH [26]. In all simulation the thickness of the model is assumed to be equal to unity (1mm). The mechanical properties assumed for the concrete materials used in the simulations are given in Table 2.

Table 2. Input mechanical properties of concrete for RBCS element

No.	Parameter	Notation	Value
1	Compressive strength	f_c'	36 [MPa]
2	Elastic modulus	E_0	30000 [MPa]
3	Poisson's ratio	ν	0.2
4	Focal strain	ε_{foc}	-1.24e-4

3.2.1. Uniaxial compression test

To examine the behaviour of the proposed element in compression, uniaxial compressive test simulations are performed. Dimensions of the modelled concrete specimen are assumed to be 100 by 200 millimetres. The boundary conditions for the first simulation is prescribed downward displacement of 0.8 mm applied gradually in 200 steps to the top boundary of the model and prescribed zero displacement in vertical direction for bottom boundary with horizontal zero displacement in horizontal direction applied to only one element to provide stability without creating any horizontal reaction force. Using this boundary conditions, the modelled specimen can be studied under condition of absolutely no confinement induced due to frictional force on loading surfaces. However, practically it is not possible to reduce the friction force to zero therefore a secondary model was created with the loading jaws simulated with elements bounded to elements of the specimen and prescribed displacement were applied to the elements of jaw and not directly to the specimen. Jaw elements are assumed to be elastic with mechanical properties of steel as given in Table 3.

Table 3. Input mechanical properties of steel elements

No.	Parameter	Notation	Value
1	Elastic modulus	E	200,000 [MPa]
2	Poisson's ratio	ν	0.3

The interface of the jaw and concrete is composed of four springs for each pair of elements (i.e. two shear springs and two normal springs) that are connected in series arrangement

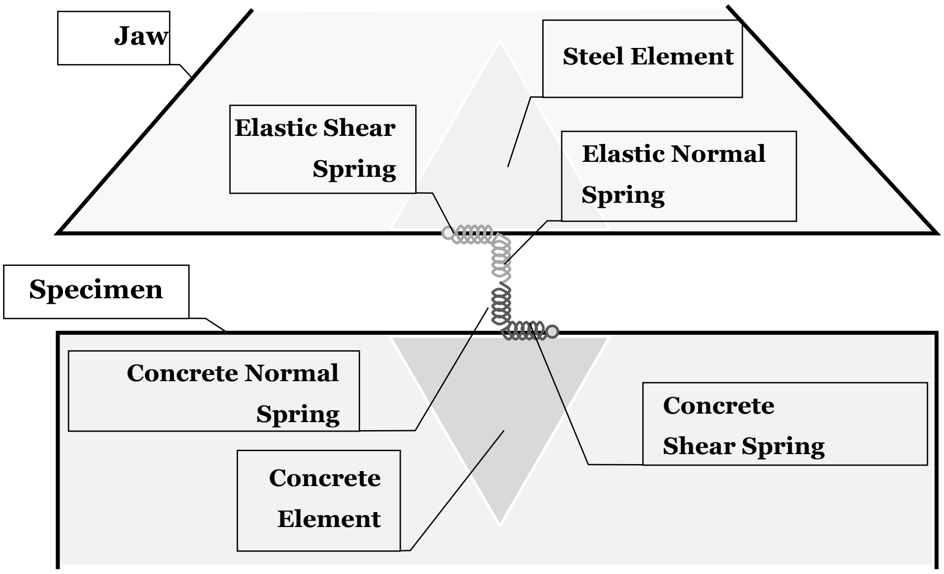

(

Figure 23). The normal springs will linearly transfer compression from jaw to the concrete and the shear springs will represent the induced confinement due to friction. The shear spring on the jaw side performs linearly with properties of steel on the other hand the shear spring on concrete side performs just like concrete springs. This set up will create an exaggerated effect induced to specimen from loading jaw which is the ultimate opposite condition of frictionless model.

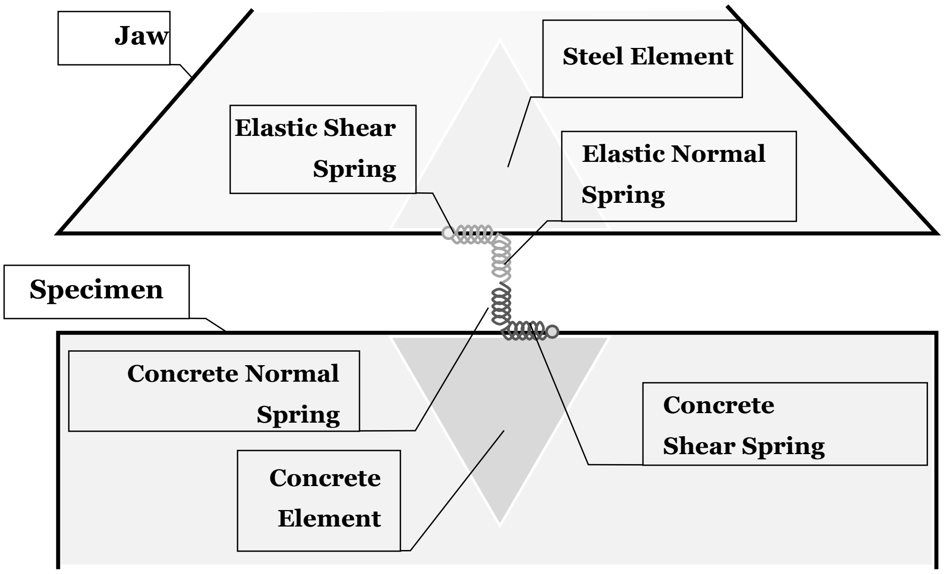

Figure 23. Interface of Jaw-Specimen in Model II (element size exaggerated for better demonstration)

Similar simulations are performed using RBSM element using a program originally developed in 2004 [18]. The rigid body dimensions for RBSM model is approximately 5mm and the material properties used for RBSM elements are given the Table 4.

Table 4. Input mechanical properties of concrete for RBSM element

No.	Parameter	Notation	Value
1	Tensile strength	f_t	3.52 [MPa]
2	Elastic modulus	E	30,000 [MPa]
3	Poisson's ratio	ν	0.2

For RBSM element, the value of the tensile strength (f_t) is evaluated based on 36MPa compressive strength of concrete using Kosaka's relationship (Equation 44) which is implemented into RBSM code. Based on this value a 36MPa compressive macroscopic strength is expected from RBSM model. In the models simulated using RBSM, the frictional restraint is implemented by preventing the top and bottom boundary of the specimen to move in horizontal direction, this will result in an intensive lateral confinement.

The visualized outcome of RBCS element analysis results of the frictionless compressive test (model I) is depicted in Figure 24 with deformation magnified 50 times for clarity. The peak axial stress happens approximately in step 95. It can be observed that from step 95 to 105 the small splitting cracks are gradually increasing until finally a diagonal crack merge with them and cause an accelerated lateral deformation. In step 110 the failure mode of the specimen can be observed.

In the case of intensive frictional restraint (model II), as it can be observed in Figure 25, the frictional force will restrain the loading faces of the concrete to expand laterally while the element tries to expand due to Poisson effect and the formation of cracks and with some distance from the loading boundaries lateral expansion can be observed. The variance between expansion of the specimen in the middle compared to the ends is clearly observed in step 117 which is approximately the peak axial force of the specimen. As the loading continues to the step 135 the splitting cracks form and propagate in axial direction causing additional the lateral expansion. Following that transversal shear cracks start to form connecting the splitting cracks they create excessive expansion of the specimen.

The axial force versus deformation induced to the specimen, obtained from model I and model II, beside the results obtained from RBSM elements, are depicted in Figure 27.

For a better comparison, expected response of concrete under uniaxial compression test, obtained from model code 1990 [24] and Carreira and Chu [31] are included as well. To evaluate the these models, the mechanical properties is taken same as the value given in Table 2 and the strain value corresponding to the peak stress for both models is obtained from Carreira and Chu [31] recommendation (Equation 47). The model obtained from the model code 1990 considers a rather brittle behaviour after peak on the other hand the second adopted model provided by Carreira and Chu [31] indicates a more ductile behaviour.

It can be observed that in the case of no frictional restrain (model I) the post peak stress of the specimen will drop rapidly and behaviour is closer to the recommendation of model code 1990, while in the case of exaggerated friction, interactions on the loading boundary will affect the failure pattern of the specimen making it more similar the Carreira and Chu’s model while increasing the peak compressive stress marginally. Since model II is an exaggerated case of lateral frictional restrain, it may be expected that a more realistic case, a less intense effect on the post-peak behaviour of the model should be observed similar to the normalized post-peak behaviour of the experiments of Vliet and Mier who performed compression test on concrete with different boundary friction reduction counter measures [35] depicted in .

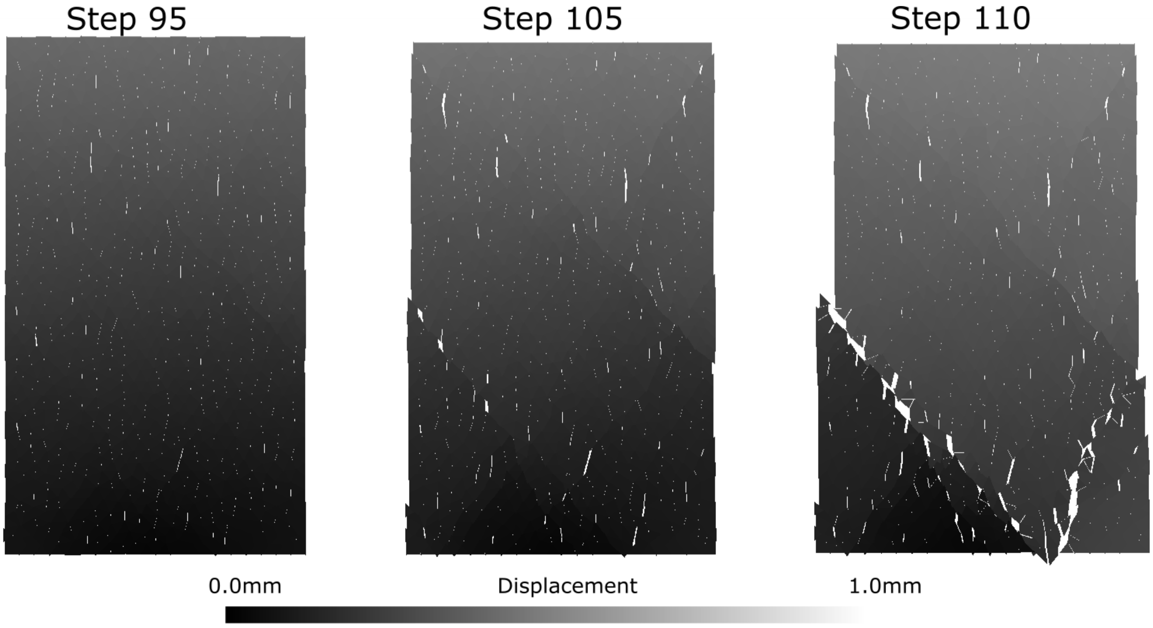

Figure 24. Uniaxial compression test without frictional restraint (Model I)

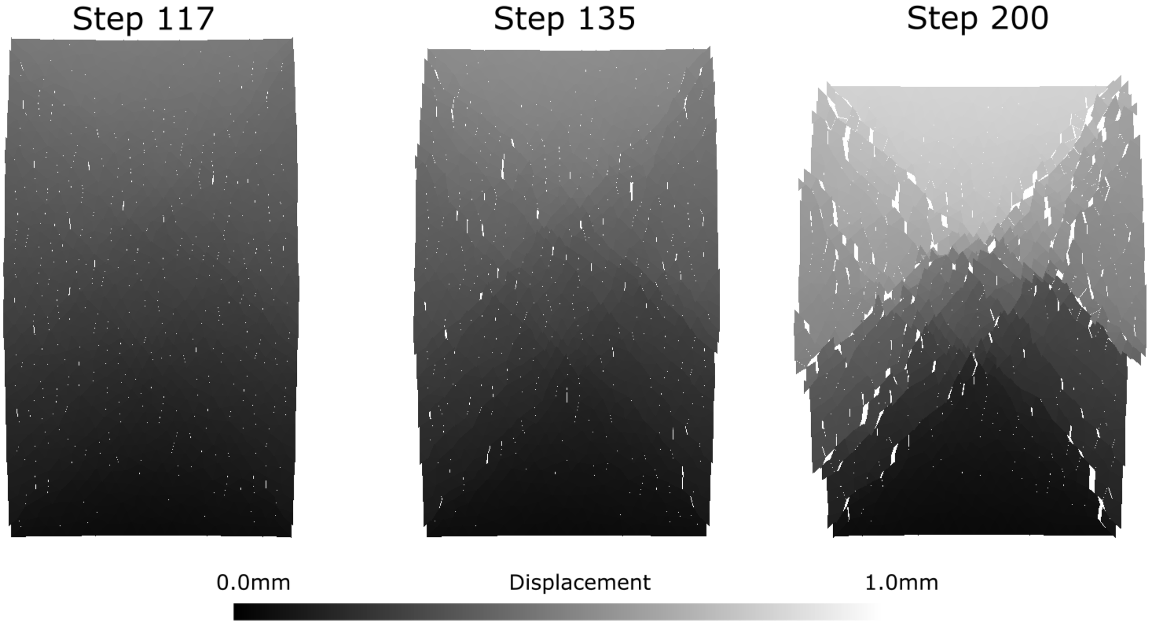

Figure 25. Uniaxial compression test under intense frictional restraint (displacements magnified 50 times)

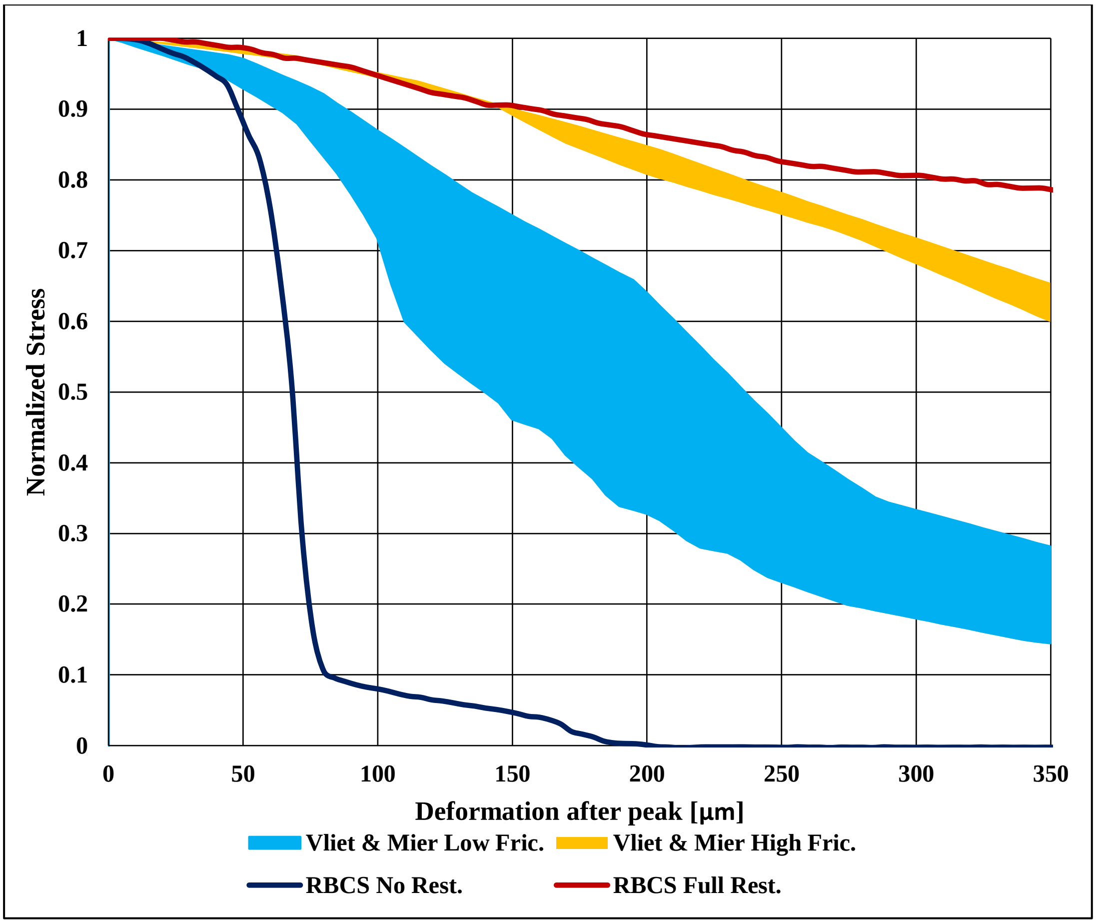

Figure 26. Effect of loading jaw on the post-peak compressive behaviour of concrete [35]

Compared to the stress-strain response of RBSM, the response of RBCS elements is more similar to the proposed models by Model code 1990 and Carrieira and Chu as it can be observed in Figure 27. In contrary to RBCS, RBSM showed a residual strength even in unconfined uniaxial compression. Displacement of elements for RBSM models with magnification factor of 10, are depicted in Figure 28.

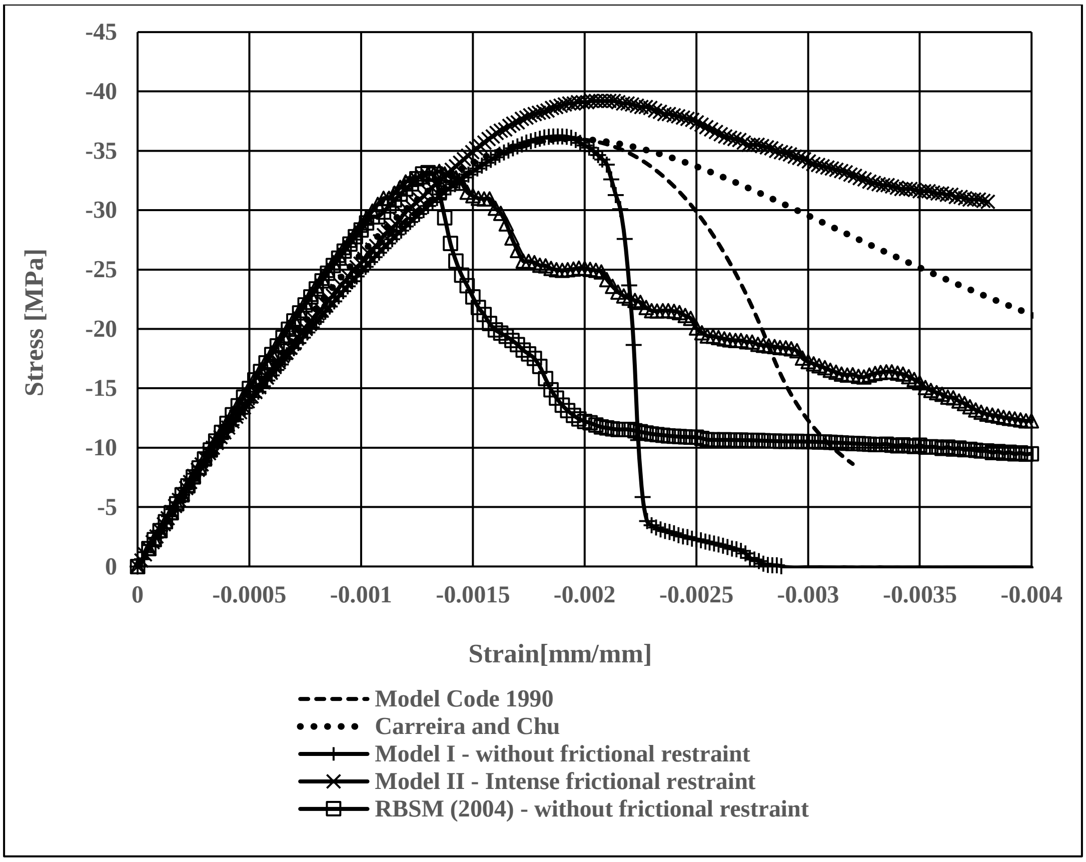

Figure 27. Uniaxial compression test simulation using RBCS and RBSM element (homogenous models)

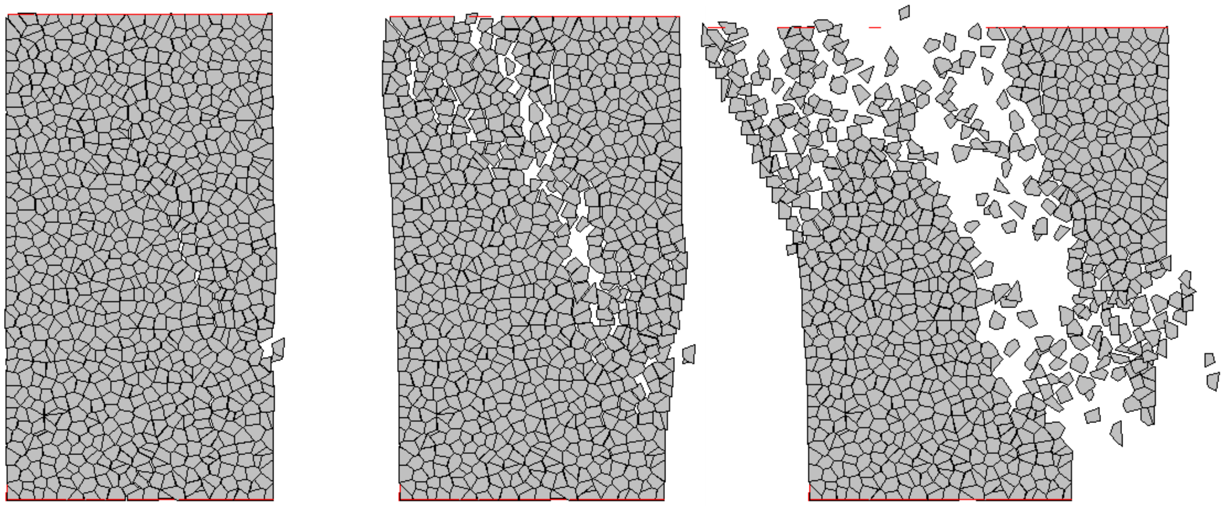

Step 52 Step 56 Step 72
Without restraint

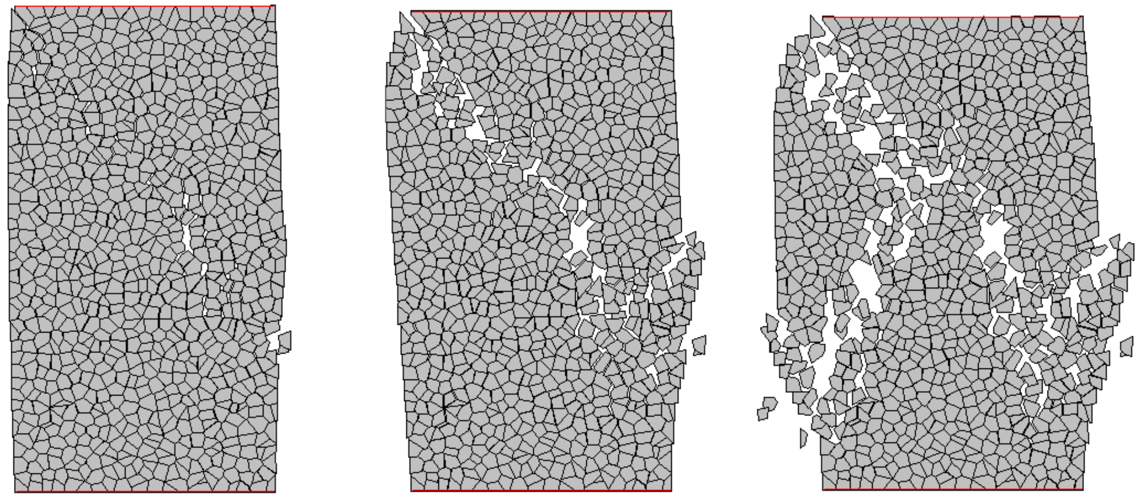

Step 54 Step 63 Step 72
Intesive restraint

Figure 28. Depiction of RBSM elements with and without restraint

3.2.2. Uniaxial tensile test

In second series of simulation, uniaxial tensile test is simulated using three models. Model I and model II are dog-bone shaped specimens and allow failure to happen the weakest section of a designated failure zone while model III is an hourglass shaped specimen coercing the failure in a specific section (Figure 29). Dimensions of dog-bone model II is based on experiments performed by Malarics and Muller [36,37] and dimensions of hourglass specimen are adopted from [38]. Model I, has same dimensions as model II, except that the length of failure zone is reduced from 200mm to 165mm.

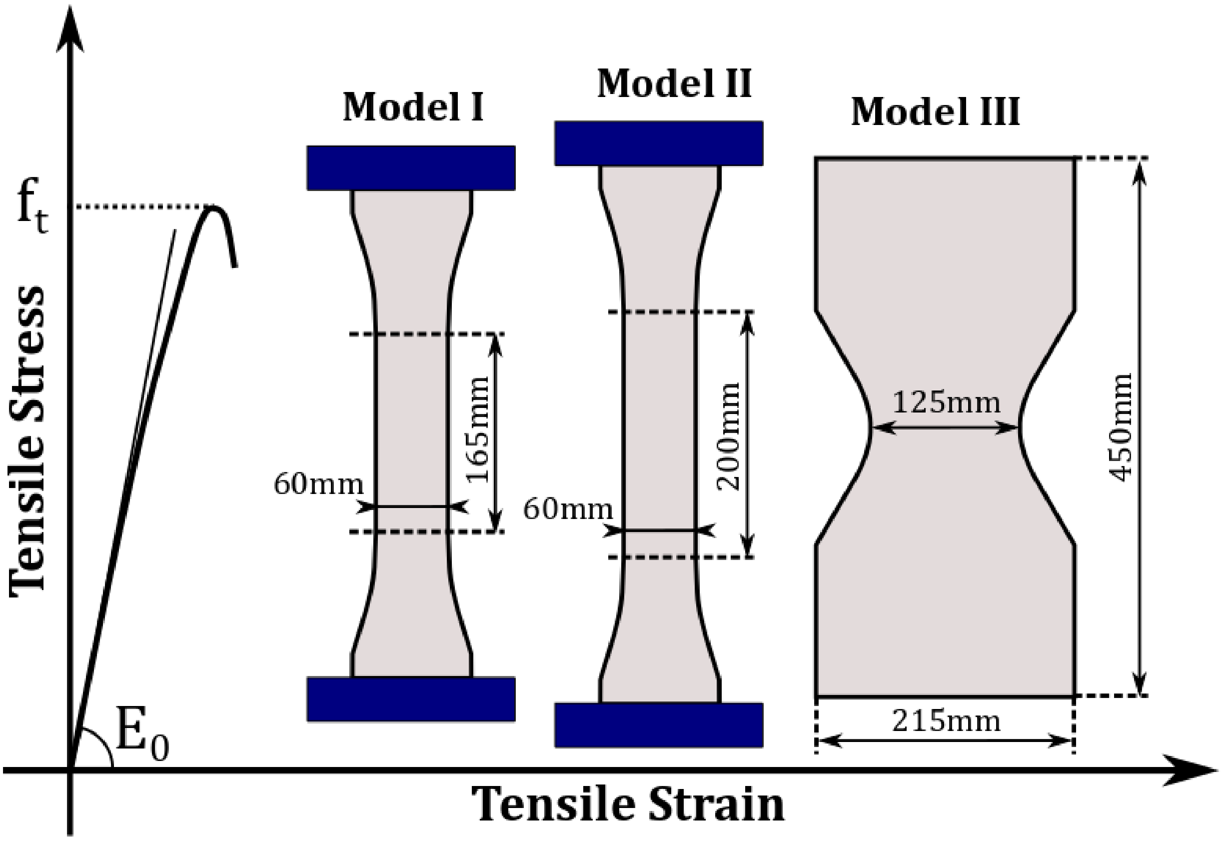

Figure 29. Uniaxial tensile test models

To reduce the calculation costs, the dimension of discretization will gradually increase outside of the failure zone, but it is maintained approximately 5mm in areas that failure is expected to happen to keep the results comparable with other tests simulations (Figure 30).

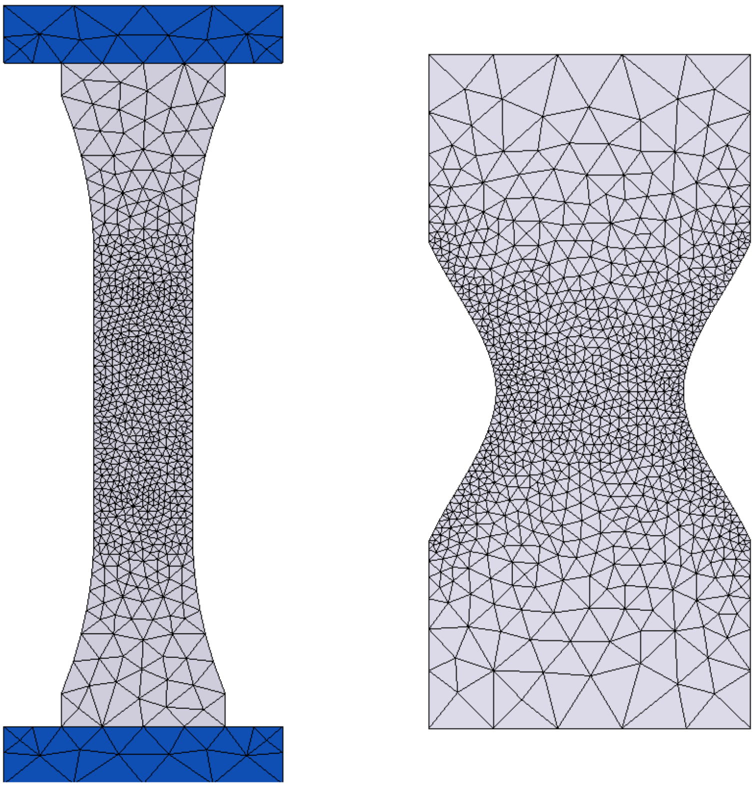

Figure 30. Varied discretization dimension of the dog-bone and hourglass specimens

For the dog-bone specimen the loading jaws were also modelled and an upward displacement of 0.08 is applied to the upper jaw in 200 steps while zero movement in vertical direction is applied to the lower jaw. For the hourglass, the original test setup is different and includes embedded bolts inside the specimen [38]. In this case the test conditions are simplified and same boundary conditions is applied directly to the concrete elements on top boundary of the model. To maintain stability in horizontal direction, movement of one element is horizontally constrained.

The depicted force displacement response of the models in Figure 31a confirms that model I and II have a wider hardening phase compared to model III. For model I and model II many sections go through hardening since the failure can occur in a wide region and it is very likely that several sections have a close energy levels for failure. On the other hand, for the model III the possibility for crack formation is limited to the narrow neck of hourglass shape. However, in a real case scenario for dog-bone, a crack may initiate at a flawed point in the failure zone causing the specimen failure more abruptly. RBSM simulation takes advantage of random distribution of strength while in RBCS simulations such approach is avoided, yet the arrangement of the elements limits possible failure patterns. Model II has the longest failure zone and therefore it is more likely that a crack formation with smaller energy occurs, so it is reasonable to expect the smallest tensile strength from this specimen while for model III a higher tensile strength may be observed. Evaluated tensile strengths, f_t, from the models, presented in Table 5, confirms this.

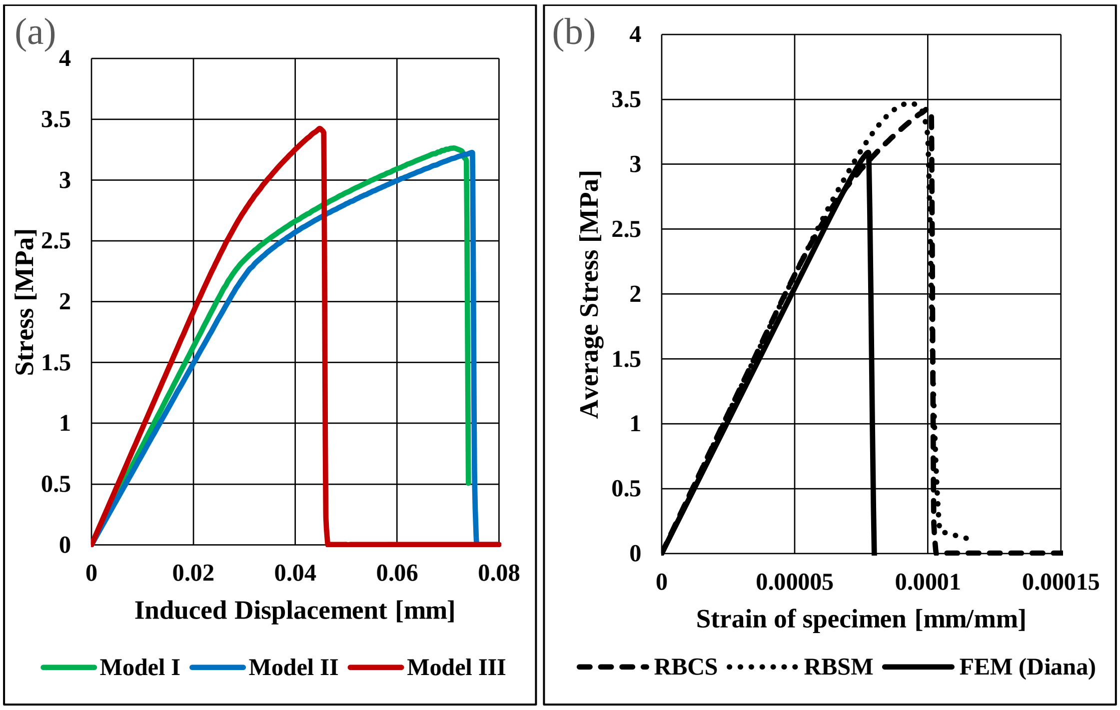

Figure 31. a) Force-displacement response of the uniaxial tensile tests b) Model III simulated in RBCS, RBSM and FEM

A comparison between behaviour of RBCS and RBSM element along with an FEM model performed using DIANA[39] with linear tensile-softening relationship assigned to concrete material is given Figure 31b. It can be observed that the behaviour of the models is similar.

Table 5. Obtained tensile strength from uniaxial tensile test

No.	Simulation	Peak force [N]	Cross section [mm^2]	f_t [N/mm^2]
1	Model I	195.8	60 x 1	3.26
2	Model II	193.4	60 x 1	3.22
3	Model II	428	125 x 1	3.42

Displacement distribution before and after crack formation is depicted in Figure 32. It can be observed that in all three models the tensile crack appeared abruptly. This happens due to reverting of elastic deformation as one section undergoes softening stage. This will induce more deformation in the failing section and consequently further softening which leads to sudden failure of specimen. Release of elastic energy was also reported in direct tensile test experiments by Amin et al. [38].

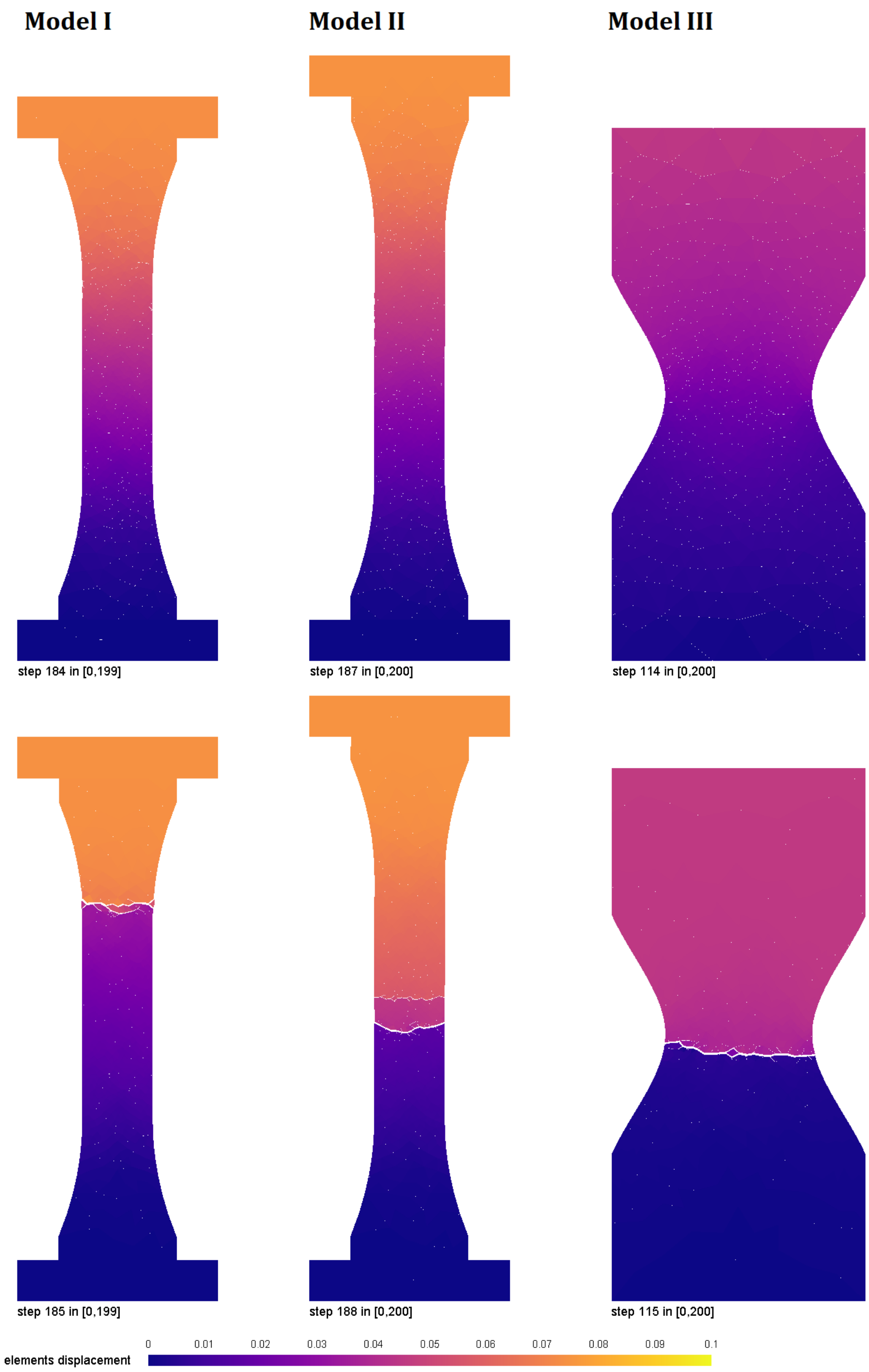

Figure 32. Displacement pattern of model before and after tensile cracking

3.2.3. Splitting tensile test

For simulation of splitting tensile test, researches performed by Malarics and Muller [36,37] was targeted to make it possible to compare the results obtained from Model II of direct tensile test. The mentioned series of splitting tensile tests were performed on cylindrical specimens according to the DIN EN 12390-6:2001 standard with exception of excluding usage of hardboard packing as bearing strips in the experiment apparatus to avoid problems they encountered with testing high strength concrete specimens. Implementation of such bearing interlayers along the length of the specimen however is required by various standards while the required width varies between standards, for instance BS EN 12390-6:2000 recommends a width of 10mm while DIN EN 12390-6:2010 recommends 15mm and yet the ASTM standard recommends width of 25mm for the bearing strips. The contact width and distribution of the load on the boundary condition is determined by the bearing strips. By excluding them it may be expected that the contact surface between the bearings and the specimen will be reduced and a more concentrated load to be applied at least at the early stages of loading. In theory, if ratio of loading width to specimen diameter in splitting test is small, it will have a small effect on the obtained tensile strength in the centre of specimen, however numerical studies of splitting tensile test shows a considerable difference between load bearing strip width of 10mm and 20mm for diameter of 150mm[36]. Performing numerical simulations, Malarics and Muller observed validating results for their experiment by modelling steel bearing with width of 10mm for specimens with diameter of 150mm [37].

Given this introduction, the cylindrical specimen was modelled and discretized to approximately 5mm elements (Figure 33). To simulate the loading condition a bearing width of 10mm was considered and two elements at top were prescribed by the downward displacement of 0.08mm in 200 steps while at the bottom two elements were prescribed with zero displacement in vertical direction. Finally, one element was prescribed zero horizontal movement to provide global stability of the model.

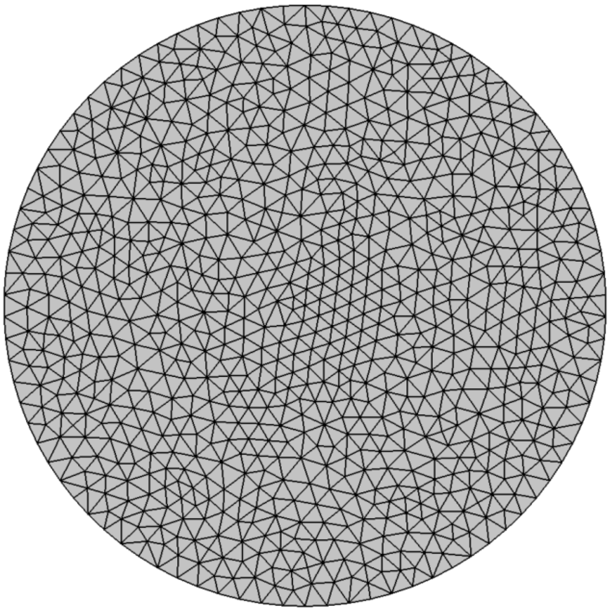

Figure 33. Discretization of the model

The obtained displacement response of the model at peak and following steps are depicted in Figure 34 (displacement magnified 50 times). It can be observed that cracks initially form beneath the loading area then combine and propagate through the height of the specimen. This behaviour was also reported by Malarics and Muller in normal strength concrete specimens that indicates formation of cracks that merge and propagate toward centre and formation of wedge ruptures below the bearings (Figure 35).

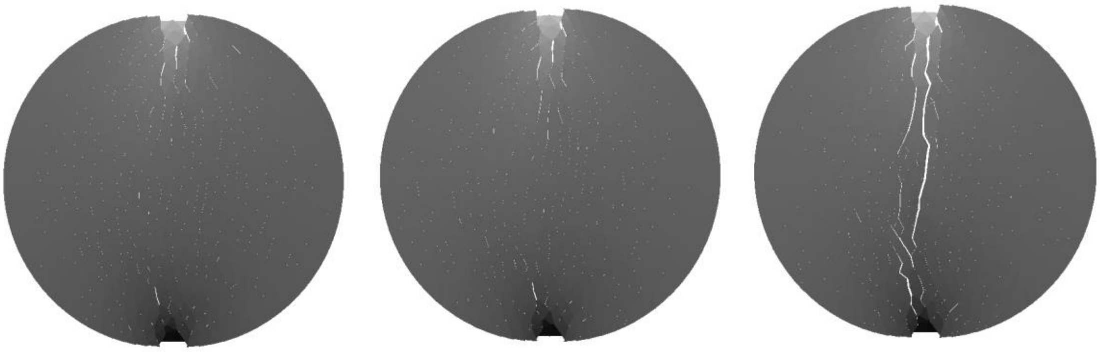

Figure 34. Visualization of split test simulation results. From left to right, Steps 43 (peak load) to 45 (vertical crack observation)

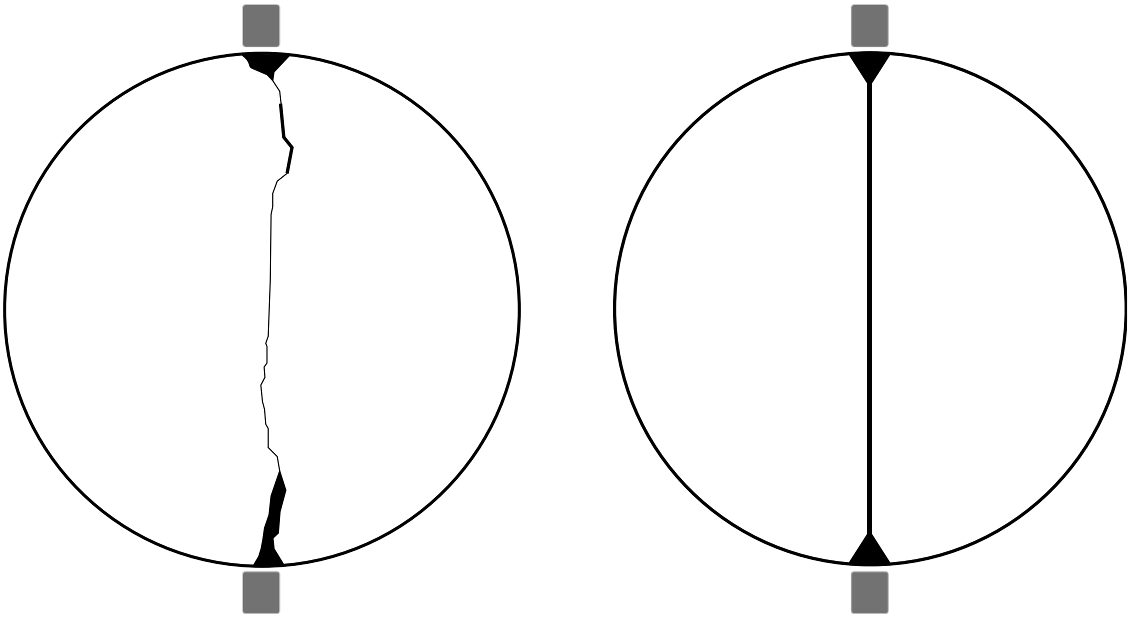

Figure 35. A sample of observed cracking (left) and fracture mechanism pattern (right) in the split tensile test of normal strength concrete [36]

The obtained split tensile strength from simulation of split test, f_{ts}, is equal to 3.41MPa which is very close to the values obtained from direct tensile test simulations (Table 5).

3.2.4. Behaviour of the element in non-homogenous (multi-phase) mesoscopic modelling

In mesoscopic modelling of concrete like material, to account for non-homogeneity of concrete, it is possible to assume the model comprises multiple phases. These phases include (not necessarily limited to) **mortar matrix** phase and **course aggregates** phase. Such concept is used in some research papers that utilize RBSM for simulation of concrete while some other studies assume one phase for concrete. For the case of simulation in previous chapters, the concrete comprised only one phase. In this section multi-phase concept is implemented to investigate the behaviour of RBCS elements further.

The implemented aggregate-mortar interface (or interfacial transition zone, ITZ) uses same concept as the one used in jaw-specimen interface shown in

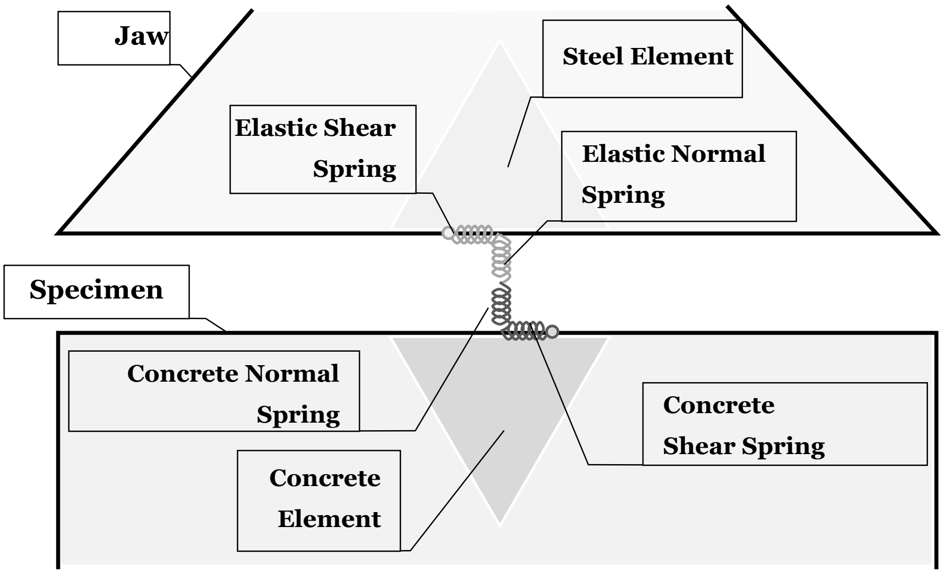

Figure 23 except that aggregate spring replace springs of jaw.

Material model of the aggregates is same as the behaviour of the mortar with different mechanical properties which is assumed for aggregates. Input mechanical properties of mortar matrix and aggregates used in multi-phase simulations are given in Table 6 unless stated otherwise.

Table 6. General mechanical properties used in multi-phased simulation

No.	Phase	Parameter	Value
1	Phase I - mortar matrix	Compressive strength	36 [MPa]
		Elastic modulus	28200 [MPa]
		Poisson's ratio	0.2
		Focal strain	-1.24e-4
2	Phase II - aggregates	Compressive strength	80 [MPa]
		Elastic modulus	40000 [MPa]
		Poisson's ratio	0.25
		Focal strain	-1.24e-4

Aggregate distribution is performed randomly and automatically based on Fuller-Thompson grading curve given in Equation 58.

$$P = \left(\frac{d}{D}\right)^n \qquad \textit{Equation 58}$$

In which P is passed percentage for sieve size of d and D is the maximum aggregate size in the specimen. The parameter n, determines amount of course aggregates and is usually chosen between 0.1 to 0.67 based on the usage demands (e.g. workability). In this section, parameter n is selected equal to 0.35 and maximum aggregate size, D, is 22.6mm (figure).

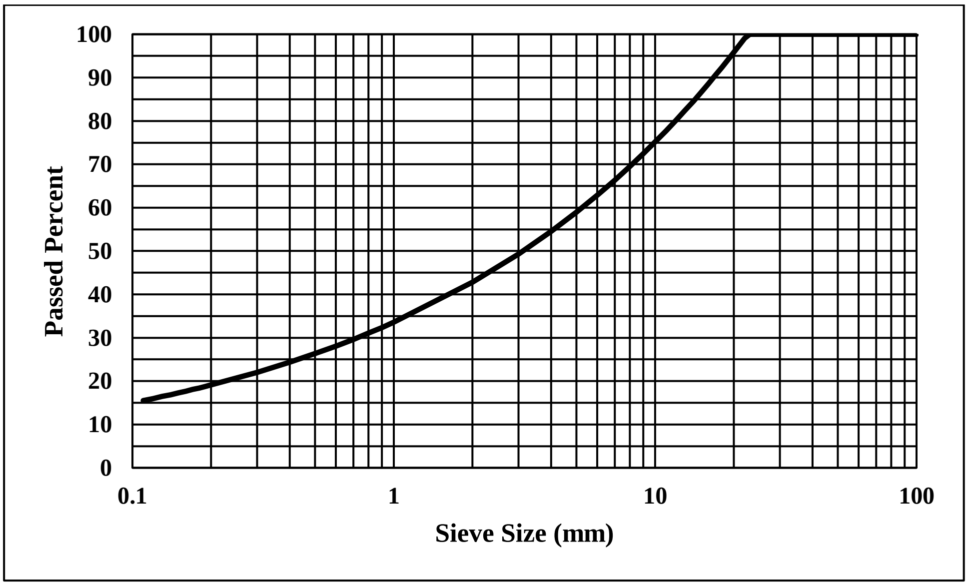

Figure 36. Fuller-Thompson grading curve (n=0.35, D=22.6)

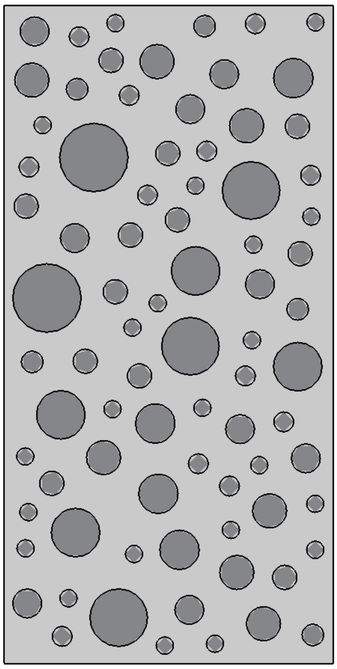

Figure 37. An instance of random aggregate distribution inside the model

The uniaxial compression test is performed with and without frictional restraint using nonhomogeneous model. The visualized failure pattern for both cases is presented in Figure 38.

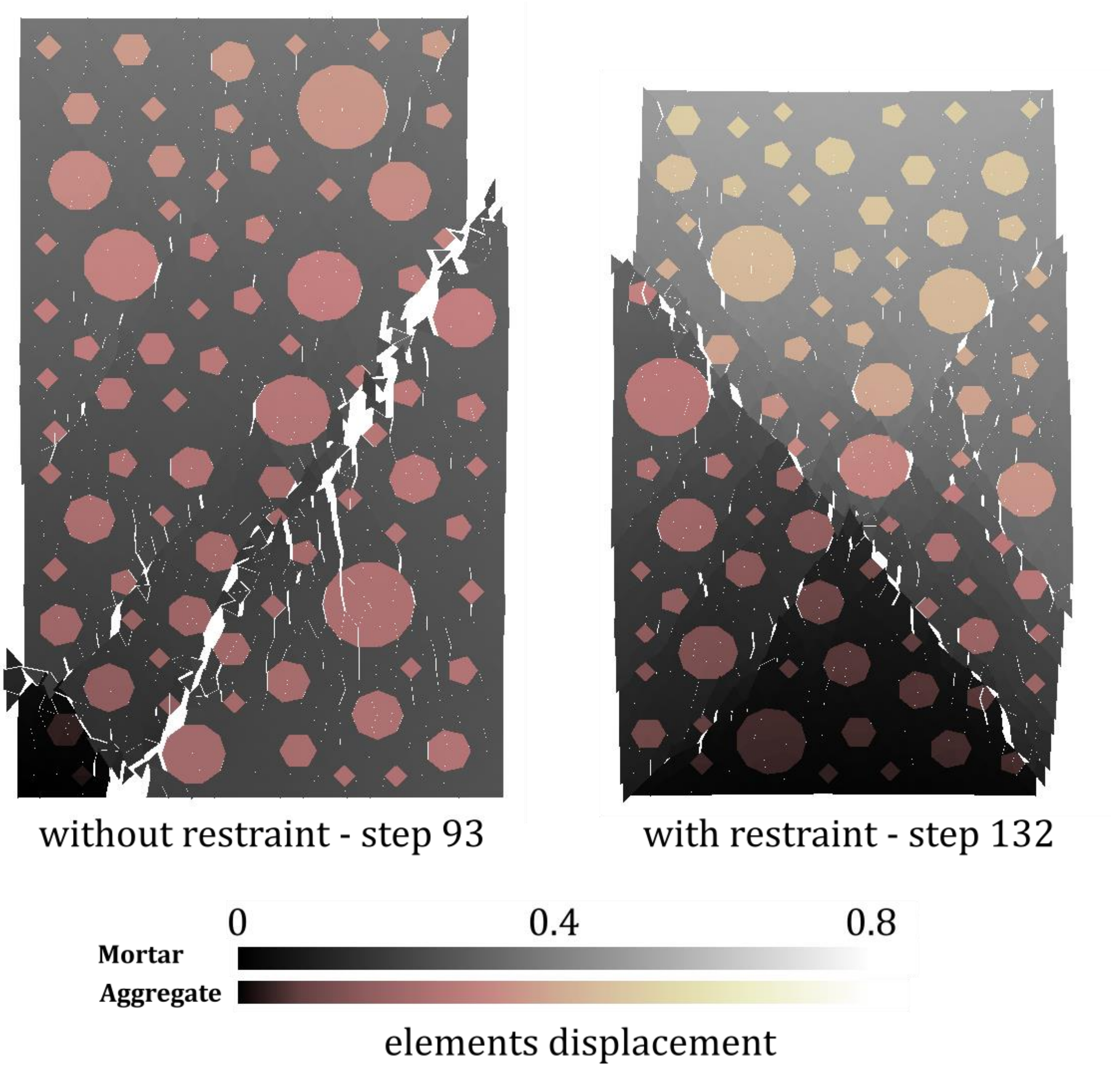

without restraint - step 93

with restraint - step 132

Figure 38. Failure pattern of non-homogenous models with (right) and without (left) frictional restraint on loading boundaries (displacements in mm)

The stress-strain response of simulations with and without restraint is presented in Figure 39. It can be observed that the non-homogenous model behaves more brittle compared to homogenous models.

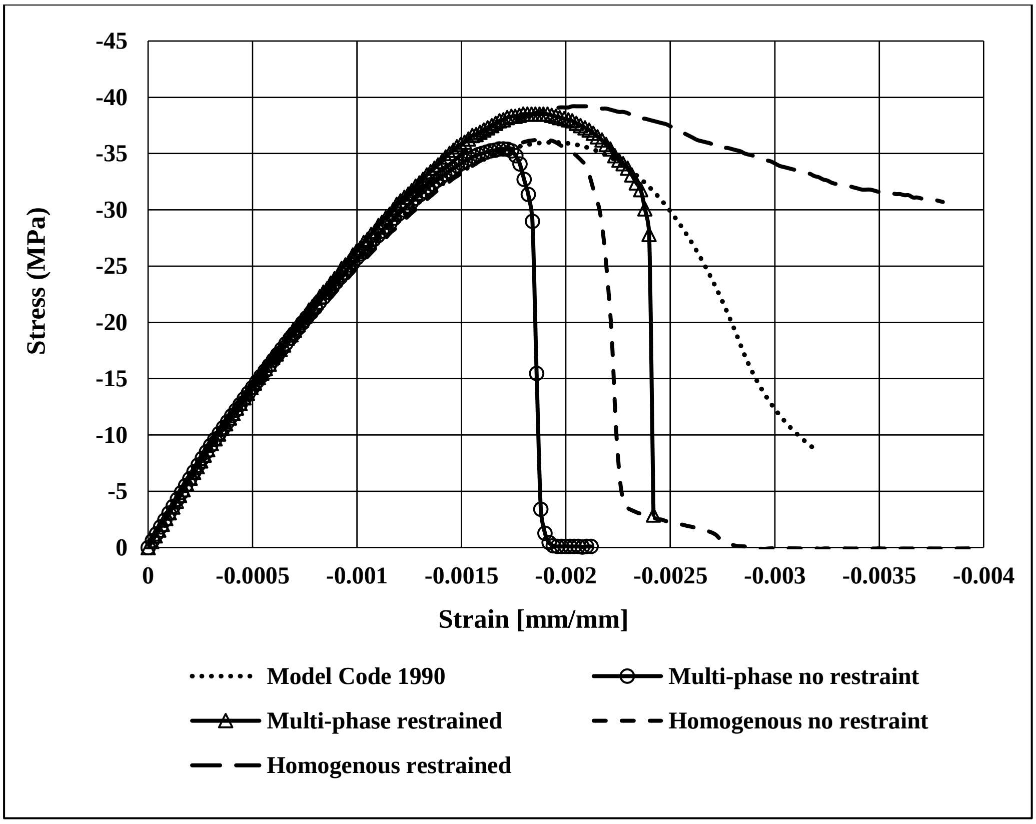

Figure 39. Stress-strain response of non-homogenous models

The Poisson's ratio difference between aggregate and mortar phase will affect the failure pattern. This effect is investigated by once assigning the Poisson's ratio of 0.2 to both mortar and aggregate and then Poisson's ratio of 0.17 to mortar and 0.25 to aggregates respectively and performing the simulating uniaxial compression test without considering frictional restraint. The stress-strain response in these simulations was not dramatically changed but as shown in Figure 40 the failure pattern will be affected.

Generally, for the case of no frictional restraint more splitting cracks can be expected. Compared to the homogenous model, splitting cracks are more distinguishable in analysis outcome of non-homogenous models. Some of these splitting cracks can even penetrate aggregates. As it can be observed in Figure 38 and Figure 40, in all failure cases, shear crack also appeared.

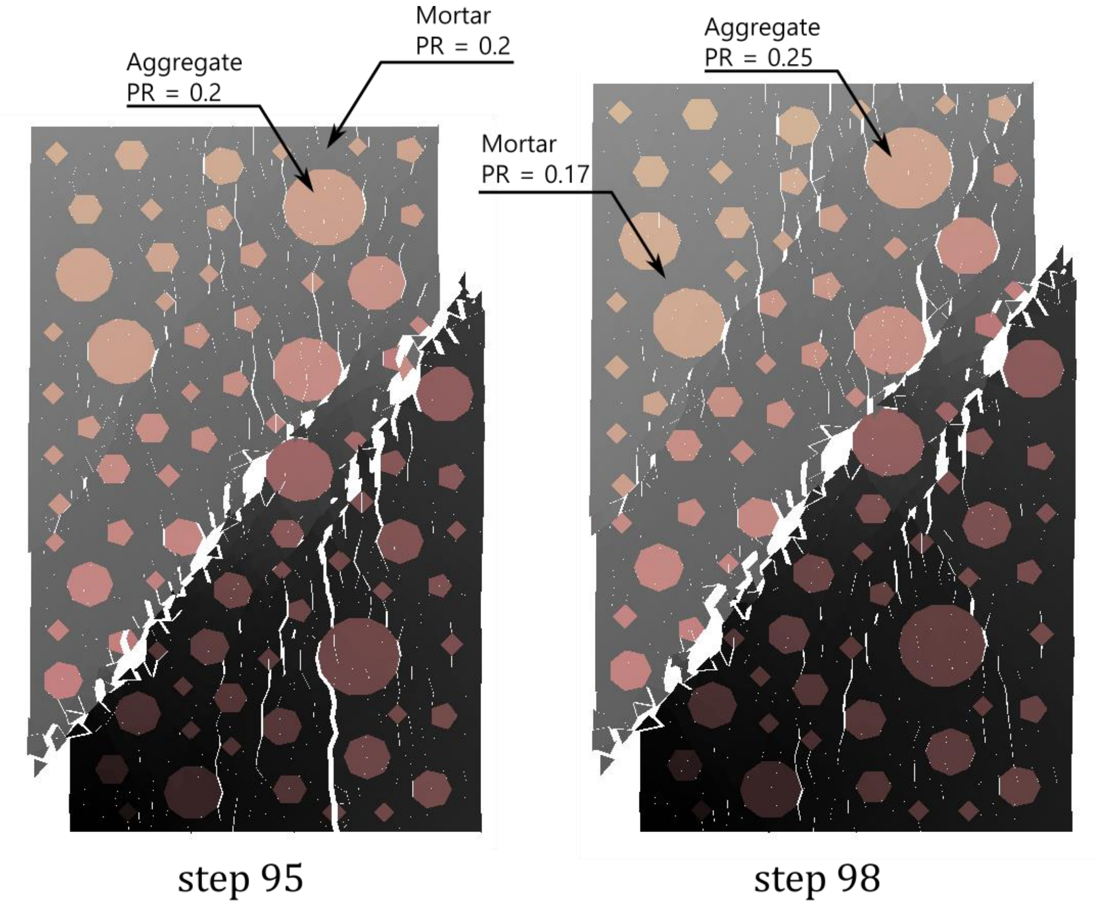

Figure 40. Effect of Poisson's ratio on failure pattern of the model

3.3. Discussion

According to the provided results, simulation of uniaxial compression test could provide the split cracking and diagonal shear cracking in concrete like materials while the final failure of specimen was due to shear cracklings. Splitting failure mode (in which the splitting cracks coalesce to form a columnar fragmentation) was not observed but in some laterally unrestrained cases, especially for the models with aggregate distribution, splitting failure can be seen along with shear cracks. Since splitting fracture or combination of splitting and shear fracture is a common failure mode of compressive tests (especially in cases with appropriate aggregate distribution and small frictional restraint), it might be possible to observe such failure modes with dense coarse aggregates phase however this may cause problems with meshing (discretization) of the model.

Studying the effect of confinement due to frictional restrain on loading faces showed RBCS element can capture such effect. The estimated compressive strength of 36 MPa was obtained in the case of no lateral confinement and in the case of excessive frictional restrain the compressive strength will exceed that value by 8.89%.

The tensile strength of the material was investigated using dog-bone model revealed the tensile strength of 3.22MPa, however when the failure section was limited using an hourglass shaped model it increased to 3.42MPa. Using Model Code 2010 to obtain the tensile strength of the 36MPa concrete (i.e. the tensile strength of 3.27MPa) and accepting the 3.22Mpa as the macroscopic tensile strength of the model, a variation of 1.56% will be evaluated for tensile strength accuracy.

By simulating the split tensile test, it was observed that the model could appropriately capture the failure mode and cracking of the specimen. To convert the direct tensile strength and splitting tensile strength the following equation can be used:

$$f_t = \alpha_{sp} f_{ts} \qquad \textit{Equation 59}$$

In which α_{sp} is conversion factor. Even with commendation of some older codes and researches regarding α_{sp} being smaller than unity [40], some recent studies suggest that α_{sp} is usually greater than 1.0; The Model Code 2010 [25] allows α_{sp} to be taken equal to 1.0 in that case the simulated split test slightly overestimates the tensile strength (5.90%). However, since the failure in the split test happens in one section it worth mentioning that this failure may be more similar to the failure of hourglass specimen. In that case the obtained tensile strength is almost same as hourglass specimen. Malarics and Muller proposed a set of relationships to evaluate α_{sp} based on specimen specifications[37]. According to their recommendation for 150mm by 300mm cylindrical specimen with gravel aggregates with compressive strength of 36MPa, α_{sp} can be evaluated as 1.17. In that case the tensile strength obtained from splitting test is 1.17×3.41=3.99MPa and the direct tensile strength is overestimated 23.9%. Despite the mentioned method of evaluating conversion factor, as already mentioned, there are some other observations and standards (e.g. [4,5]) that suggest the splitting tensile strength of concrete is generally greater than direct tensile strength and smaller than flexural tensile strength (i.e. $\alpha_{sp} < 1$).

3.4. Bottom line

In this chapter the developed discrete element, described in Chapter 2, was utilized for simulation of nonlinear behaviour of the concrete material. The improved material models include introduction of a novel behaviour for the shear contact springs which provides a more realistic behaviour to improve the behaviour of the model in uniaxial compression. The new element and assigned material models are also investigated in the cases of direct tension and splitting tension to assure that the model can simulate concrete in various conditions properly and not only in the case of compression.

The case of tensile simulation produced interesting results regarding the effect of the shape of the specimen on outcome of the test. This effect was commonly ignored by the researchers who have investigated the relationship between splitting and direct tensile tests. According to these results if the specimen provides a region for failure, such as the case of a dog-bone coupon specimen, a smaller tensile strength is obtained compared to the cases such as hourglass or splitting specimens.

A case of random multi-phase simulation of concrete specimen was also investigated according to whose results showed that introduction of the aggregate to the model defined in this chapter lead to more brittle behaviour and formation of more visible splitting cracks.

Chapter 4

Application of RBCS into simulation of SFRC

Conventionally in various structural applications the tensile weakness and brittleness of concrete is addressed by additional of reinforcement into the concrete however using the composite concrete material like Fibre Reinforced Concrete (FRC), which have better mechanical properties, in challenging structural designs is drawing more attention recently. Steel Fibre Reinforced Concrete (SFRC) is a commonly used type of FRC. Using steel fibre in concrete mixture was proposed in 19th and early 20th centuries by researchers including Bernard, Nekrasov and Porter [41,42]. Since simulation of composite concrete material using numerical methods based on continuum mechanics can be very complex, developing an effective simulation tool for such materials can contribute to related studies. Application of discrete models for simulation of concrete has been useful in various studies performed on concrete. In this chapter the developed discrete element, RBCS, is extended to be applied to fibrous concrete. Some modifications to material models were mandatory as will be described here.

4.1. Assumptions

4.1.1. Homogeneity of the fibre distribution

The basic idea of to derive the mesoscopic material model for the contribution of the steel fibres used in this study is that the fibres are equally distributed into specimen and they contribute equally in all locations and directions. A similar assumption is used by other researchers even for Steel Reinforced Concrete (RC) (e.g. [43]) and this assumption is more realistic for the case of fibre reinforced concrete.

4.1.2. The fibres are rounded-straight

The method used in this study can be extended to other types of fibres but for this study it is assumed that the fibre type is rounded – straight and fibre – matrix interaction is physiochemical and not mechanical. In other words, the fibre shape is not modified to create additional anchorage.

4.1.3. The pre-cracking contribution of fibre content

It is assumed that the contribution of the fibre to the resisting stresses is negligible when the matrix is intact and therefore fibre contribution (which is due to bridging) comes with a delay when the matrix is damaged (Figure 41a). In other words, the first cracking strength is affected by matrix strength rather than the effect of fibre content [38,44].

4.1.4. Fibre bridging action

- The contribution of fibre is described with three key points (Figure 41b)
- The key point denoted by s1 is assumed to happen simultaneously with matrix failure
- The effective length of fibre is assumed to be ¼ times fibre's nominal length
- A one-sided matrix spallation is assumed during the pull-out action

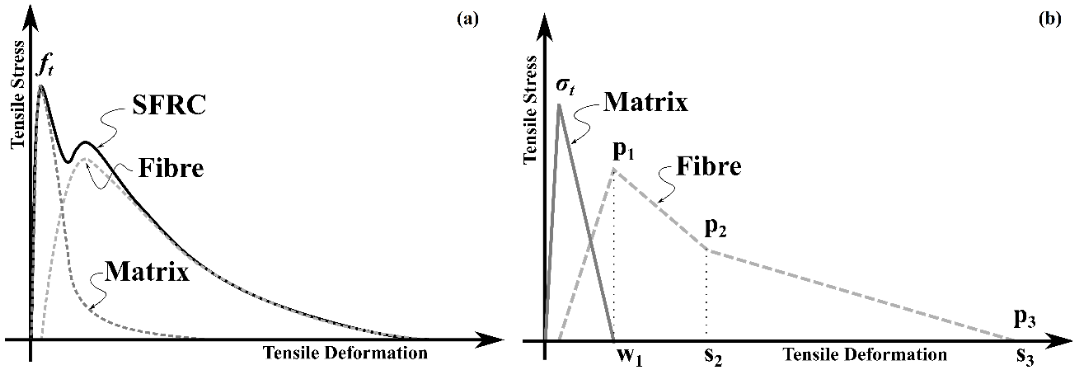

Figure 41. a) assumed tensile stress contribution model for matrix and fibre in SFRC b) the simplified assumed multi-linear behaviour for fibre and matrix

4.2. Modifications made to normal and shear springs and material models

The modifications to normal and shear springs are done to improve the behaviour and to provide a simpler model.

The tensile failure of the normal springs is redefined in terms of specific deformation which represents crack width instead of a specific tensile strain. Both concepts are used in simulating concrete elements namely the concept of failure strain is used in simulating RC members by Allam et al. [45,46] but in the case of discrete models it is common that the failure of tensile springs will be judged based on the deformation of the springs rather than their strain [18]. The designated failure deformation of normal spring is equal to 0.5×w_1 with w_1 being the ultimate crack width and the multiplier "0.5" added assuming two springs between each pair of elements are deformed equally. The value of w_1 is assumed constant and equal to 0.05mm. The maximum allowed stress in normal springs is denoted by σ_t is evaluated form the following equation:

$$\sigma_t = (0.1f_c')^{2/3} \qquad \text{Equation 60}$$

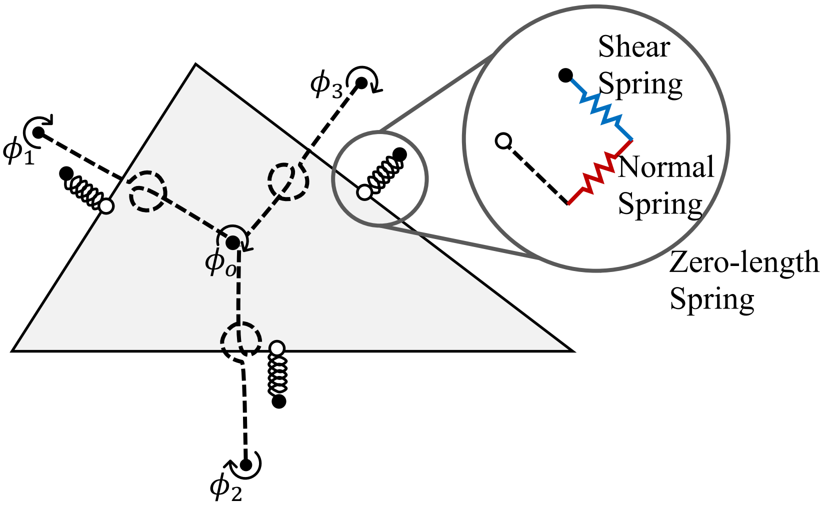

Figure 42. RBCS element rigid body, normal, shear and rotational springs

The tangent shear modulus, $\breve{G}_t$ is evaluated from a simplified Equation 61.

$$\breve{G}_t = -c_m \frac{(r_E-2)\left(\frac{\varepsilon_s}{\varepsilon_{sc}}\right)^2+2\left(\frac{\varepsilon_s}{\varepsilon_{sc}}\right)-r_E}{\varepsilon_{sc}\left((r_E-2)\left(\frac{\varepsilon_s}{\varepsilon_{sc}}\right)+1\right)^2} v_a \qquad \varepsilon_s < \varepsilon_{s\,lim} \qquad \textit{Equation 61}$$

in which, ε_{sc} is evaluated from a new equation according to the fibre content as:

$$\varepsilon_{sc} = 0.0023 + 0.0016 \times V.R.I. \qquad \textit{Equation 62}$$

in which V.R.I stands for Volumetric Reinforcement Index defined as volume fraction of the fibre times aspect ratio of the fibre.

In Equation 61, like Equation 43, the value of ε_s is limited to limit strain ($\varepsilon_{s\,lim}$) redefined as

$$\varepsilon_{s\,lim} = \varepsilon_{sc} \times r_{lim} \qquad \textit{Equation 63}$$

with r_{lim} and r_E redefined as:

$$r_{lim} = \frac{\frac{(\frac{1}{2}r_E + 1)}{2}}{\sqrt{\left(\frac{\frac{1}{2}r_E + 1}{2}\right)^2 - 0.5}}, r_E = 3.5 \times E_0 \varepsilon_{sc}/f_c' \qquad \textit{Equation 64}$$

For $\varepsilon_s \geq \varepsilon_{s\,lim}$, $\breve{G}_t$ is assumed to be constant and equal to one-fourth of the Gt evaluated at $\varepsilon_s = \varepsilon_{s\,lim}$ to slow down the final softening stage.

In Equation 64, v_a is replaced with αv_c in Equation 43 and β is omitted. In the case of tensile normal stress ($\sigma > 0$), v_a is reduced from v_c to zero as the yielding tensile stress is reduced from initial σ_t to zero. This behaviour will improve the stability of the model. In compression α is obtained similarly to what was defined in Equation 51. The calibrated parameters are for the modified element are summarized in Table 7. It is worth mentioning that the parameters are reduced since β function is removed and constant r_2 and r_3 are not used in the new definitions. Figure 43 schematically depicts $\breve{G}_t$ as a function of ε_s for a constant value of v_a.

Table 7. Calibration parameter values for new shear model

No.	Parameter	Condition	Value
1	r_1	-	0.5
2	c_m	$\breve{G}_t \geq 0$	1.0
		$\breve{G}_t < 0$	0.05
3	n	-	5

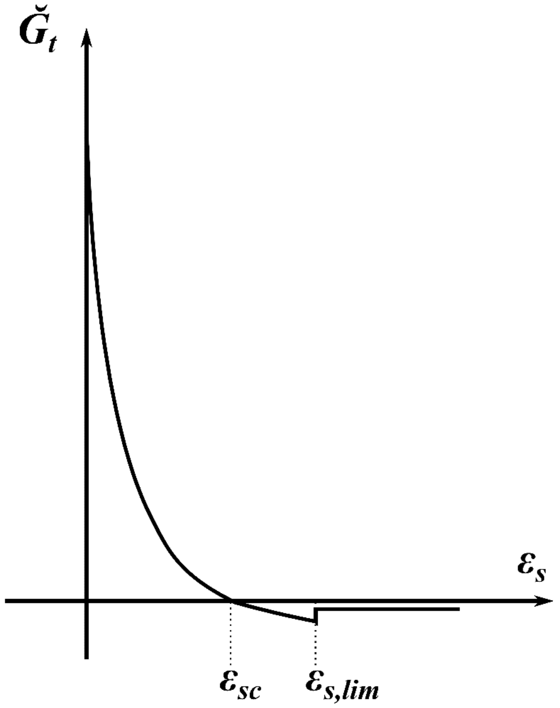

Figure 43. Schematic illustration of $\breve{G}_t$ for constant v_a and no tensile failure

4.3. Rotational springs

Considering rotational stiffness of the elements in RBSM and RBCS simulations is cumbersome and usually a workaround is implemented to avoid over complicating the model. In Chapter 2 and Chapter 3 the a very simple model was assumed which assumes that the adjacent elements of each element have no rotation and based on that a rotational stiffness is assembled over the stiffness matrix. This method will lead to overestimation of rotational stiffness if the elements have considerable rotation. Another alternative used in RBSM elements is introduced by Yamamoto et al. in which interface of rigid bodies are divided to allow a set of tensile springs account for moment resistance as cited in [47]. However, this method is expensive and cannot be simply implemented in RBCS elements.

Since simulation of beams in which accuracy of flexural stiffness is crucial is targeted in this chapter, this issue must be addressed. For this purpose, the resisting rotational moment is calculated based on the relative rotation of the rigid bodies (Figure 42). For this purpose, first the rotation of adjacent element of each ridge ($\varphi 1$, $\varphi 2$, $\varphi 3$) are added to displacement vector, $\{\mathbf{d}\}$, as given in Equation 65 and Figure 44. Then considering the relationship for the moment of a mutual ridge (M) and the curvature (κ)an analogy to the stress strain relationship is considered in which the moment (*M*) is analogous to the force and the moment of inertial (*I*) is analogous to the area, therefore *M/I* ratio represents the stress and κ represents the strain (Equation 66).

$$\{\mathbf{d}\} = \begin{Bmatrix} u_o \\ v_o \\ \phi_o \\ u_1 \\ v_1 \\ u_2 \\ v_2 \\ u_3 \\ v_3 \\ \phi_1 \\ \phi_2 \\ \phi_3 \end{Bmatrix} \qquad \text{Equation 65}$$

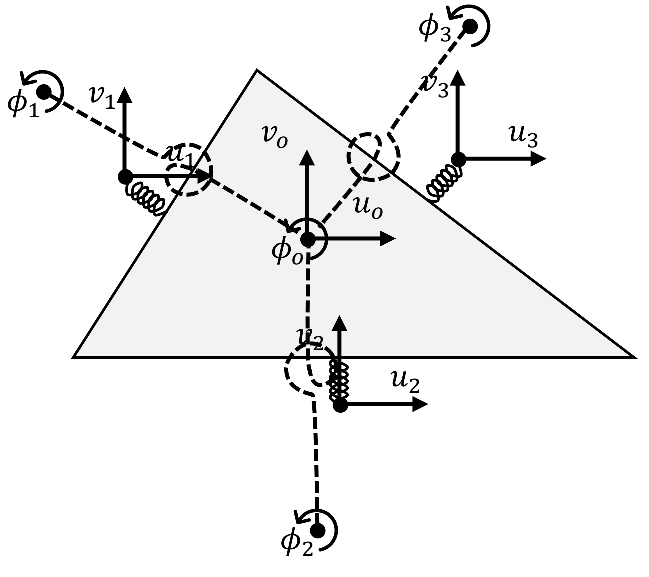

Figure 44. Modified RBCS element with rotational springs

$$\frac{M}{I} = E \times \kappa \equiv \frac{F}{A} = E \times \varepsilon \qquad \textit{Equation 66}$$

The curvature on each mutual ridge is calculated from the ratio of relative rotations of two rigid bodies to the normal springs' total length (h_1+h_2) as shown in Figure 45. With this analogy, the stress and strain vectors of the elements were expanded to keep values of M/I and κ of each ridge (Equation 67) and displacement-strain matrix, [**B**], and stress – strain relationship matrix, [**D**], were modified to convert relative rotation to curvature (κ).and curvature to M/I accordingly.

$$\{\boldsymbol{\varepsilon}\} = \begin{Bmatrix} \varepsilon_1 \\ \varepsilon_2 \\ \varepsilon_3 \\ \varepsilon_{s1} \\ \varepsilon_{s2} \\ \varepsilon_{s3} \\ \kappa_1 \\ \kappa_2 \\ \kappa_3 \end{Bmatrix}, \qquad \{\boldsymbol{\sigma}\} = \begin{Bmatrix} \sigma_1 \\ \sigma_2 \\ \sigma_3 \\ \tau_1 \\ \tau_2 \\ \tau_3 \\ (M/I)_1 \\ (M/I)_2 \\ (M/I)_3 \end{Bmatrix} \qquad \textit{Equation 67}$$

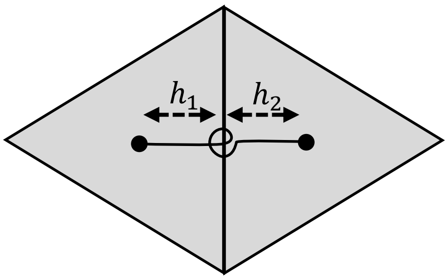

Figure 45. Distance to calculate flexural curvature between two elements

The rotational stiffness is ignored (failure of a moment spring) under two conditions. The first condition is the failure of one of the normal springs on the ridge. The second condition is if the tensile stress of the ridge evaluated on the farthest tensile fibre reaches the tensile strength of the normal spring. If any of these two conditions are satisfied, the contribution of that ridge to rotational stiffness of elements will be ignored.

For the ridges between elements with different materials the stiffness is estimated using an equivalent modulus of elasticity evaluated from Equation 66.

$$E_{eq} = \frac{E_1 E_2 (h_1 + h_2)}{E_1 h_2 + E_2 h_1} \qquad \text{Equation 68}$$

4.4. Analysis results and discussion

In this section, four cases including the uniaxial compression, direct tension, three-point flexural and direct shear are simulated by utilizing RBCS element for fibrous concrete. The properties of used in the simulations are given in Table 8 and 9 respectively.

Table 8. Input specification for concrete matrix

No.	Strength	Elastic Modulus*	Poisson's Ratio
1	60 MPa	3.64e4 MPa	0.2
2	40 MPa	2.97e4 MPa	0.2
3	35 MPa	2.78e4 MPa	0.2
4	30 MPa	2.57e4MPa	0.2

* $E_{[MPa]}=4700\sqrt{}\,(f'_{c\,[MPa]})$

Table 9. Specification and assumed pull-out key points for fibre types

Type	A.R.*	L[mm]	D [mm]	w_1[mm]	s_2[mm]	s_3[mm]	P_1[N]	P_2[N]	P_3[N]	Comment
1	62	13	0.21	0.05	0.40	4.00	4.65	3.53	0.00	Dramix LO 13/.20
2	57	50.8	0.89	0.05	0.40	12	55.0	45.0	30.0	round-straight
3	72	64	0.89	0.05	0.40	12	62.0	56.0	40.0	round-straight
4	80	60	0.75	0.05	0.40	25	50.0	45.0	0.0	Dramix RC 80/60

* Aspect Ratio

4.4.1. Uniaxial compression

To investigate uniaxial compression behaviour of high-strength matrix, 60Mpa concrete reinforced with the straight-round fibre with Specification of fibre type 1 in Table 9 and with Volume Fraction (V.F.) of 0%, 1% and 2% is simulated. The outcomes are compared with empirical models proposed by Soroushian and Lee and Ezelding and Balaguru [48,49]. For the model of Ezelding and Balaguru which only provides normalized stress – strain curve for straight fibre full response is obtained using the compressive strength of the SFRC (f'_{cf}) and the strain at peak (ε'_{cf}) are accordingly evaluated from equations adopted from [50] and (Soroushian & Lee, 1989).

For the case of normal strength concrete, 40MPa concrete is considered with type 2 and type 3 fibre of Table 9 with the outcome compared with an experimental study [51]. The discretization of the model is depicted in Figure 46.

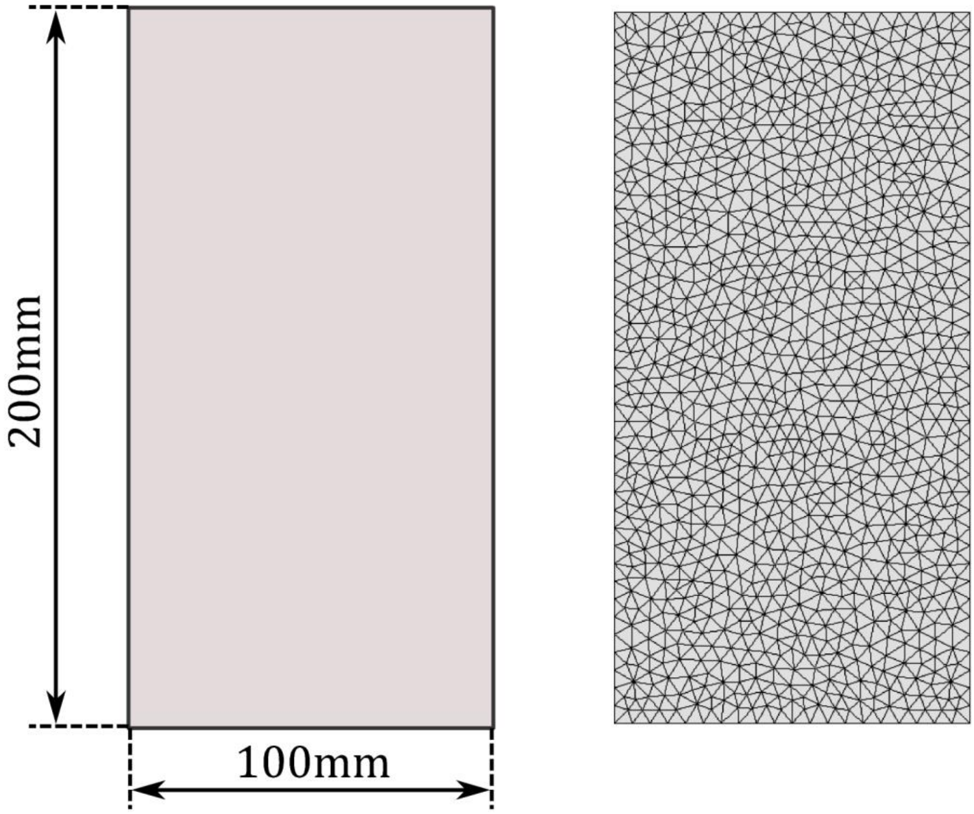

Figure 46. Uniaxial compression model dimensions and element arrangement

The stress-strain obtained from the modelled high-strength plain specimen is depicted in Figure 47a along expected responses as proposed by CEB-FIP model code 1990 [24] and Carreira and Chu [31]. Figure 47b and Figure 47c depict the response of the models with V.F. (volume fraction) of 1% and 2% along with the empirical models.

While 1% V.F. simulation matches with Ezeldin and Balaguru’s model, Soroushian and Lee’s model predicts a more ductile behaviour just as for the 2% V.F. (Figure 47c) while no comparison is possible with Ezeldin and Balaguru’s model for the 2% V.F. since the fibre content is beyond the range of the model.

Figure 48 compares the outcome of uniaxial compression test on normal strength specimen simulation using with the experiment depicted with dotted lines [51] and the empirical model [49] depicted with dashed lines. Increments can be observed in the ductility, peaks stress and the strain at peak for the simulated specimen which mainly coming from the increment applied to peak shear strain while the contribution to the tensile behaviour only occurs at the softening stage of normal springs cannot significantly improve the pre-peak respond.

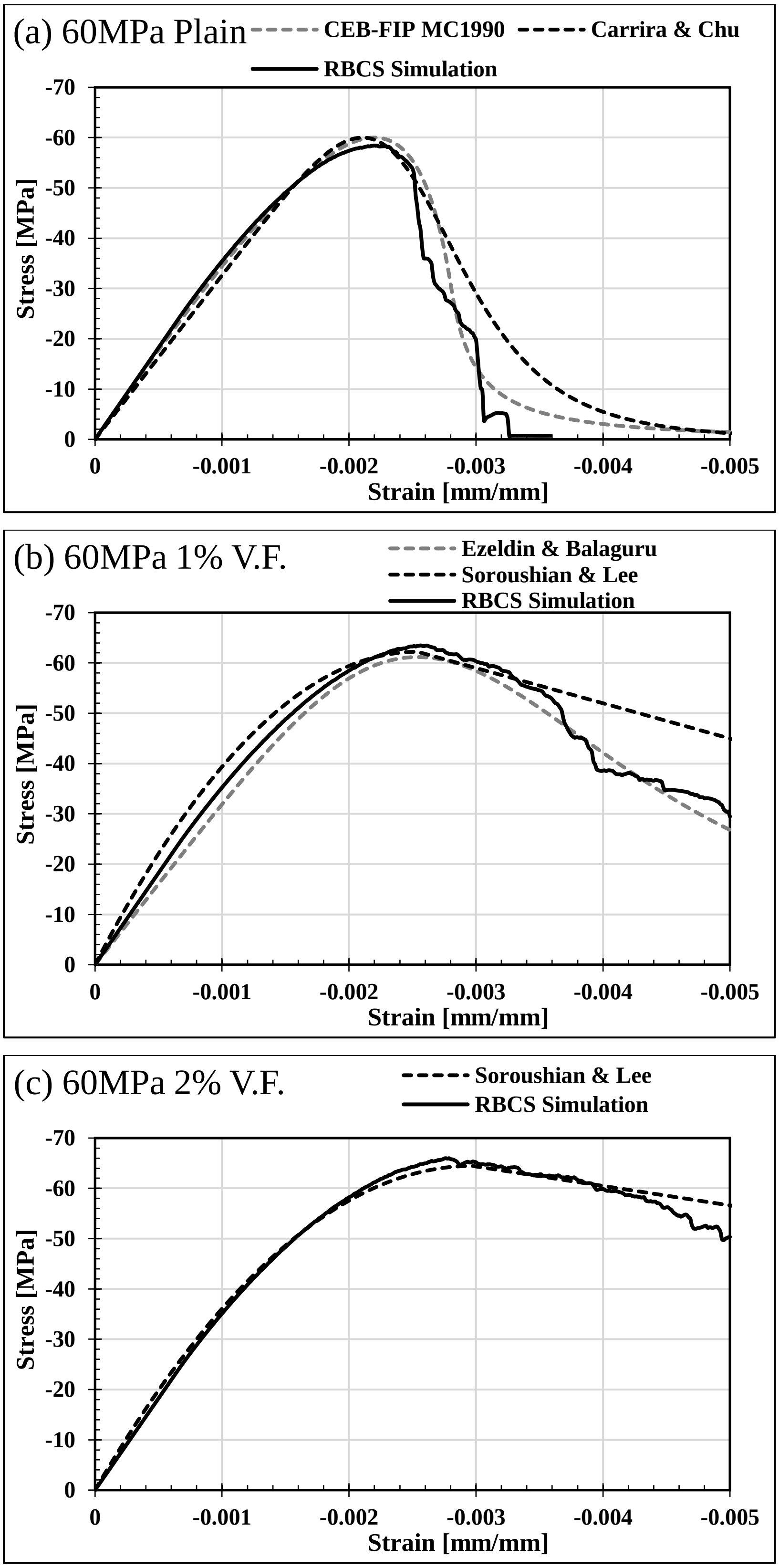

Figure 47. High-strength SFRC at uniaxial compression

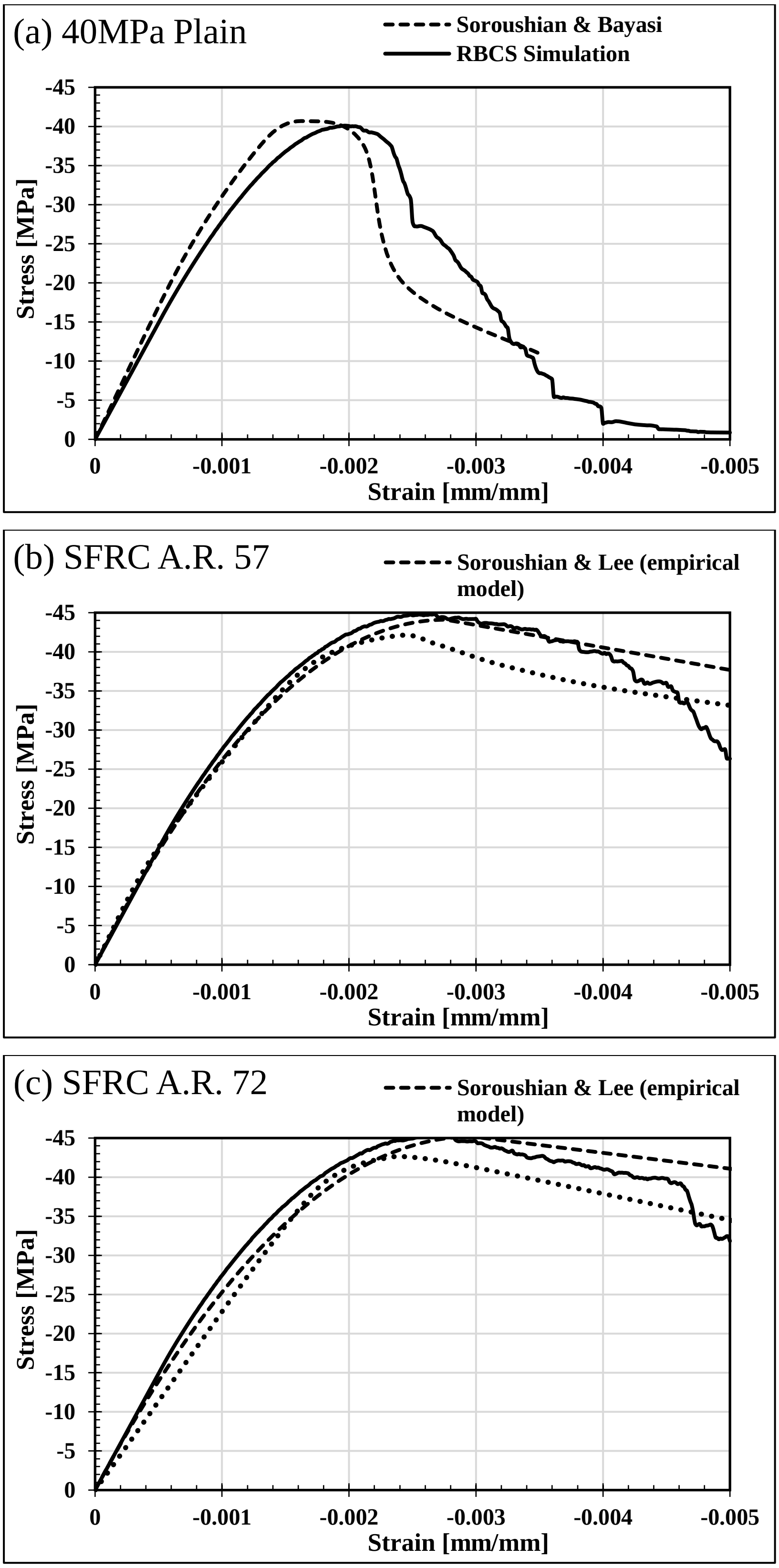

Figure 48. Normal strength SFRC at uniaxial compression

4.4.2. Direct tension

In this section an hourglass shaped dog-bone (Figure 49) adopted from [38] made up of 60MPa SFRC reinforced with 0.5% and 1.0% V.F. of the steel fibre (Table 9 – type 1) is simulated. The boundary condition is prescribed deformation (displacement control) assigned to top and bottom boundaries directly.

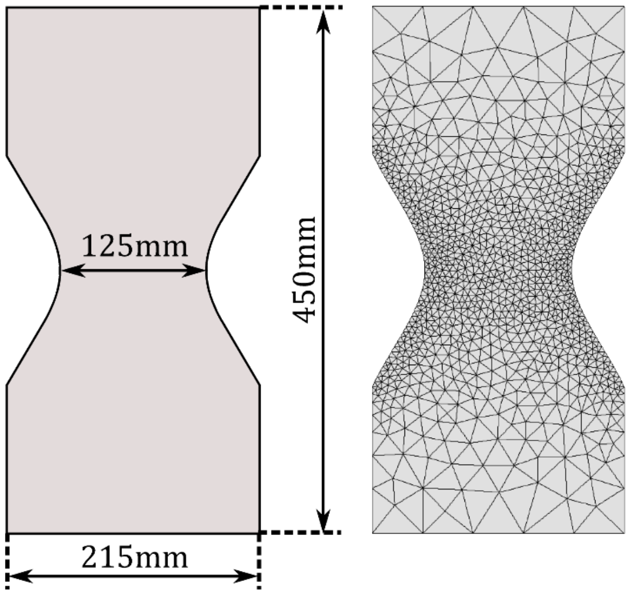

Figure 49. Direct tension model geometry and discretization

The tensile strength for simulated 1% and 0.5% V.F. specimens are approximately 3.5MPa; compared to the experimental data [38], that roughly ranges between 3.5MPa to 4.5MPa, is the lower bound. Just as observed in the experiments, due to abrupt release of the preserved elastic energy in the specimen and the loading machine, a sudden drop occurs after peak. Figure 50 depicts the simulated results aside with the region depicting the residual tensile strength from experimental data compared to which the simulation results seem consistent.

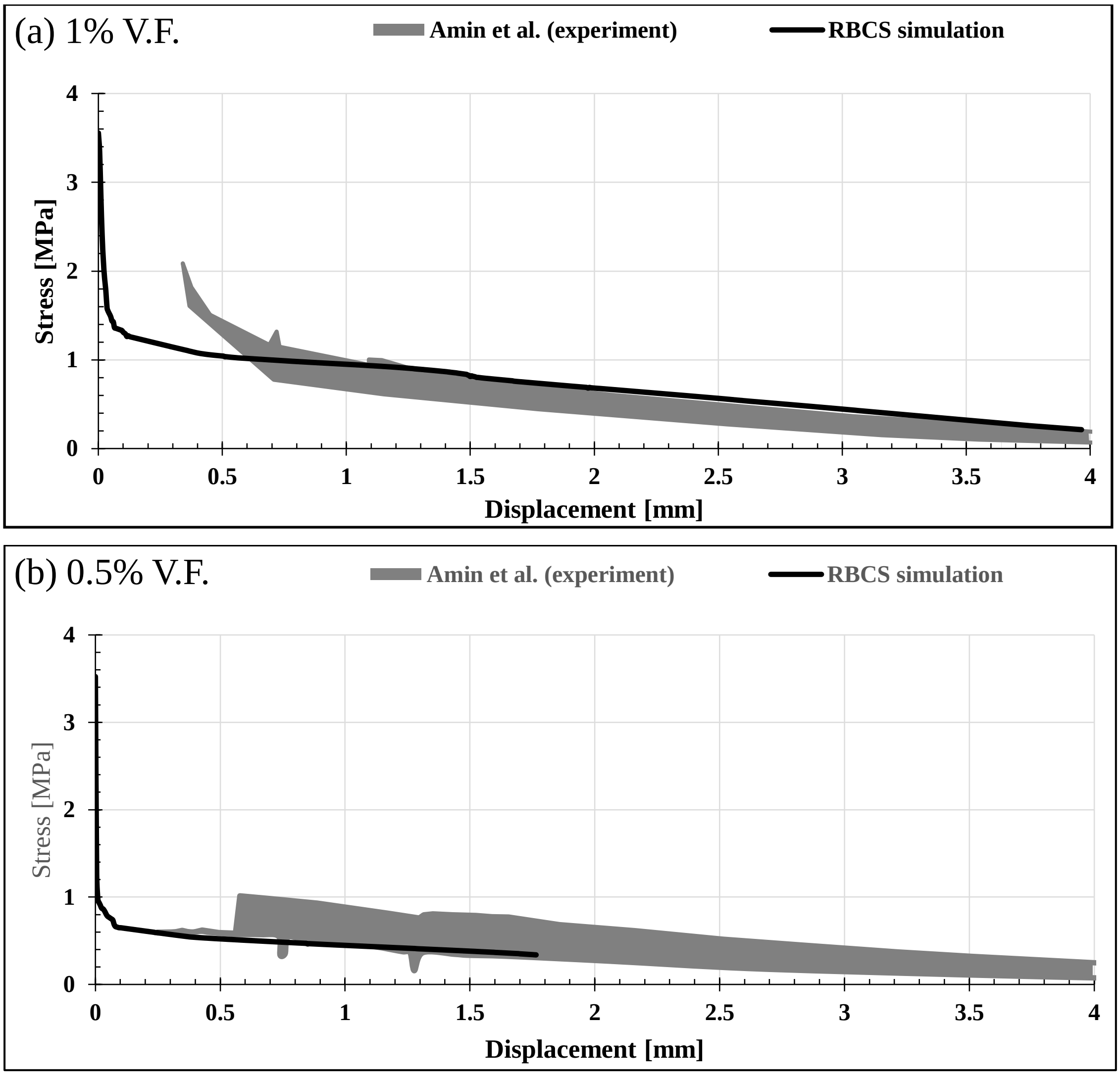

Figure 50. Direct tensile test simulation and experimental data

4.4.3. Three-point bending

To validate RBCS in flexural behaviour of concrete and SFRC beams, three point bending experiments on notched bending were adopted from [38] including experiments preformed on two beam specimen dimensions and two volume fractions (0.5% and 1.0%) of the steel fibre (Table 9 – type 1). The test set-ups are presented in Figure 51. The flexural tensile strength ($f_{tf,i}$) of the specimen can be obtained from:

$$f_{ft,i}(CMOD_i) = \frac{3F_i l}{2bh_{sp}^2} \qquad \text{Equation 69}$$

in which $CMOD_i$ and F_i respectively being the crack mouth opening displacement and loading force (P) at the specific loading stage i, l is the span length and the b and h_{sp} are accordingly the length and the unnotched height of the prism in the mid-span [25].

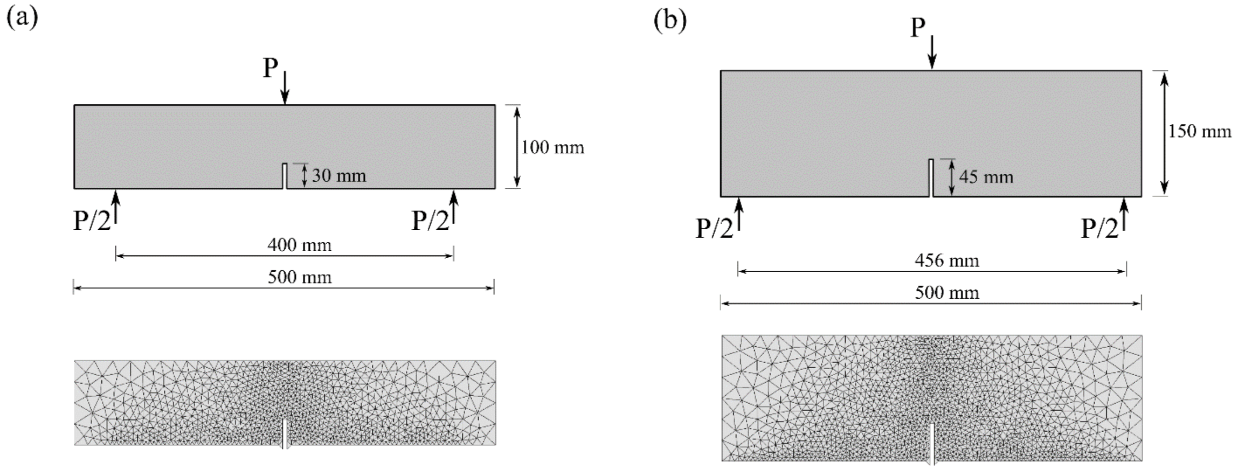

Figure 51. Three-point bending test beams and discretized models

The obtained peak loading forces from the simulation and experiment are respectively given in Table 10 and 11 along with calculated flexural tensile strength calculated from the equation above. According to the results, the increment in the fibre percentage marginally increase the flexural tensile strength in the simulated models and experiments.

Table 10. Simulation peak loads and corresponding flexural tensile strength

No.	Prism dimension	Fibre V.F.	Peak Load [KN]	$f_{tf,i}$ [MPa]
1	150mm	1.0%	16.93	7.00
2	100mm	1.0%	5.33	6.53
3	150mm	0.5%	15.65	6.47
4	100mm	0.5%	4.93	6.04

Table 11. Experiment [38] peak loads and corresponding flexural tensile strength

No.	Prism dimension	Fibre V.F.	Approximated Peak Load [KN]	$f_{tf,i}$ [MPa]
1	150mm	1.0%	15	6.20
2	100mm	1.0%	6.7	8.20
3	150mm	0.5%	12.5	5.17
4	100mm	0.5%	5.8	7.10

It can be observed that there are some differences between predicted peak loads in a way that in the simulation results compared to the experimental results, for the case of 100×100mm prisms, the predicted peak load is underestimated while overestimated for the 150x150mm prism. However, by comparing evaluated flexural tensile strength (f_{tf}), it can be observed that the simulation results obtained from 100×100mm prisms and 150×150mm prisms (Table 10) are more consistent while in the case of experiment there is a larger variance in the obtained flexural tensile strength for 100×100mm and 150×150mm prisms (Table 11). Therefore, the difference between simulation and experiment may come from the uncertainty of the behaviour of the concrete-like materials and the effect of test set-up like the effect of mould walls on the orientation of the fibre which should be more significant in the case of the smaller specimens. The distributions of displacements in the beams at induced displacement of 0.1mm to the plain and 1% VF beams are depicted in Figure 52. From Figure 52 it can be observed that the bridging action of fibres in tensile cracks can reduce the crack opening.

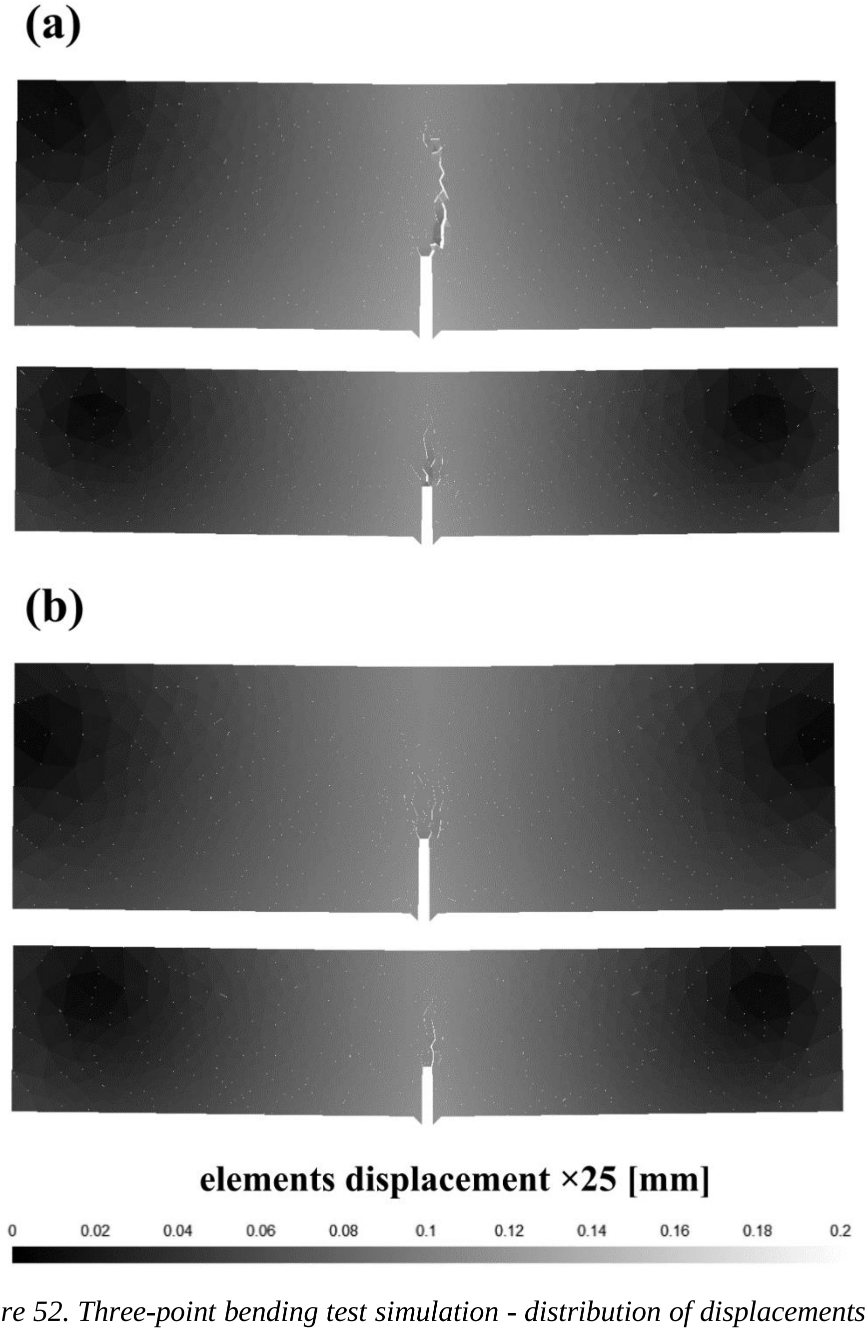

Figure 52. Three-point bending test simulation - distribution of displacements at induced deformation of 0.1mm for a) plain concrete beams b) SFRC 1% VF beams

The load versus crack mouth opening displacement (CMOD) of three-point bending test simulation of plain specimens is depicted in Figure 53 while Figure 54 depict result of SFRC prism simulation along with the experimental results [38].

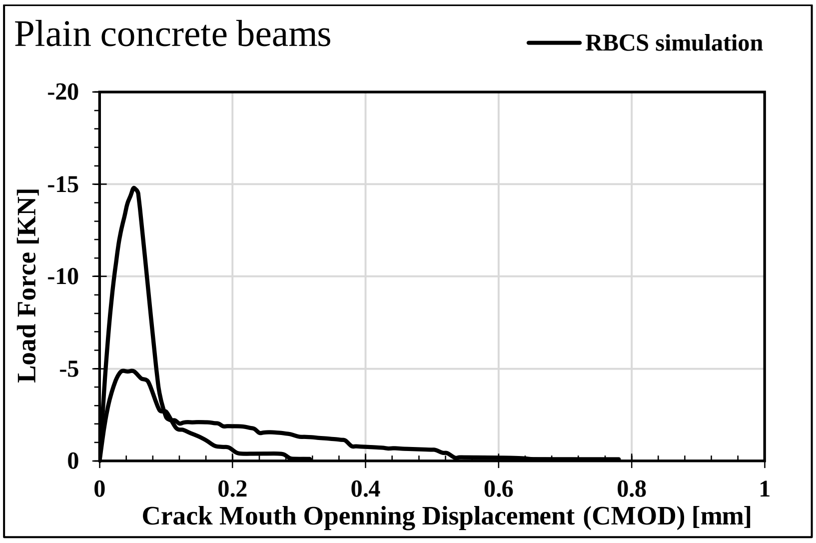

Figure 53. Three-point bending test simulation on plain concrete models

The outcome of the simulation shows that the behaviour of the simulated specimen is similar to the experimental results but for the experimental results the difference in the post peak residual strength between 0.5% and 1% V.F. mixes is less significant compared to the simulated results. This can be seen in behaviour of the simulated 150×150mm beam with 0.5% which has a lower residual strength compared to the 1% V.F. specimen. The mitigated difference in the case of experimental results could be due to ease of producing mixture with lower fibre content, like better dispersion of the fibre or mixture components making lower fibre contents be compensated with better mix quality. However, in the case of simulation, these effects are not implemented, and the behaviour of the model is directly affected by the given volume fraction of the fibre. Another note that can be pointed out by comparing simulation and experimental results is that the simulated flexural behaviour has a more sudden drop after peak. One probable reason for this behaviour can be that the fibre contribution in the model is mainly based on bridging action while the effect of dowelling action and the pull-out in mode II fracture of the fibre [52] are not directly considered due to limited studies performed on this subject. Yet the outcome is satisfying considering that the results of the simulation may be improved further by calibration of the pull-out key points (Table 9) for each experimental case.

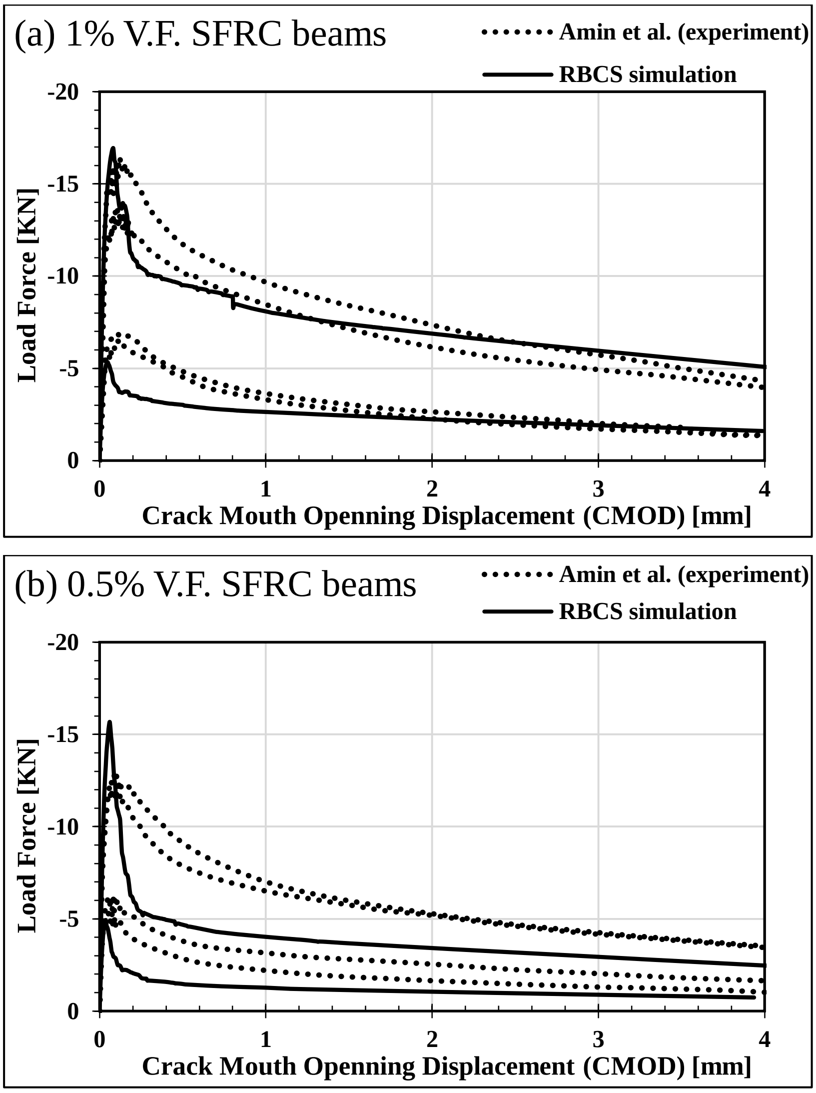

Figure 54. Three-point bending test results for 150×150mm prisms (higher curves) and 100×100 prisms (lower curves) a)1% V.F. mix b)0.5% V.F mix

4.4.4. Direct shear through push-off

In this section, a push-off test is simulated on plain concrete and SFRC specimens. Due to lack of the reports on push-off test using straight steel fibre a test set-up proposed by Barragan et al. using hooked steel fibre (type 4 in Table 9) is used as an experimental reference [53]. Since current model does not calculate the mechanical bond due to anchor effect of hooked fibre a smaller residual strength is expected from contribution of the fibre content. The test set-up and the discretised model are presented in Figure 55. The discretization dimension is increased to reduce calculation cost in areas where failure is not expected. Displacement control is applied to the boundary of steel strips with no displacement constraint in horizontal direction. The boundary is made in a way that no moment reaction is generated on the prescribed boundaries.

The steel and concrete interface of steel strips and the specimen are similar to previous sections. The elastic modulus of steel is assumed equal to 2×10^5 MPa and Poisson's ratio is assigned 0.3. The strength of the matrix is assumed 35MPa in the simulation to represent C30 grade concrete used in the experiment with mechanical properties given in Table 8 and fibre content is 0.5% V.F. for SFRC specimens.

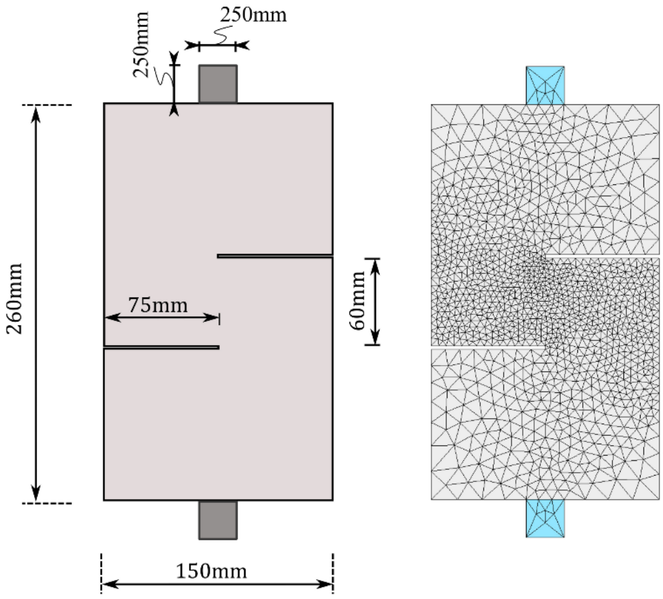

Figure 55. Push-off test set-up and the corresponding discretized RBCS model

The outcome of push-off simulation is depicted along with experimental results in Figure 56. The modelled plain specimen has a delayed failure compared to the experiment in which a split crack causes early failure of the specimen. For the case of plain model, at deformations larger than 0.2mm the analysis did not continue after more than 20,000 and the model was deemed unstable due to failure. The post-peak residual strength observed after peak for the experiment is larger which could be the effect of anchors at the end of hooked fibre.

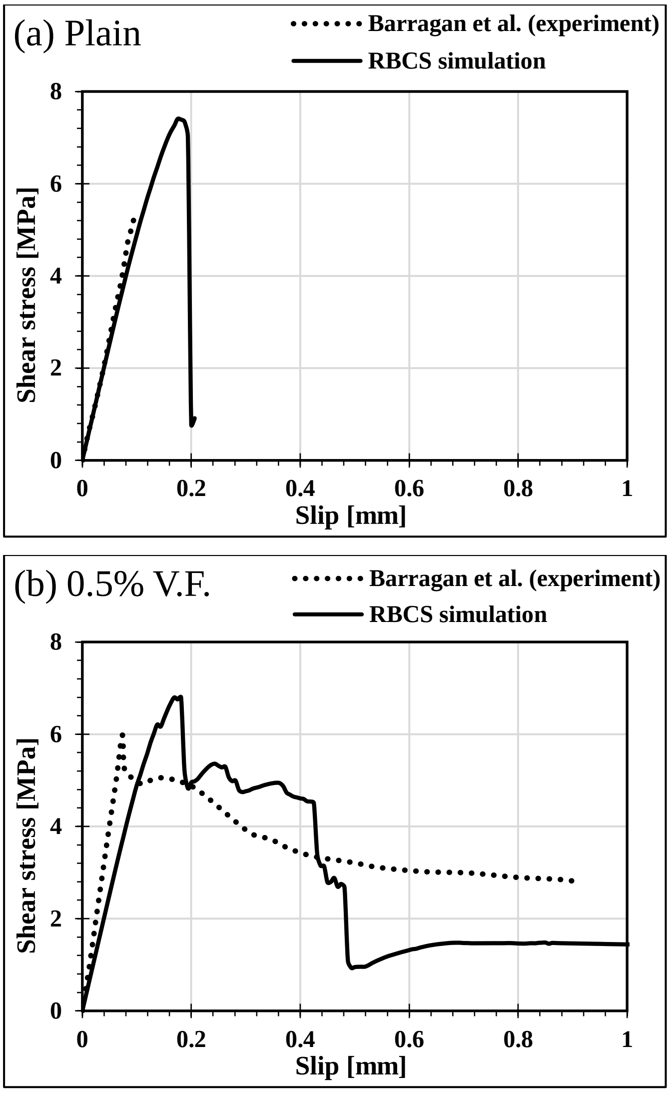

Figure 56. Push-off direct shear test for a) plain concrete b) 0.5% V.F SFRC

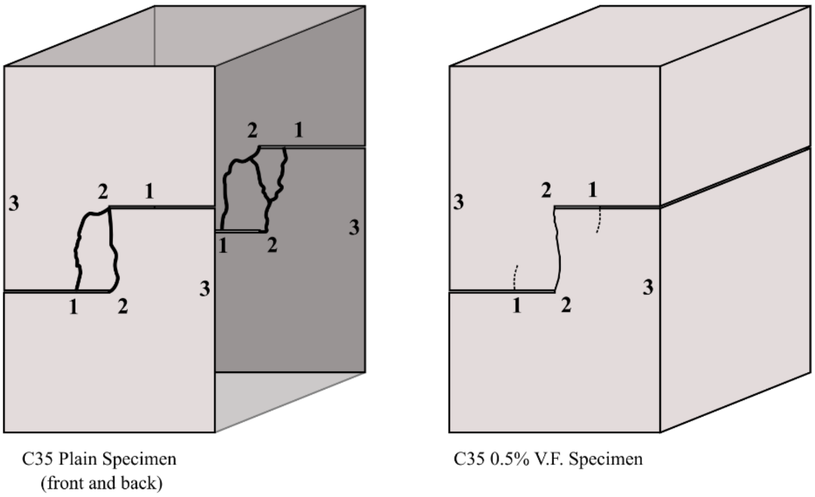

Figure 57. Observed crack patterns reported by [53]

Observed crack patterns reported by [53] are depicted in Figure 57. The tensile cracks formed from point 1 can interfere with shear failure plane at 2-2 section for the plain specimens while in fibres can prevent the tensile failure to be pronounced in the case of SFRC specimens. A similar failure patterns are observed in the RBCS simulation as shown in Figure 57 and Figure 58.

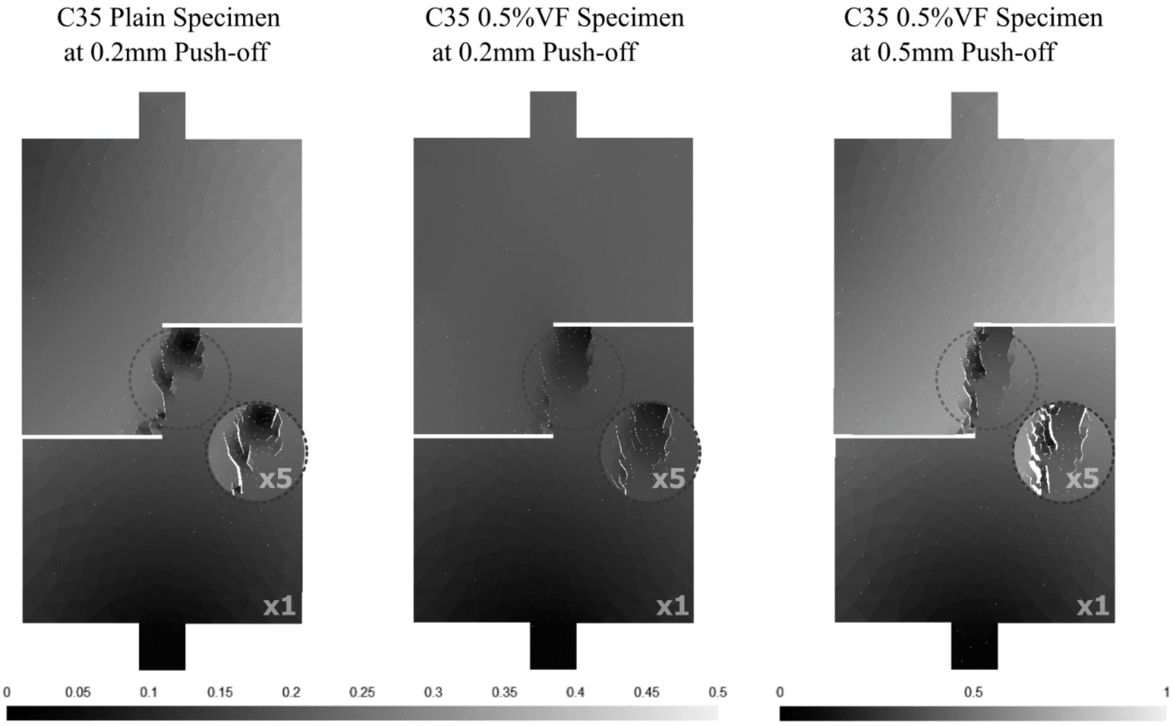
C35 Plain Specimen at 0.2mm Push-off

C35 0.5%VF Specimen at 0.2mm Push-off

C35 0.5%VF Specimen at 0.5mm Push-off

Figure 58. RBCS push-off with mapping of displacements (numbers in mm)

4.5. Bottom line

In this chapter the models developed in former chapters are utilised using an additional algorithm which calculates the inclined pull-out stress of an imaginary fibre spring. This method is based on the direct and inclined pull-out models for steel fibre and is implemented in tensile behaviour of normal springs.

This method however was not enough to replicate the improvements observed in compressive behaviour of fibrous concrete. This may indicate effect of fibres not only in tensile direction but also in shear direction via effects such as dowelling action and shear pull-out. Interestingly not many researchers have performed experiments on shear pull-out or emphasized contribution of such actions to improvement of fibrous concrete composites.

In this research such affects were added to the model by increasing the strain corresponding to peak shear stress in shear springs in meso-scale behaviour. By adding this behaviour to the constitutive models, it was observed that the macroscopic behaviour of the was improved and became similar to the observed experiments.

The proposed model was also used to simulate cases such as direct tension, flexural test and direct push-off tests. It was observed that for the simulated cases the model provides acceptable predicting for the behaviour of the specimen. It should however be noted that the proposed model does not incorporate the negative effect of excessive amount of fibre on the material or the effect of specimen shape on the tendency of the common fibre directions and therefore it might overestimate the effect of fibre in high volume fractions or show different behaviour for smaller specimens which due to wall effect the fibre tend to be aligned in a more favourable direction.

Chapter 5

Application of RBCS into simulation of structural element

Application of numerical methods has been beneficial in the study of structures and structural members. Performing experiments on large structural members is usually difficult and expensive and if a large number of tests needs to be performed it can be time consuming, costly and sometimes barely feasible. Numerical simulation can help to reduce number of the tests that need to be performed thus eliminate necessity of performing a large number of costly tests. A good example of application of numerical simulation to avoid performing an extreme number of real-size tests can be seen in [54].

On the other hand, application of Application of discrete models into structural members and structures can be very beneficial to studies performed on those specific members. These methods may help illuminate the failure mechanism of the targeted problem and simulated cracking and discontinuities that occur in the member. The AEM method introduced earlier in this manuscript can even be employed in realistic simulation of demolishing structures where FEM is barely able to perform such simulations. RBSM and RBCS method also have advantages over FEM when it comes to studying the fracture process and cracking of concrete members. Further improvement of such method can result in attaining powerful tools that can simulate large deformations and late stages of failure in concrete members. Also, the abilities of RBCS such as possibility to demonstrate the internal stresses can give advantages to this method over RBSM. It should be noted that these abilities however come with higher calculation costs.

It is worth mentioning that prior to this study, RBSM-base techniques has been utilized to study structural members failure such as effect of mechanical anchorage of rebars in beam-column knee connection [34], or studies performed to improve the understanding on mechanism of failure and crack propagation of structural members under monotonic and cyclic load such as [47] and [55]. In our laboratory however this method has been mainly applied only in material level. One major reason is the limitation of Graphical User Interface of the RBSM software that puts a big limitation on freedom of model definition. This limitation being recognized at the early stages of this study, a new method for model definition was employed to prove a huge freedom to the user for defining the model and make it possible to perform simulations on models with complicated geometrical definition. However, the limitation of 2-dimensional simulation and of course the computational hardware limitations remain. In order to lift these barriers further studies has to take place on this method. The model can be improved to three-dimensions and the computational cost can be reduced significantly.

This chapter tries to demonstrate the application of introduced element in structural element level by simulation of newly introduced cast in-situ shear connection in prefabricated concrete wall elements [56,57]. This connection is chosen since the behaviour of this connection is still under investigation and the detailed failure mechanism of this connection is given in the performed studies. This can make it possible to easily compare the behaviour of the RBCS simulation with the real experiment. Also, since the Digital Image Correlation (DIC) technique is used in the investigations it is possible to compare the cracking in the experiment with the simulation.

The stages of the study include:

1) Development and calibration of a model for connection with key depth of 10mm known as D10 specimens
2) Increasing the key depth to 20mm to simulated and predict the behaviour of another specimen known as D20

One of the main concerns in this section is the calculation expenses and limitation of the available hardware. Therefore, the mesh size in this simulation is larger than previous sections and this may affect the accuracy of results and cracking. This matter will be discussed in the following sections.

5.1. Introduction to the targeted experiment

The targeted experiment on this type of connection is a push off experiment in which, as depicted in Figure 59, the failure zone consists of casted grout mortar connecting the precast parts.

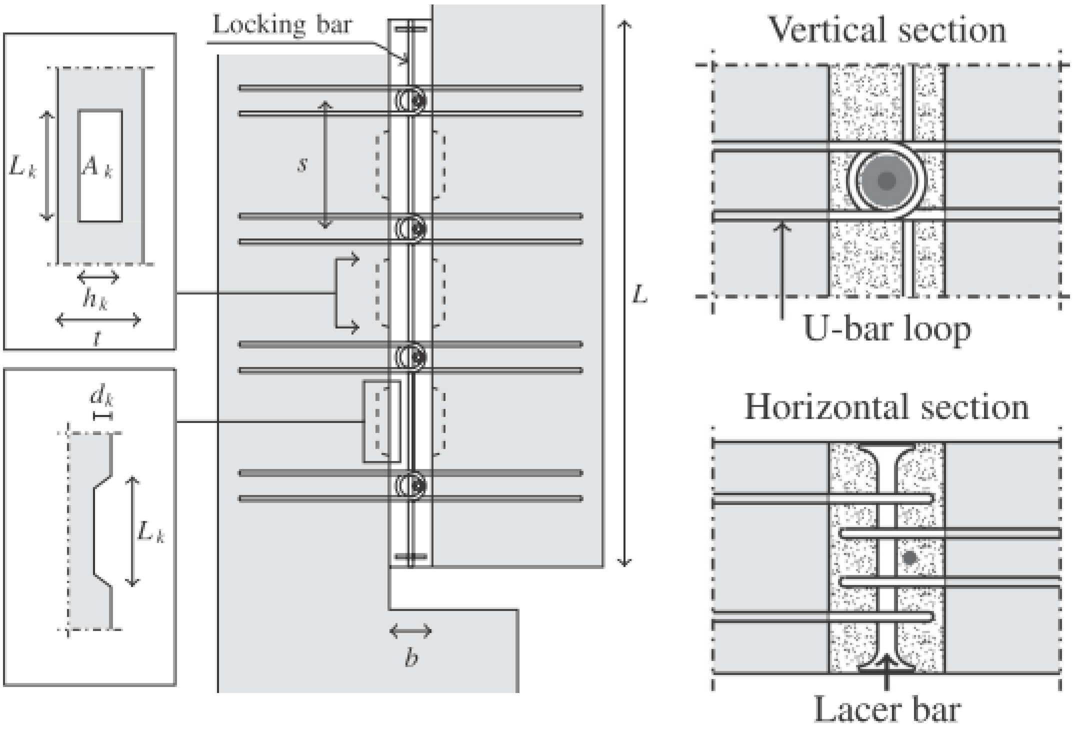

Figure 59. Targeted shear connection proposed by Sørensen et al. [56,57]

The shear transfer is done through designated shear keys while U-shaped reinforcements, called U-bars, provide tensile resistance. U-bars from each side meet in a location forming a loop which is locked by a horizontal lock bar. Additional vertical lock bar also exist which connects all of the loops together.

To capture both the behaviour of the middle keys and end keys, Sørensen et al. arranged three shear keys and four loop connections. The U-bars in the loop are designed in a way that they will yield in the case of failure of the connection.

5.2. Material Models

5.2.1. Material model for RC precast element

Since no major failure is expected in precast elements, except for the areas near shear keys (as pointed out in Figure 64), no failure is defined for these elements and they are assigned with the elastic mechanical properties of concrete of the same compressive strength. For precast elements near shear keys concrete material model is used (refer to 5.2.2).

5.2.2. Material model for grout and concrete

The material model for grout and precast concrete at the vicinity of shear keys is the same as the material model of SFRC material with zero volume fraction of fibre. This material model is used for grout mortar and part of precast element which connects to shear keys and is subject to possible cracking (Figure 64). A small modification in shear springs is performed in this chapter which limits the maximum stress of shear springs to half of macroscopic strength of concrete ($v_a = \alpha v_c \leq f_c'/2$). This modification prevents the conditions in which the strength of shear springs will increase excessively in large compressive stresses (Figure 60).

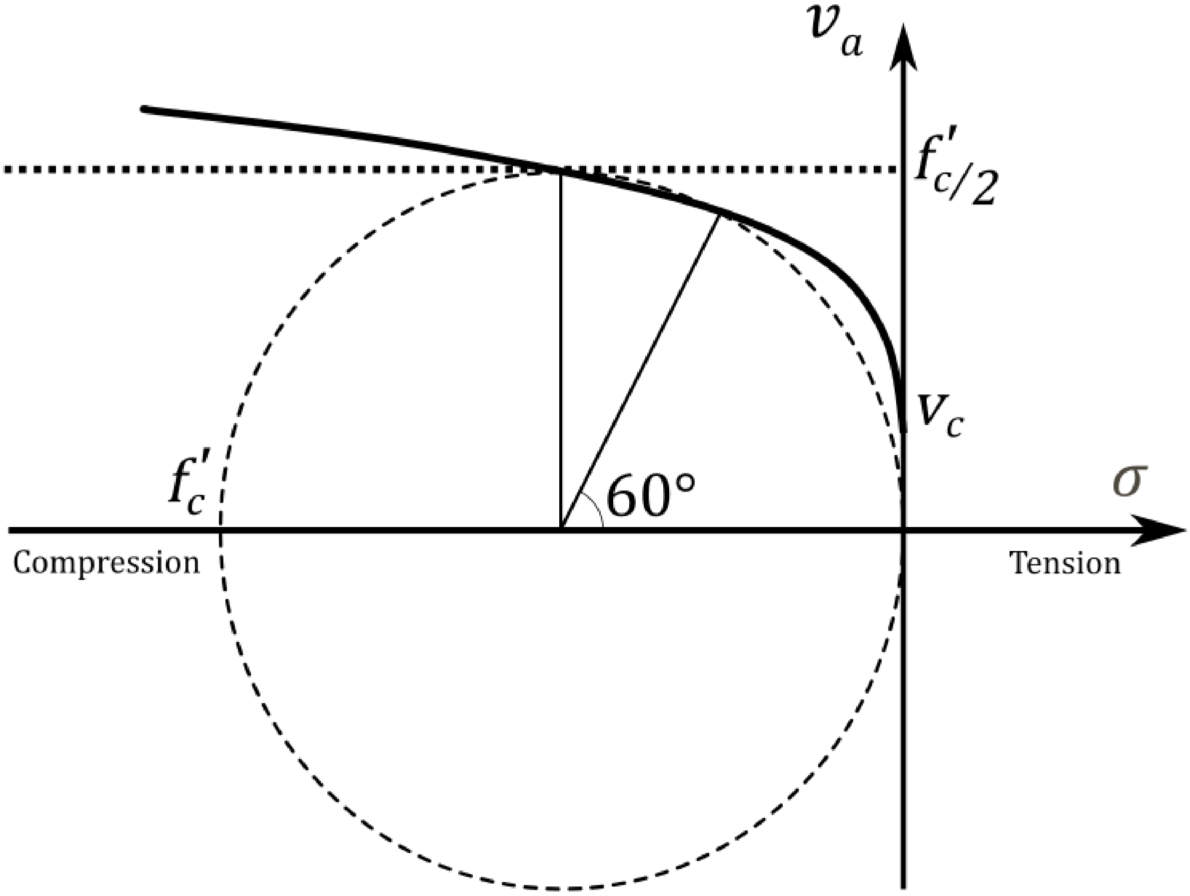

Figure 60. maximum shear stress as a function of normal stress

To avoid prolixity the concrete material model will not be described again and the reader is referred to section 4.2. for detailed information.

5.2.3. Concrete-grout Interfacial Transition Zone (ITZ)

In blocked discrete models the targeted modelled volume is tessellated into discrete blocks connected via zero-length springs. This concept makes introduction of ITZ elements by modification of corresponding springs to be properly applicable.

Since the bond between old (precast element) and fresh (grout) concrete is known to be weaker than internal bound of the compound on both parts, this weakness is considered in the model by introducing ITZ between grout and precast parts. ITZ is created by modifying the interfacial spring on the grout side.

It is not easy to estimate the strength of the ITZ since many parameters can play role such as the type of the grout and the conditions of casting the grout in place [58]. Therefore, calibration is performed on D10 specimens and good results are obtained with reduction factor of 40% for tensile springs (i.e. reducing tensile strength of interface to 40% of internal tensile strength) and 50% for shear springs. These values for strength of ITZ match well with the experiments of Xiong et al., on bound between old and new concrete, in which tensile strength of 42% and shear strength of 52% is observed in splitting tension and slant shear tests for old-new concrete interface with split-broken surfaces [59].

Since the ITZ is the weak link in the connection it is clear that ITZ will fail at some stage of loading and a post-failure behaviour should be considered for the ITZ. The theory of the current element is based on infinitesimal strains and small rotations and will not be suitable for applications of large deformations which is beyond the scope of this study. While this matter will be postponed to future studies, the main focus remains on the pre-peak behaviour of the model and it’s cracking at early stages after peak. Considering this matter, the failed concrete-grout ITZ model can only provide reaction in normal direction and will not consider friction effects after failure of the bond which seems to play an important role in the post-peak residual strength of the connection [57]. This simplification will help the convergence of the analysis and make it possible to reduce the mesh size.

5.2.4. Material model of the steel bars

For the steel material model, it is assumed that in tension on compression the yielding happens at yield stress of Fy while for shear stress it occurs at 0.6×Fy. Based on these assumptions, the interaction of tension and shear are considered by defining the yielding criterion as:

$$\sqrt{\left(\frac{\sigma}{f_y}\right)^2 + \left(\frac{\tau}{0.6 f_y}\right)^2} < 1. \qquad \textit{Equation 70}$$

If above is violated the normal and shear stress are replaced with σ' and τ' in a way that

$$\left(\frac{\sigma'}{f_y}\right)^2 + \left(\frac{\tau'}{0.6f_y}\right)^2 = 1$$ *Equation 71*

while

$$\frac{\sigma'}{\tau'} = \frac{\sigma}{\tau} = R_{ns}$$ *Equation 72*

in which R_{ns} is the ratio of normal to shear stress before correction. For the purpose of programming the above concepts are modified using:

$$\sigma = \tau \times R_{ns}$$ *Equation 73*

and from Equation 71 and 73, F_{tr} is defined as

$$F_{tr} = \sqrt{\left(\frac{\tau.R_{ns}}{f_y}\right)^2 + \left(\frac{\tau}{0.6f_y}\right)^2} = \tau\sqrt{\left(\frac{R_{ns}}{f_y}\right)^2 + \left(\frac{1.667}{f_y}\right)^2}.$$ *Equation 74*

.

Correction of stress is done by correcting F_{tr} to F'_{tr} based on:

$$F'_{tr} = \tau' \times \sqrt{\left(\frac{R_{ns}}{f_y}\right)^2 + \left(\frac{1.667}{f_y}\right)^2} = \tau' \times \frac{F_{tr}}{\tau} = 1.$$ *Equation 75*

Then corrected stress are calculated from F_{tr} accordingly:

$$\tau' = \frac{\tau}{F_{tr}}$$ *Equation 76*

$$\sigma' = \tau' \times R_{ns}.$$

The behaviour of the steel material model introduced in this section for two simple cases are shown in Figure 61.

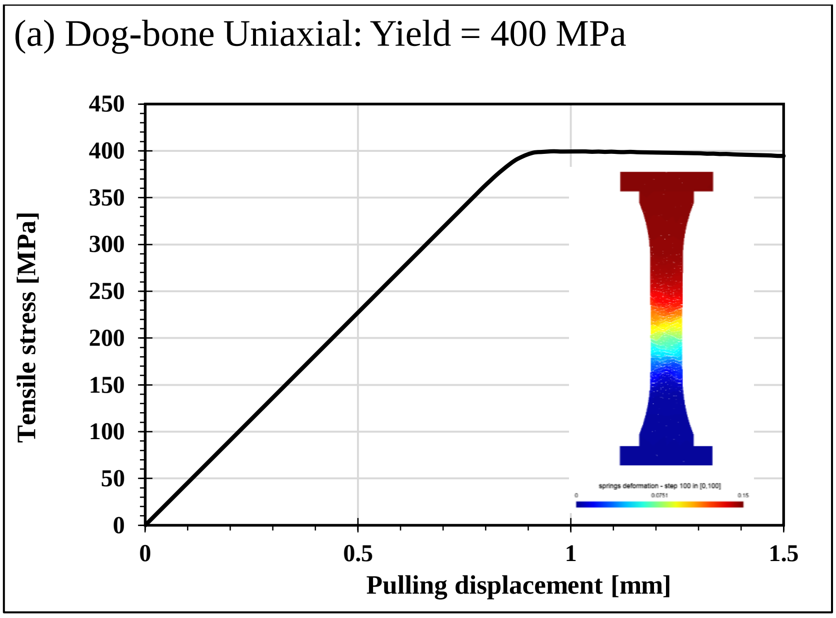

(a) Dog-bone Uniaxial: Yield = 400 MPa

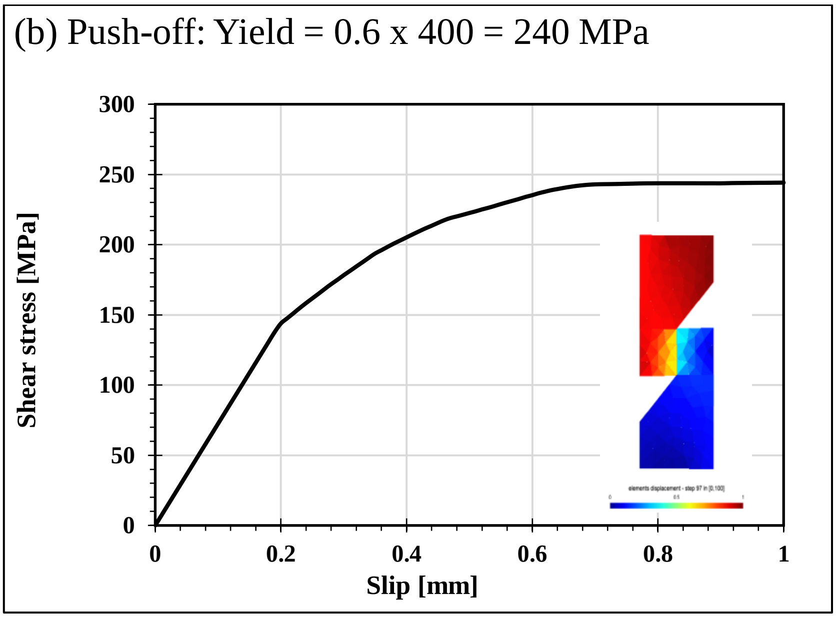

(b) Push-off: Yield = 0.6 x 400 = 240 MPa

Figure 61. Behaviour of the steel material in case of a) dog-bone b) push-off

5.3. Modelling and pre-processing

5.3.1. Simplification of the problem

Usually to perform 2-dimensional simulations require some scarification in the modelling to adapt the case in to a problem that can be defined in two dimensions.

As depicted in Figure 59, in Sørensen et al.’s design, height of shear keys (h_k) can be smaller than the model depth however in this manuscript only experiments in which dept of shear keys is equal to specimen dept is considered (i.e. $h_k = t = 200mm$) to make 2-dimensional simulation feasible.

Another issue is the loop connection in which U-bars and V-bar are not in the same plane and the concrete inside the loop has an out of plane failure (if it has a failure). If the simulation of the loops is intended, it is possible to simulate the elements of U-bar in a way that they are not directly connected as depicted in Figure 62. However, the main problem is the uncertainty about the behaviour of the concrete inside the loop and the relation of this area with the grout.

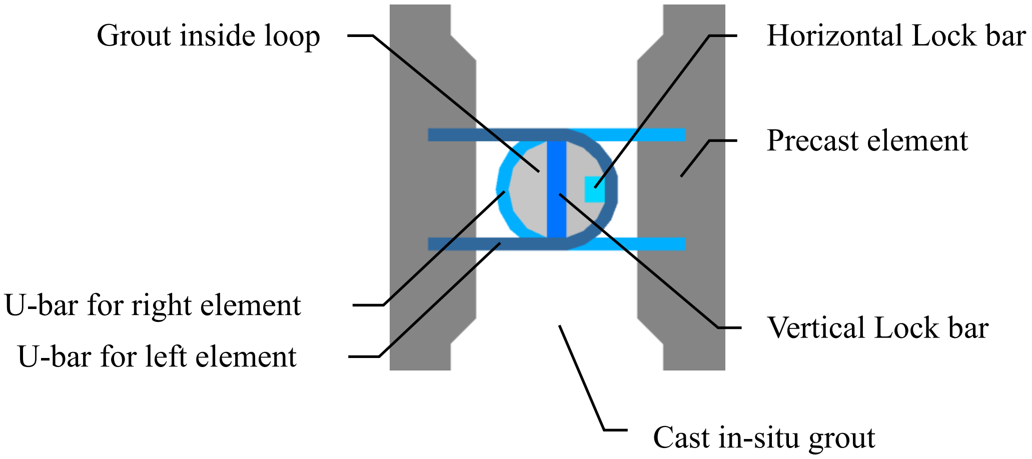

Figure 62. A possible alternative for simulation of loop connection in a 2-D model

To resolve the issue, based on the idea that the failure in the reinforcements happen due to yielding of the U-bars the simulation of the loops is avoided by assuming the U-bar reinforcements connect the precast elements directly and accordingly provide a passive confinement for the shear connection (Figure 64). However another issue that remains is the unrealistic confinement that vertical bars and horizontal bars will create in the 2-D model while as shown in horizontal section in Figure 59, beside the fact that the diameter of these bars is negligible compared to the depth of the specimen, these bars don’t exist in the same plane and the created confinement effect is unrealistic. It should be noted that the functionality of U-bars is to perform tensile resistance for the connection. Base on his note, the mentioned issue is resolved by omitting the contribution of the horizontal bars to the grout mortar behaviour by modelling them independent from grout elements while the effect of modelling vertical bar is investigated in simulations.

Since the strength of the precast concrete (which is reinforced with steel bars) is higher than the grout mortar, no failure model is assumed main part of precast elements but for the areas near the shear keys where an extreme stress concentration exists as shown in Figure 63, partial damage may occur in precast elements. Therefore, the nonlinear behaviour is assigned to the precast side near shear keys (Figure 64).

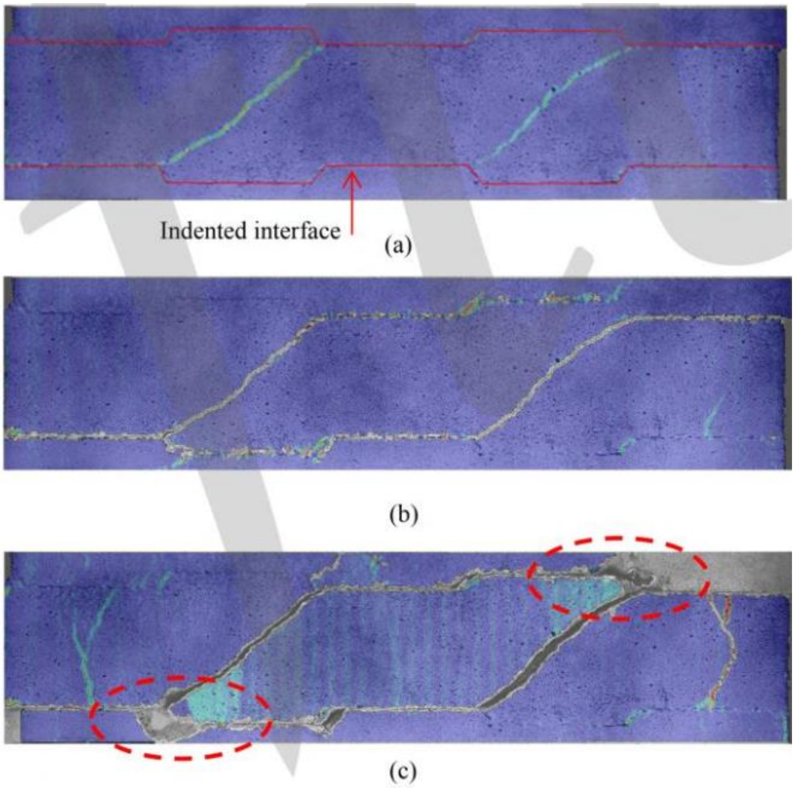

Figure 63. Cracking of a case of keyed connection in push-off test a) before peak b) at peak c) late stages of loading, by Sørensen et al. [60]

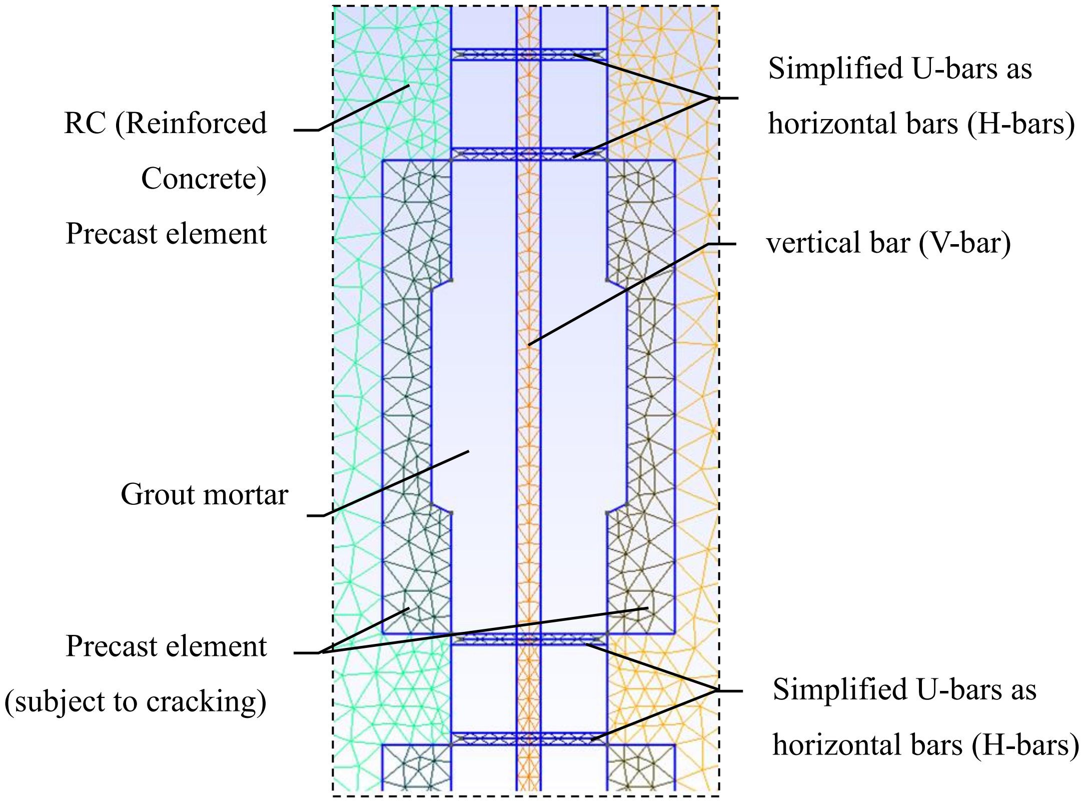

Figure 64. Simplified model of the joint

5.3.2. Meshing and input parameters of specimen series D10

The D10 specimen series are the specimens with shear key depth of d_k = 10 mm (Figure 59). This series of the specimens were used to calibrate the model. The model was simulated with and without vertical bar to see the effect of vertical bar to see the effect of V-bar on the pre-peak behaviour of the model.

The depth of the specimen is 200 mm, but the simulation performed for unit depth of the specimen and then converted to 200 mm to compare with the experiment. Accordingly, a correction (equivalence) factor is needed for reinforcements that don't exist within the whole depth of the specimen.

The input mechanical properties given in the Table 12 are chosen based on the information provided in the experimental study of D10 series [57]. Since the detailed mechanical properties of the grout mortar is not known the properties of the corresponding concrete material is assumed base on the given strength of the grout.

The model inside the connection is meshed using approximated 10 mm element size. Due to hardware limit meshing of smaller size is not possible. The element size gradually increases for the rest of the model to reduce calculation cost. The meshed model is depicted in Figure 65.

Table 12. Input mechanical properties of D10 specimen

No.	Part	Parameter	Notation	Value
1	Prefabricated element (no failure for RC part)	Compressive strength	f_c'	58.2 [MPa]
		Elastic modulus	E_0	35900 [MPa]
		Poisson's ratio	ν	0.2
		Focal strain	ε_{foc}	-1.24e-4
2	Grout mortar	Compressive strength	f_c'	45.0 [MPa]
		Elastic modulus	E_0	31500 [MPa]
		Poisson's ratio	ν	0.2
		Focal strain	ε_{foc}	-1.24e-4
3	Steel reinforcement H-bars (equivalent thickness of 9.42mm / 200mm)	Yield stress	f_y	517 [MPa]
		Elastic modulus	E_0	200000 [MPa]
		Poisson's ratio	ν	0.3
		Equivalence depth*	--	9.42 [mm]
4	Steel reinforcement V-bar (equivalent thickness of 9.42mm / 200mm)	Yield stress	f_y	599 [MPa]
		Elastic modulus	E_0	200000 [MPa]
		Poisson's ratio	ν	0.3
		Equivalence depth*	--	9.42 [mm]
5	Steel Bearing	Yield stress	f_y	∞
		Elastic modulus	E_0	200000 [MPa]
		Poisson's ratio	ν	0.3
		Equivalence depth*	--	200 [mm]
6	Anchor (depth and yield stress assumed)	Yield stress	f_y	599 [MPa]
		Elastic modulus	E_0	200000 [MPa]
		Poisson's ratio	ν	0.3
		Equivalence depth*	--	65 [mm]

*Equivalent depth of the element for 200 mm depth of specimen

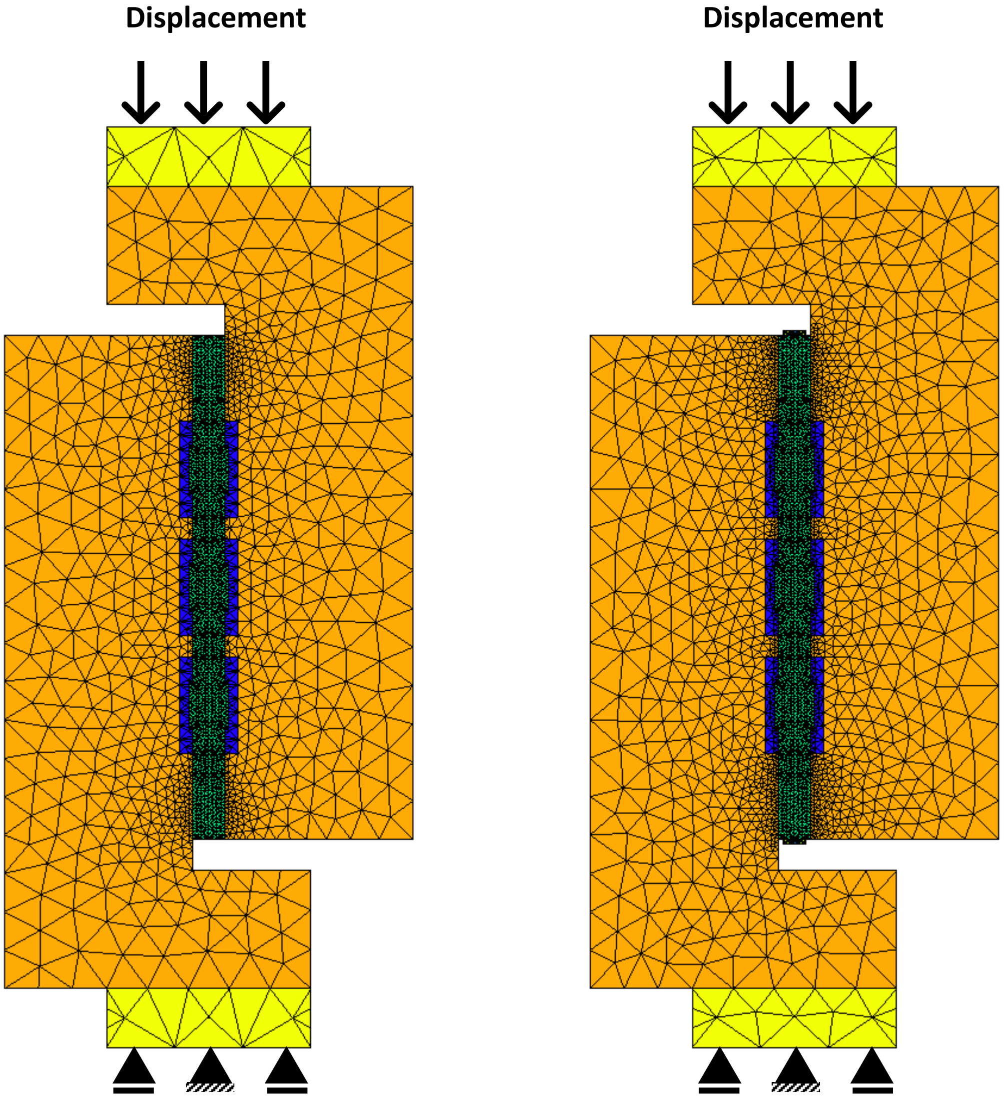

Figure 65. Modeling and meshing of D10 model without (Left) and with vertical bar (right)

5.3.3. Meshing and input parameters of specimen series D20

The D20 specimen is based on D10 model with V-bar. The model is simply created by increasing the depth of the shear key (Figure 59) from d_k = 10 mm to d_k = 20 mm. The model for D20 is depicted in Figure 66. While the strength of grout is slightly different (2.6 MPa weaker) this marginal difference is ignored to keep the results comparable with D10 model and the same input as in Table 12 is used in the simulation of D20 specimen.

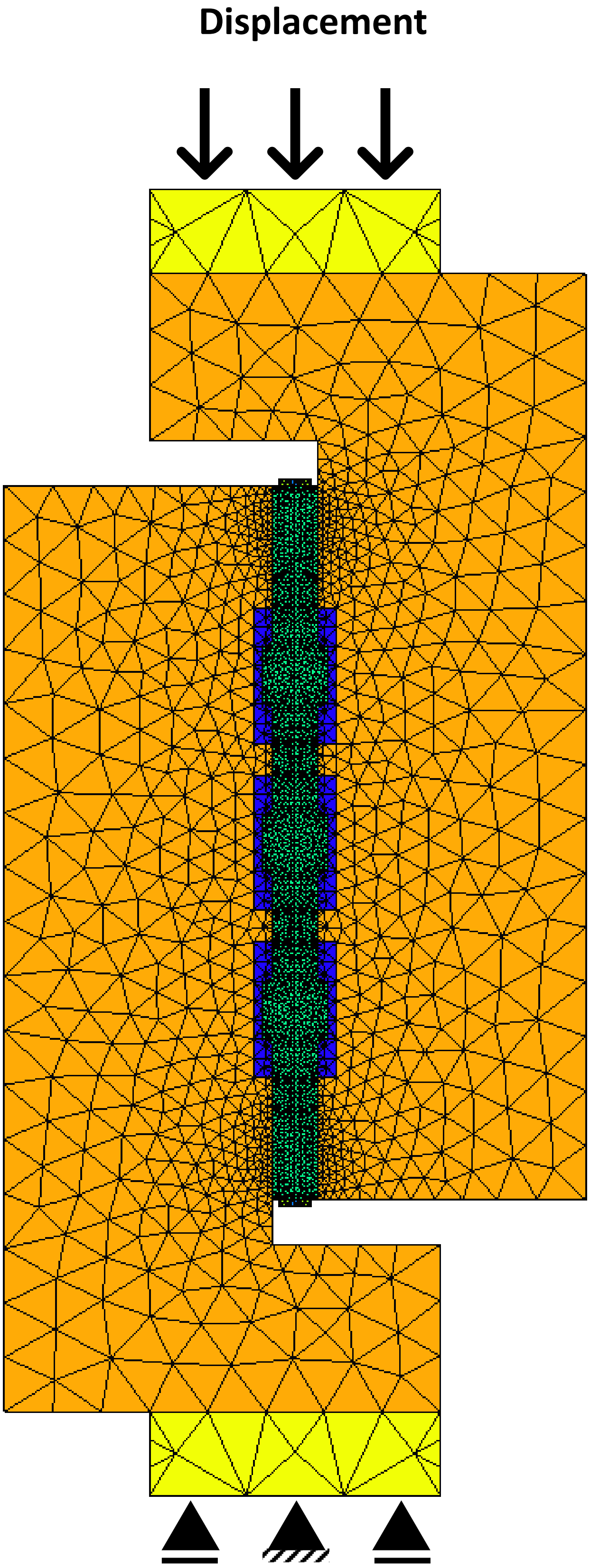

Figure 66. Modeling and meshing of D20 model

5.4. Analysis and results

5.4.1. The peak load of the connection

The peak load of the connection for D10 specimens of the experiment and the Finite Element Limit Analysis (FELA) performed by Sørensen et al. [57], along with RBCS simulations are gathered in Table 13.

Table 13. Peak push-off force for D10 shear connection specimen

No.	Simulation/Experiment	First Peak [KN]
1	Experiment D10-I	448.56
2	Experiment D10-II	448.62
3	FELA D10	340.5
4	RBCS D10 w/o V-bar	513.77
5	RBCS D10 with V-bar	511.16

It can be observed that the two experiment give almost same peak load and that how FELA analysis can give a proper conservative estimation of the connection. It can also be observed that the RBCS simulations overestimate the strength of the connection by about 14% with V-bar having a negligible effect on the peak strength of the connection. With this estimation no further calibration was performed and the model was used for simulation of D20 specimen.

The peak push-off force for the D20 specimen is given in Table 14. It can be observed that there is a marginal increase in the D20 specimen compared to the D10 both for simulation and experiment. In this case also the RBCS results over estimate the push-off strength by about 8%.

Table 14. Peak push-off force for D20 shear connection specimen

No.	Simulation/Experiment	First Peak [KN]
1	Experiment D20-I	526.62
2	Experiment D20-II	517.03
3	FELA D20	486
4	RBCS D20 with V-bar	565.36

5.5. Failure mode of the connection

The failure mode of the connection obtained from experiment using Digital Image Correlation (DIC) method is obtained and reported by Sørensen et al. [57]. These results are compared with what is obtained through visualization of displacement distribution in modelled specimens of RBCS analysis for D10 and D20 specimens (Figure 67).

As it can be observed in the visualized results, the failure pattern of D10 and D20 specimens is captured correctly in the model. A very interesting point is that the full failure of the shear keys in the D20 specimen is only observed at the two end keys and not in the middle key. This point is not reported by Sørensen et al. [57] but it seems this is not be a simple coincidence and such failure is more likely to happen at the end keys rather than central one. This phenomenon may happen due to the fact that the prefabricated parts are not rigid and therefore the case is not a pure shear case as the bending deformation of the prefabricated elements can be observed in the exaggerated visualized deformation in Figure 68.

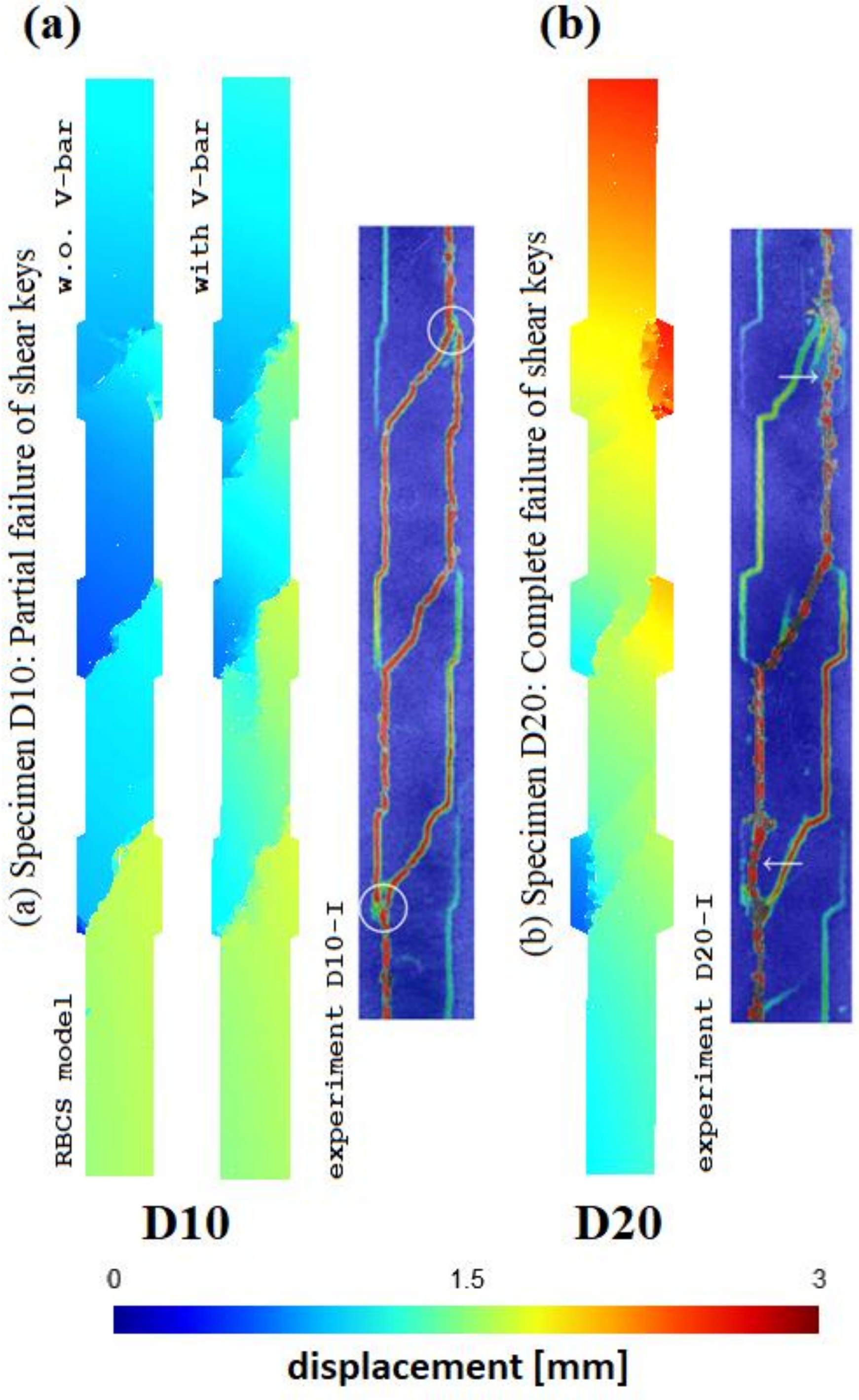

Figure 67. Visualization of elements displacement in RBCS analysis compared with strain distribution in the connection obtained from DIC (Sørensen et al. [57]) a)in D10 specimen b)in D20 specimen

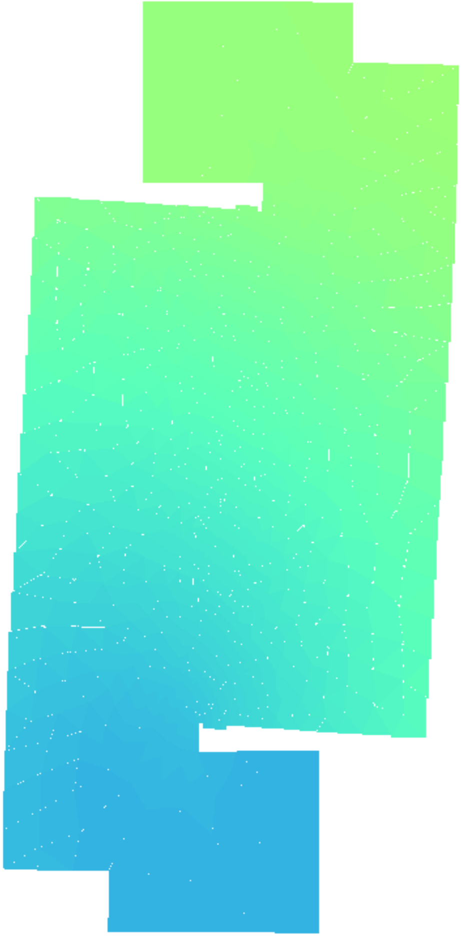

Figure 68. Deformation of the D20 RBCS model at step 30 (×50)

5.6. Stress transfer in the model

The capability of RBCS to evaluate principal stresses is used to study stress transfer action in the connection as depicted in Figure 69.

In this figure it can be observed how formation of cracks can limit and affect the stress transfer mechanism. Another interesting point is stress transfer at the ends of the cast in-situ grout parts which are not noticed or mentioned in the experiment. This is in fact due to the rotation of the model as shown in Figure 68. Also it is worth mentioning that the diagonal crack of the D20 specimen for the end shear key connections which is less visible in the Figure 67 can be clearly observed in Figure 69 since the stress values at the upper part of the crack is much smaller.

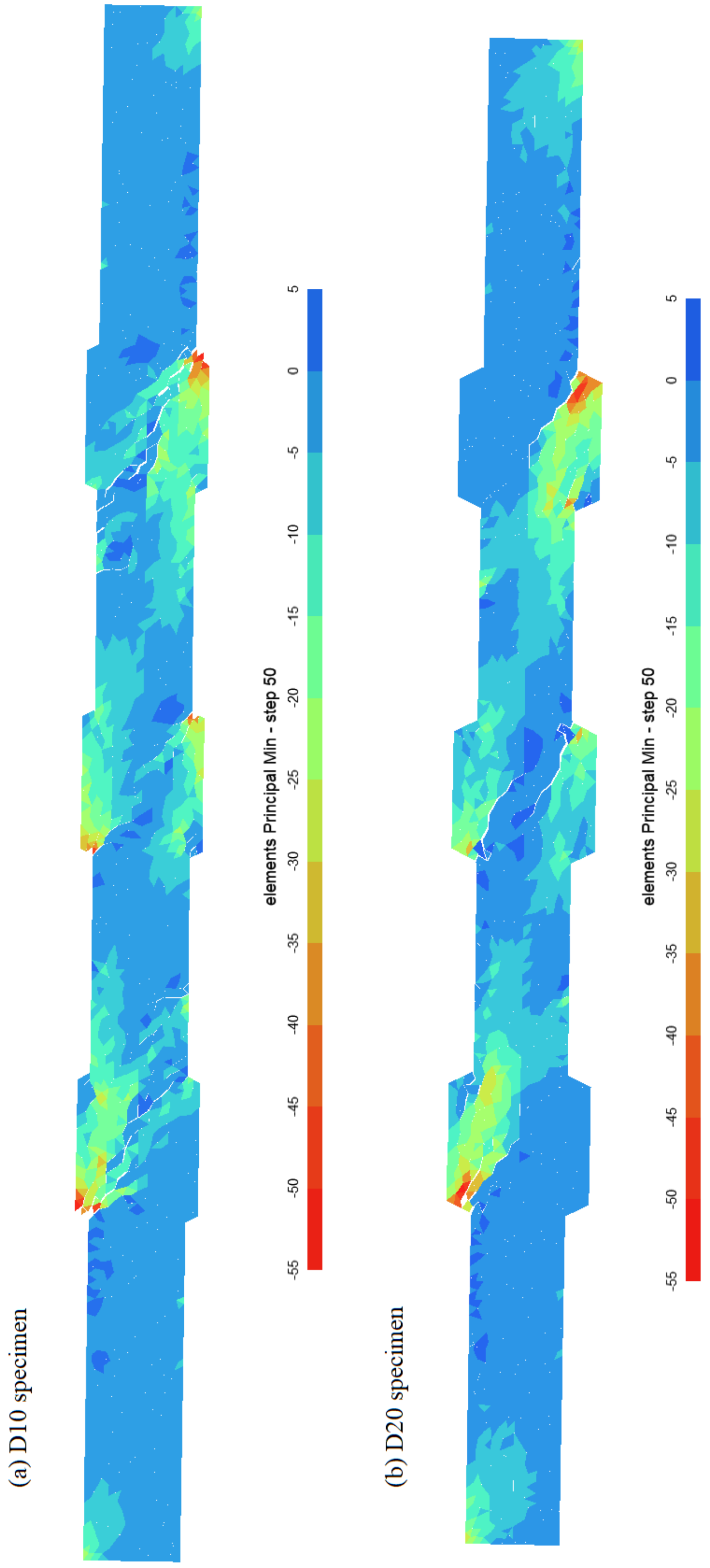

(a) D10 specimen

(b) D20 specimen

Figure 69. Minimum principal stress in a) D10 specimen b) D20 specimen (elements beyond spectrum limits are omitted)

5.7. Bottom line

In this chapter the behaviour of a prefabricated structural concrete wall was simulated and investigated using RBCS element. It was observed that the cracking behaviour of the model matches with the ones observed and reported in the experiment. For the case of D10 details, the shear keys will not totally fail while for the case of D20 connection shear connection at the ends will break at one side and in the opposite sides of the other end. Considerable stress transfer is also observed at the ends of the grout part away from the shear keys. These findings in the model show the importance of the improvements made to the element which made visualization of the elements’ displacement spectrum and principal stresses possible.

Chapter 6

Conclusion

A discrete model, called Rigid Body Coupled Springs (RBCS), was introduced with the advantage of incorporating Poisson effect in procedure of deriving the stiffness matrix. Unlike some alternative methods to recreate the Poisson deformation no extra iterations are needed in the elastic stage, in addition mechanical properties of springs are not modified. The analysis results show that the Poisson deformations are successfully calculated.

6.1. Summary of the studied cases

The proposed RBCS element was employed to simulated concrete under common experimental tests and the following behaviours was observed:

1. In uniaxial compression the obtained stress-strain curve was more realistic compared to RBSM. During the uniaxial loading small splitting cracks were formed in the specimen but the final failure mode was due to diagonal shear cracks. Simulation of loading jaw with assumption of complete bound affected the peak and the post-peak behaviour of specimen.
2. The direct tensile tests were simulated for dog-bone and hourglass specimens. The tensile failure happens with a sudden appearance of a horizontal crack. The obtained tensile strength is very close to expected tensile strength for specimen.
3. The split tensile on cylindrical specimen with diameter of 150mm was simulated assuming a load bearing width of 10mm. The obtained splitting tensile strength is larger than tensile obtained from direct tensile test on dog-bone specimen and very close to direct tensile test performed on hourglass specimen. However, the loading width and form of force distribution may affect the splitting test results.
4. The uniaxial compressive failure in non-homogenous models which include aggregate phase were more brittle possibly due to stress concentration.

The prediction of the behaviour of steel fibre reinforced concrete (SFRC) reinforced with various types of the straight rounded steel fibre under several experiments was made possible by new material model introduced to RBCS technique. This material model developed with the idea of implementing inclined pull-out behaviour of straight rounded steel fibre into mesoscopic tensile model and improvement of shear behaviour based on the volumetric reinforcement index parameter of the SFRC mixture. Simulation of various cases was attempted with the outcome compared to the cited experimental results. Base on the obtained results, the following conclusions can be made:

1. In the case of the uniaxial compression the marginal increment of peak strength and improvement of post peak ductility can be incorporated by the model.
2. According to outcome from direct tension, the post peak residual strength of this test is within the experimental observed data.
3. In the simulation of the three-point bending test, 6 specimens were simulated. The simulation outcomes are comparable with the experimental results. The residual strength flexural tests were well predicted in most of the cases but the drop after the peak happened more rapidly in the simulations.
4. The push-off test simulation was simulated to investigate direct shear behaviour. The failure of the plain concrete happened in a larger slip compared to the chosen experiment but the slope of the slip – shear stress was accurate but the cracking patterns in the model was as expected. The fibre contribution lead to a post-peak residual strength as expected.

Based on the observed results the modified RBCS element presented in this study could simulated the behaviour of SFRC material in the studied cases. Though the implemented analytical models used to predict the pull-out behaviour of the fibre limits the model to the rounded-straight steel fibre types, but a similar concept can be used to simulate the behaviour of the hooked steel fibre or other types of the fibre which may become the topic of a future study.

In the final case study, a structural connection was simulated using RBCS to extend the application of this method from material level to structural level and investigate the capability of the method in such cases. The RBCS models successfully captured the failure modes of the so called D10 and D20 types of the connections and the study of the crack formations, displacements and principal stress revealed some interesting points about the structural behaviour such as the failure of D20 keys in the end connection in one side and opposite to the other and the stress at the end of the connection away from the keys.

6.2. Assessment on the achieving the goals of the study

This study was performed aiming for providing an improved version of the RBSM discrete modelling techniques.

One of the main issues observed in RBSM method is inability to capture the Poisson deformation and the method used to incorporate in RBSM in legacy RBSM code is not accurate and may cause inaccuracy in the inner stresses of the model. The proposed element has resolved this issue and can calculate the Poisson deformations accurately.

Another issue that existed in RBSM is the inability to calculate the principal stresses and inaccuracies of the stress visualization. This issue is also resolved in the proposed element. If the calculation of the principal stresses is requested before initiation of the analysis such information will be saved in the output file in a way that can be easily postprocessed using open source post-processing software, GMSH[26].

The RBSM model also had the problem with the pre-peak behaviour of concrete in uniaxial compression in a way the strain corresponding to peak is small and at the pre-peak there is not enough curvature in stress-strain response of the model. Accordingly, the next goal of this study was to equip the new element with the capability to model nonlinear behaviour of concrete and also resolve this issue. As a result, the compressive behaviour of the concrete was improved by defining new material models. The behaviour of the model was then verified in known standard test on concrete to make sure the element can capture the behaviour of the concrete properly.

Following that, extending the capability of the new element to simulate fibrous concrete was also another goal of this study which was achieved. In this stage the rotational springs, which are commonly omitted in RBSM simulations, were also added to the concept of the new element to capture the flexural failure cases more accurately. The material model developed for SFRC material was investigated in several cases and showed good accordance with the experimental results in most cases.

Finally, application of the method to a case study of prefabricated concrete wall shear connection showed the effectiveness of the method in structural level. The model was first calibrated with a shallow shear key case and then used do simulate a deep shear key and it was observed that the failure pattern from partial damage and detaching from prefabricated elements in the shallow key connection changed to the failure of the shear keys. The investigations showed a failure patterns which may have not been emphasised and understood in the experiment.

6.3. Disadvantages of RBCS compared to RBSM

While the merits of the new element have been discussed in this manuscript, it is worth to mansion the disadvantages of the RBCS compared to RBSM. The RBCS element incorporates the Hooke's law into the discrete model and therefore has the advantages of calculating Poisson's deformation and the stresses in the model. However, this implementation is not free of cost. Compared to RBSM the RBCS element has more complicacies and it is harder to develop. In addition, the more complicated theory comes with more calculation cost. Though it seems that the concept can be extended into 3-dimensions, the current model is limited to 2-deminsions and there might be concerns about the calculation costs of the models in 3-dimensions. It is also worth mentioning that the calculation costs can be dramatically reduced by employing better calculation techniques such as assembling the global stiffness matrix in a more proper way to provide a band matrix with proper storage scheme (i.e. only store non-zero members in the memory).

6.4. Future studies

The proposed element in this study can be suited for in new applications. Extending this method to cases such as studying environmental effects or non-static cases are some of other aspects that can be subject of further studies.

Though the introduced discrete model provided, the ability for simulation of the nonlinear materials in a 2-dimensional simulation, a similar 3-dimensional element can be derived using a similar concept.

References

[1] K. Meguro, H. Tagel-Din, A new efficient technique for fracture analysis of structures, Bulletin of Earthquake Resistant Structure Research Center, IIS, Univ. of Tokyo. (1997) 103–116.

[2] K. Nagai, Y. Sato, T. Ueda, Mesoscopic simulation of failure of mortar and concrete by 2D RBSM, Journal of Advanced Concrete Technology. 2 (2004) 359–374.

[3] B. Beckmann, K. Schicktanz, D. Reischl, M. Curbach, DEM simulation of concrete fracture and crack evolution, Structural Concrete. 13 (2012) 213–220. https://doi.org/10.1002/suco.201100036.

[4] T. Kawai, New discrete models and their application to seismic response analysis of structures, Nuclear Engineering and Design. 48 (1978) 207–229.

[5] K. Meguro, H. Tagel-Din, A new simple and accurate technique for failure analysis of structures, Bulletin of Earthquake Resistant Structure. (1998) 51–61.

[6] H. Tagel-Din, K. Meguro, Consideration of Poisson's ratio effect in structural analysis using elements with three degrees of freedom, Bulletin of Earthquake Resistant Structure Research Center. 31 (1998) 41–50.

[7] K. Sonoda, A. Kambayashi, Applicability of a Rigid Body Spring Model to Impact Problems of Elastic Bodies, Doboku Gakkai Ronbunshu. 1992 (1992) 147–155. https://doi.org/10.2208/jscej.1992.147.

[8] A. Kambayashi, H. Kobayashi, K. Sonoda, Applicability of a Rigid Body Spring Model to Impact Problems of Axi-symmetric Elastic Bodies, Journal of Applied Mechanics. 2 (1999) 271–278. https://doi.org/10.2208/journalam.2.271.

[9] K. Nagai, Y. Sato, T. Ueda, Mesoscopic simulation of failure of mortar and concrete by 3D RBSM, Journal of Advanced Concrete Technology. 3 (2005) 385–402.

[10] T. Ueda, M. Hasan, K. Nagai, Y. Sato, L. Wang, Mesoscale simulation of influence of frost damage on mechanical properties of concrete, Journal of Materials in Civil Engineering. 21 (2009) 244–252.

[11] Y.H. Gedik, H. Nakamura, Y. Yamamoto, M. Kunieda, Evaluation of three-dimensional effects in short deep beams using a rigid-body-spring-model, Cement and Concrete Composites. 33 (2011) 978–991.

[12] Y. Yamamoto, H. Nakamura, I. Kuroda, N. Furuya, Crack propagation analysis of reinforced concrete wall under cyclic loading using RBSM, European Journal of Environmental and Civil Engineering. 18 (2014) 780–792.

[13] S. Mehrpay, T. Ueda, Application of a new RBSM element into simulation of nonlinear behaviour of concrete, in: Krakow, 2019.

[14] S. Mehrpay, T. Ueda, Developing a new Rigid Body Spring Model Element for incorporating Poisson effect in simulating concrte-like materials, in: Kyushu, 2017.

[15] S. Mehrpay, Z. Wang, T. Ueda, Development and Application of a new Discrete element into simulation of nonlinear behaviour of concrete, Structural Concrete. (2019). https://doi.org/10.1002/suco.201900059.

[16] Intel® Parallel Studio XE, Intel Corporation, 2018.

[17] Intel® Math Kernel Library, Intel Corporation, 2018.

[18] K. Nagai, Y. Sato, T. Ueda, Mesoscopic simulation of failure of mortar and concrete by 2D RBSM, Journal of Advanced Concrete Technology. 2 (2004) 359–374.

[19] J.-L. Tailhan, P. Rossi, D. Daviau-Desnoyers, Probabilistic numerical modelling of cracking in steel fibre reinforced concretes (SFRC) structures, Cement and Concrete Composites. 55 (2015) 315–321. https://doi.org/10.1016/j.cemconcomp.2014.09.017.

[20] C. Nader, P. Rossi, J.-L. Tailhan, Numerical strategy for developing a probabilistic model for elements of reinforced concrete: NADER et al., Structural Concrete. 18 (2017) 883–892. https://doi.org/10.1002/suco.201600217.

[21] A.P.C. Duarte, N. Silvestre, J. de Brito, E. Júlio, Numerical study of the compressive mechanical behaviour of rubberized concrete using the eXtended Finite Element Method (XFEM), Composite Structures. 179 (2017) 132–145. https://doi.org/10.1016/j.compstruct.2017.07.048.

[22] Y. Fang, B.N. Nguyen, K. Carroll, Z. Xu, S.B. Yabusaki, T.D. Scheibe, A. Bonneville, Development of a coupled thermo-hydro-mechanical model in discontinuous media for carbon sequestration, International Journal of Rock Mechanics and Mining Sciences. 62 (2013) 138–147. https://doi.org/10.1016/j.ijrmms.2013.05.002.

[23] D. Asahina, K. Ito, J. Houseworth, J. Birkholzer, J. Bolander, Simulating the Poisson effect in lattice models of elastic continua, Computers and Geotechnics. 70 (2015) 60–67.

[24] Comité euro-international du béton, CEB-FIP model code 1990, Telford, 1993.

[25] Comité euro-international du béton, fib Model Code for Concrete Structures 2010: fib, 2013.

[26] C. Geuzaine, J.-F. Remacle, Gmsh: A 3-D finite element mesh generator with built-in pre- and post-processing facilities, International Journal for Numerical Methods in Engineering. 79 (2009) 1309–1331.

[27] T. Kawai, New discrete models and their application to seismic response analysis of structures, Nuclear Engineering and Design. 48 (1978) 207–229. https://doi.org/10.1016/0029-5493(78)90217-0.

[28] K. Nagai, Y. Sato, T. Ueda, Y. Kakuta, Numerical simulation of fracture process of concrete model by Rigid Body Spring Method, Konkurito Kogaku Nenji Ronbun Hokokushu (Proceedings of the Japan Concrete Institute). 24 (2002).

[29] K. Nagai, Y. Sato, T. Ueda, Mesoscopic simulation of failure of mortar and concrete by 3D RBSM, Journal of Advanced Concrete. 3 (2005) 385–402.

[30] T. Ueda, M. Hasan, K. Nagai, Y. Sato, L. Wang, Mesoscale simulation of influence of frost damage on mechanical properties of concrete, Journal of Materials in Civil Engineering. 21 (2009) 244–252.

[31] D.J. Carreira, K.-H. Chu, Stress-strain relationship for plain concrete in compression, in: Journal Proceedings, 1985: pp. 797–804.

[32] B. Li, K. Maekawa, H. Okamura, Contact density model for cracks in concrete, in: IABSE Colloquium, Delft, 1987: pp. 51–62.

[33] B. Bujadham, K. Maekawa, Qualitative studies on mechanisms of stress transfer across cracks in concrete, Doboku Gakkai Ronbunshu. 1992 (1992) 265–275.

[34] L. Eddy, K. Matsumoto, K. Nagai, Effect of perpendicular beams on failure of beam-column knee joints with mechanical anchorages by 3D RBSM, Journal of Asian Concrete Federation. 2 (2016) 56–66.

[35] M.R.A. van Vliet, J.G.M. van Mier, Experimental investigation of concrete fracture under uniaxial compression, Mechanics of Cohesive-Frictional Materials. 1 (1996) 115–127. https://doi.org/10.1002/(SICI)1099-1484(199601)1:1<115::AID-CFM6>3.0.CO;2-U.

[36] V. Malárics, H.S. Müller, Experimental and numerical analysis of the fracture process at the splitting tension test for concrete, in: 7th International Conference on Fracture Mechanics of Concrete and Concrete Structures, Seogwipo, South Korea, 2010.

[37] V. Malárics, H.S. Müller, Evaluation of the splitting tension test for concrete from a fracture mechanical point of view, Proceedings of the Fracture Mechanics of Concrete and Concrete Structures—Assessment, Durability, Monitoring and Retrofitting of Concrete Structures. (2010) 709–716.

[38] A. Amin, S.J. Foster, A. Muttoni, Derivation of the σ-w relationship for SFRC from prism bending tests, Structural Concrete. 16 (2015) 93–105.

[39] DIANA, DIANA FEA BV, 2018.

[40] A.S. C496, Standard test method for splitting tensile strength of cylindrical concrete specimens, (2004).

[41] W. Głodkowska, J. Kobaka, Modelling of properties and distribution of steel fibres within a fine aggregate concrete, Construction and Building Materials. 44 (2013) 645–653. https://doi.org/10.1016/j.conbuildmat.2013.02.037.

[42] F.-Y. Li, L.-Y. Li, Y. Dang, P.-F. Wu, Study of the Effect of Fibre Orientation on Artificially Directed Steel Fibre-Reinforced Concrete, Advances in Materials Science and Engineering. 2018 (2018) 1–11. https://doi.org/10.1155/2018/8657083.

[43] L.J. Malvar, J.E. Crawford, J.W. Wesevich, D. Simons, A plasticity concrete material model for DYNA3D, International Journal of Impact Engineering. 19 (1997) 847–873.

[44] D.-Y. Yoo, S.-T. Kang, N. Banthia, Y.-S. Yoon, Nonlinear finite element analysis of ultra-high-performance fiber-reinforced concrete beams, International Journal of Damage Mechanics. 26 (2017) 735–757. https://doi.org/10.1177/1056789515612559.

[45] S.M. Allam, M.S. Shoukry, G.E. Rashad, A.S. Hassan, Evaluation of tension stiffening effect on the crack width calculation of flexural RC members, Alexandria Engineering Journal. 52 (2013) 163–173. https://doi.org/10.1016/j.aej.2012.12.005.

[46] B. Massicotte, Tension-Stiffening Model for Planar Reinforced Concrete Members, (1990) 20.

[47] Y. Yamamoto, H. Nakamura, I. Kuroda, N. Furuya, Crack propagation analysis of reinforced concrete wall under cyclic loading using RBSM, European Journal of Environmental and Civil Engineering. 18 (2014) 780–792.

[48] A.S. Ezeldin, P.N. Balaguru, Normal- and High-Strength Fiber-Reinforced Concrete under Compression, Journal of Materials in Civil Engineering. 4 (1992) 415–429. https://doi.org/10.1061/(ASCE)0899-1561(1992)4:4(415).

[49] P. Soroushian, C.D. Lee, CONSTITUTIVE MODELING OF STEEL FIBER REINFORCED CONCRETE UNDER DIRECT TENSION AND COMPRESSION, in: Publication of: Elsevier Applied Science Publishers Limited, THE UNIVERSITY OF WALES, COLLEGE OF CARDIFF, SCHOOL OF ENGINEERING, UNITED KINGDOM, 1989.

[50] D.A. Fanella, A.E. Naaman, Stress-Strain Properties of Fiber Reinforced Mortar in Compression, ACI Journal Proceedings. 82 (1985). https://doi.org/10.14359/10359.

[51] Parviz Soroushian and Ziad Bayasi, Fiber Type Effects on the Performance of Steel Fiber Reinforced Concrete, Materials Journal. 88 (1991). https://doi.org/10.14359/1883.

[52] T. Soetens, S. Matthys, A SEMI-ANALYTICAL MODEL TO SIMULATE THE DIRECT SHEAR PULL-OUT BEHAVIOUR OF HOOKED-END STEEL FIBRES, in: Proceedings Fibre Reinforced Concrete BEFIB2012, 2012.

[53] B. Barragan, R. Gettu, L. Agullo, R. Zerbino, Shear failure of steel fiber-reinforced concrete based on push-off tests, ACI Materials Journal. 103 (2006) 251.

[54] N. Jurkowska, Considering nonlinear properties of concrete in the design of reinforced concrete structures for torsion, IOP Conference Series: Materials Science and Engineering. 364 (2018) 012030. https://doi.org/10.1088/1757-899X/364/1/012030.

[55] L. Fu, H. Nakamura, H. Furuhashi, Y. Yamamoto, T. Miura, Mechanism of shear strength degradation of a reinforced concrete column subjected to cyclic loading, Structural Concrete. 18 (2017) 177–188. https://doi.org/10.1002/suco.201600052.

[56] J.H. Sørensen, L.C. Hoang, J.F. Olesen, G. Fischer, Test and analysis of a new ductile shear connection design for RC shear walls, Structural Concrete. 18 (2017) 189–204. https://doi.org/10.1002/suco.201600056.

[57] J.H. Sørensen, M.A. Herfelt, L.C. Hoang, A. Muttoni, Test and lower bound modeling of keyed shear connections in RC shear walls, Engineering Structures. 155 (2018) 115–126. https://doi.org/10.1016/j.engstruct.2017.11.004.

[58] I. De la Varga, J.F. Muñoz, D.P. Bentz, R.P. Spragg, P.E. Stutzman, B.A. Graybeal, Grout-concrete interface bond performance: Effect of interface moisture on the tensile bond strength and grout microstructure, Construction and Building Materials. 170 (2018) 747–756. https://doi.org/10.1016/j.conbuildmat.2018.03.076.

[59] G. Xiong, J. Liu, G. Li, H. Xie, A way for improving interfacial transition zone between concrete substrate and repair materials, Cement and Concrete Research. 32 (2002) 1877–1881. https://doi.org/10.1016/S0008-8846(02)00840-2.

[60] J.H. Sørensen, L.C. Hoang, P.N. Poulsen, M.A. Herfelt, Experimental investigation of keyed shear joints subjected to a combination of compression and shear loads, Proceedings of the Fib Symposium 2019. (2019) 2278–2285.

Footnotes

[1] The term "axial strain" refers to the condition in which only strain in one direction is allowed (

Figure 70). In this case (i.e. $\varepsilon_y = \varepsilon_z = 0$) the following stress-strain relationship, which is used in the stiffness matrix of the original RBSM, can be derived:

$$\varepsilon_x = \frac{\sigma_x}{E} - \nu\frac{\sigma_y}{E} - \nu\frac{\sigma_z}{E} \tag{F1.1}$$

$$\varepsilon_y = -\nu\frac{\sigma_x}{E} + \frac{\sigma_y}{E} - \nu\frac{\sigma_z}{E} = 0 \tag{F1.2}$$

$$\varepsilon_z = -\nu\frac{\sigma_x}{E} - \nu\frac{\sigma_y}{E} + \frac{\sigma_z}{E} = 0 \tag{F1.3}$$

For isotropic material we have $\sigma_y = \sigma_z$, using Equation $(F1.2)$

$$\Rightarrow -\nu\frac{\sigma_x}{E} + \frac{\sigma_y}{E}(1-\nu) = 0 \Rightarrow \sigma_y = \sigma_z = \frac{\nu}{1-\nu}\sigma_x$$

Replace above in Equation $(F1.1) \Rightarrow \varepsilon_x = \frac{\sigma_x}{E} - \frac{2\nu^2}{(1-\nu)}\frac{\sigma_x}{E} = \left(\frac{1-\nu-2\nu^2}{1-\nu}\right)\frac{\sigma_x}{E}$

$$\Rightarrow \varepsilon_x = \left(\frac{(1+\nu)(1-2\nu)}{1-\nu}\right)\frac{\sigma_x}{E} \tag{F1.4}$$

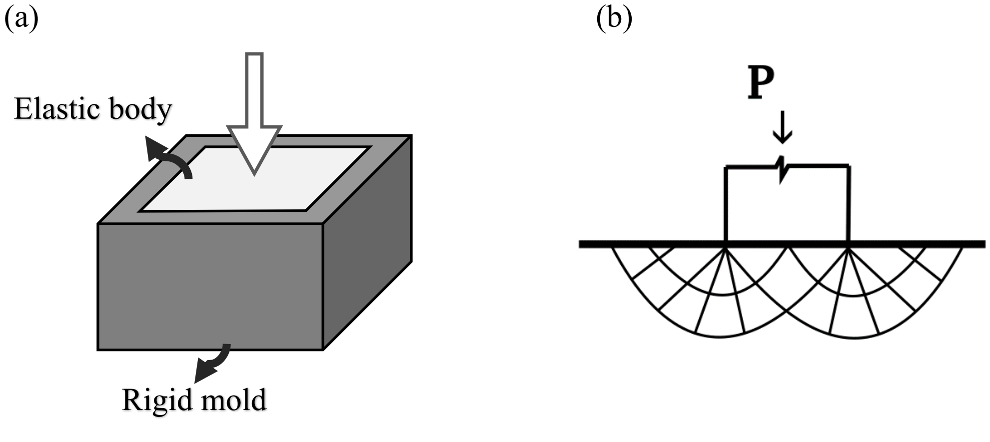

Figure 70. Special case of axial strain: a) elastic body inside a rigid mold b) semi-infinite volume

[2] The term “combined plane strain – plane stress” refers to the special condition in which in-plane strain in one direction is allowed while the condition of plane stress is used (Figure 71). In this case (i.e. $\varepsilon_y = \sigma_z = 0$) the following stress-strain relationship, which is also used in the stiffness matrix of the mentioned RBSM models, can be derived:

$$\varepsilon_x = \frac{\sigma_x}{E} - \nu\frac{\sigma_y}{E} - 0 \tag{F2.1}$$

$$\varepsilon_y = -\nu\frac{\sigma_x}{E} + \frac{\sigma_y}{E} - 0 = 0 \Rightarrow \sigma_y = \nu\sigma_x \tag{F2.2}$$

Introducing $(F2.2)$ to $(F2.1)$

$$\Rightarrow \sigma_x = \frac{E\varepsilon_x}{(1-\nu^2)} \tag{F2.3}$$

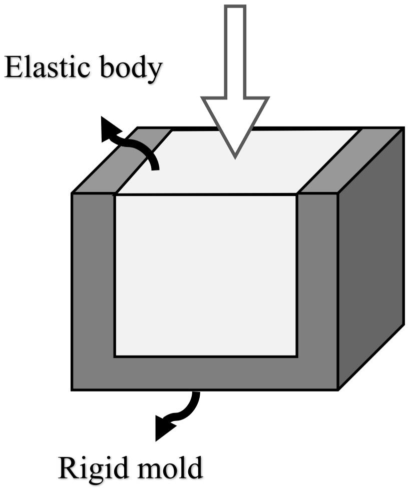

Figure 71. combined plane strain (in 2D plane) and plane stress (out of 2D plane)

List of Tables

List of Figures

セメント系複合材料および構造要素のシミュレーションのための

剛体-バネ連成離散モデルの開発

メヘルペイ　モガッダム　　サイード

北海道大学　大学院工学院
北方圏環境政策工学部門

２０２０年　０１月